Neutron Scattering Investigations of Three-Dimensional Topological States

by

Melissa Elizabeth Henderson

A thesis
presented to the University of Waterloo
in fulfillment of the
thesis requirement for the degree of
Doctor of Philosophy
in
Physics (Quantum Information)

Waterloo, Ontario, Canada, 2023

Examining Committee Membership

The following served on the Examining Committee for this thesis. The decision of the Examining Committee is by majority vote.

External Examiner: Dr. Julie Borchers
Senior Research Scientist, Neutron Condensed Matter Science Group,
National Institute of Standards and Technology

Supervisor(s): Dr. Dmitry Pushin
Associate Professor, Dept. of Physics and Astronomy,
University of Waterloo

Internal Member: Dr. Anton Burkov
Professor, Dept. of Physics and Astronomy, University of Waterloo

Internal-External Member: Dr. Jonathan Baugh
Professor, Dept. of Chemistry, University of Waterloo

Other Member(s): Dr. David Cory
Professor, Dept. of Chemistry, University of Waterloo

Author's Declaration

I hereby declare that I am the sole author of this thesis. This is a true copy of the thesis, including any required final revisions, as accepted by my examiners.

I understand that my thesis may be made electronically available to the public.

Abstract

Topological magnets represent a unique class of quantum materials in which a non-trivial Berry curvature in real- or momentum-space couples to the magnetic properties of the topological electronic or spin system. Magnetic skyrmions constitute one such class of topological magnets, characterized by real space topological swirling spin-textures which manifest as localized nanometric excitations in the magnetization field. These protected quasi-particle objects possess a helical chiral structure which supports a diverse landscape of states and defects, whose interactions with spins and electrons produce novel transport properties and emergent dynamics controllable over a wide range of parameter space. This spectrum of phenomena has inspired magnetic skyrmions as the forerunners for novel spintronic high-density memory and ultra-low power logic device applications. As quasi-particles, skyrmions may condense into crystalline orders, typically forming periodic lattice arrangements which extend three-dimensionally in bulk materials. This enhanced dimensionality opens the door to new stabilization pathways, configurational degrees of freedom, and dynamical modes which offer unique functionalities to those of thin systems. For practical applications, understanding skyrmion nucleation, annihilation, transition, and organizational pathways is critical to realizing controllable dynamics and manipulation in future devices.

In this thesis, we explore the development and application of various neutron scattering tomography and structured neutron beam techniques for three-dimensional investigations of bulk magnetic topological materials and their defect-mediated dynamical phenomena. A combination of X-ray, magnetometry, and neutron scattering techniques are used to first identify and characterize the disordered phase of an above room-temperature bulk skyrmion material, $Co_8Zn_8Mn_4$. Detailed small angle neutron scattering (SANS) measurements are then performed over the entire temperature-magnetic field phase diagram of the material as a function of a dynamic skyrmion ordering sequence. 2D SANS images in combination with micromagnetic simulations reveal a novel disordered-to-ordered skyrmion square lattice transition pathway which represents a new type of non-charge conserving topological transition. This transition is characterized by a novel promotion of four-fold order in SANS and a violation of the conservation of total skyrmion number. Dynamical skyrmion responses in the metastable skyrmion triangular lattice phase showed an exotic memory phase, with an ordered skyrmion signal persisting in spite of hysteresis protocols involving field-induced saturation into the ferromagnetic phase.

Further studies of skyrmion stabilization mechanisms and their dynamical defect pathways were performed through the development of a novel SANS tomography algorithm, applied to the ordered thermal equilibrium skyrmion triangular lattice phase of the bulk

$Co_8Zn_8Mn_4$ sample. Multi-projection neutron scattering datasets collected from the sample were used to generate the first three-dimensional visualizations of a bulk skyrmion lattice. The reconstructions unveiled a host of exotic skyrmion features, such as branching, segmented, twisting, and filament structures, mediated by three-dimensional topological transitions through two different emergent monopole (MP)-antimonopole (AMP) defect pathways.

Methods for the direct identification and determination of topological features and defects of bulk micromagnetic materials, without a priori knowledge of the sample, can be achieved through the incorporation of structured neutron beam methods to neutron scattering experiments. Holographic approaches similar to those used in the development of optical structured waves were implemented with neutrons to generate a method for the selective tuning of single-valued neutron orbital angular momentum (OAM) states. A conventional SANS setup was used to explore the diffraction of linear neutron waves input on a microfabricated grating which consists of arrays of phase-gratings with q-fold fork dislocations and nanometric spatial dimensions comparable to those of magnetic skyrmion lattice periodicities. Far-field scattering images exhibit doughnut intensity profiles centered on the first diffraction orders, with q-dependent radii, thereby demonstrating the tunable generation of topological neutron states for phase- and topology-matched studies of quantum materials.

Together, these studies demonstrate the development and application of novel tools for direct investigations of bulk topological magnetic materials, while uncovering a diverse collection of skyrmion energetics, disorder-dependent dynamics, and three-dimensional topological transition defect pathways. Future works are proposed which explore the three-dimensional formation and evolution of bulk skyrmion tubes under various temperature-magnetic field trajectories and degrees of skyrmion order, using both tomographic, structured neutron beam approaches, and combinations thereof. In doing so, we may provide the first standalone method of characterizing bulk magnetic sample topologies, defect densities, and their correlations. These methods open the door to a new generation of neutron scattering techniques for probing exotic topological interactions and the complete standalone characterization of quantum materials.

Acknowledgements

The undertaking of a Ph.D. degree can be an isolating and arduous endeavour, however thanks to a dedicated set of scientists, collaborators, family, and friends, I have never felt this to be the case. First and foremost, I would like to thank my supervisor, Dmitry Pushin. You have always supported my crazy ideas and provided me with encouragement as a young researcher. Your belief in my work and my abilities has made this achievement possible. I would like to extend a special thank you to a multitude of other colleagues and mentors at the University of Waterloo. Dusan Sarenac, your guidance, advice, and support made you a cherished mentor and friend throughout my degree. Your sage advice and wisdom helped me to navigate the complex waters of my Ph.D. Thank you to my colleague Olivier Nahman-Levesqué for working at ungodly hours during the night as I did, allowing for our countless meetings on dynamical diffraction and programming in exchange for my knowledge on condensed matter and neutrons. I will never forget your lessons in chess and look forward to maintaining our tradition of bouncing ideas off of one another at odd hours of the night. To my office-mate and friend Connor Kapahi, our many conversations and mutual bonding sessions of our Ph.D.'s over some beers always made for a refreshing distraction from the chaos of our degrees. I would also like to extend a special thank you to my committee members for their constant guidance along this journey and their unique insights which helped shape my research and expand my perspectives.

I would like to thank my collaborators at McMaster University, especially James Beare, Sudarshan Sharma, and Evan Smith, for their many efforts and support during the synthesis and characterization of our many samples. To Mathew Pula, you have been the best crystal growth partner a girl could ask for. I am indebted to you for the seemingly endless all-night crystal growths and I will especially miss our post-growth late-night/early morning street races which undoubtedly took a toll on my modest car. Finally, I would like to thank Dr. Luke for first introducing me to the field of condensed matter and neutrons in my undergraduate degree, and for continuing to support my research throughout my graduate studies.

My time spent as a guest researcher at the NCNR provided me with some of the greatest experiences of my degree. The NCNR fosters an incredibly unique research atmosphere filled with a diverse set of scientists whom all share the unwavering desire to make exciting science happen. It is this unique collection of individuals who helped bring my crazy experiment ideas to fruition. I would like to extend my deepest gratitude to Jeff Kryzwon and Credric Gagnon for helping me to develop various SANS apparatus and for their saintlike patience when Shannon Watson and myself returned back to them for the one hundredth time asking to make another "slight" modification to the instrument. I would like to thank

Juscelino Leao and Tanya Dax for always helping to make and test last minute sample environments with me for neutron experiments all around the world. Juscelino, your designs are remarkably simple yet effect and always highly entertaining. Tanya, I admire you expertise and the devices you develop for me are always making new regimes of physics accessible in my experiments. Of course these sample environments would also not have been possible without the engineering and machining staff at the NCNR. In particular, I would like to thank Colin Wrenn for always getting my "urgent" designs made in time, even if that meant doing it in a day. On that note, I would like to thank all those at the NCNR who accepted my butter tart bribes. I would also like to thank my colleagues and friends Hannnah Burrall and Robert Valdillez for providing both intellectual and emotional support throughout this journey. I would especially like to thank Robert for his helpful discussions on dynamical diffraction, lessons in pickleball, keeping me company in Maryland, and more importantly for teaching me how to make the perfect cheesecake. Thank you to Kathryn Krycka, Jonathan Gaudet, and Paul Butler for making my SANS experiments possible, and to Mike Huber for providing me support no matter the instrument, country, or hour. I would also like to thank Dan Neumann and Robert Dimeo for making my research at the NCNR possible and for always approaching my research with excitement and encouragement. To Julie Borchers, you have been a very special mentor, without whom I would have been lost at times. While I cannot articulate to my satisfaction the crucial role you had during my studies and thereon, I will simply say your approach to research and people is inspiring and I look forward to working with you at NIST in the future. I would like to thank Martha Neviaser and Julie Keyser for their administrative support and tireless efforts to extend my many guest researcher agreements, and for ultimately ensuring I was able to continue my research during the pandemic. Finally, I would like to extend my most sincere gratitude to all of the truly exceptional instrument scientists whose profound insights/contributions and commitment to my research made all of my projects possible. It is one thing to have an exciting idea, but it is another thing to make it experimentally feasible. Lisa DeBeer-Schmitt, Jonathan White, and Elliot Gilbert, your shared love of neutrons and condensed matter and dedication to my research has far transcended the typical role of any collaborator, and I am deeply indebted to you all.

To my mentors at the NCNR, Shannon Watson and Wangchun Chen. I never thought I would be privileged enough to have such brilliant and supportive mentors and friends. Wangchun, your innovative approaches to polarized neutron physics and many encouragements have inspired me as a scientist and shaped me as a researcher. I am sure I will still be reaching out to you in my post-doc and I am excited for the opportunity to collaborate with you for many years to come. Shannon, firstly thank you for making sure that I did not starve throughout my Ph.D. and for introducing me to okra. Working with you and learning from you over the past few years has been my greatest honor. Whether it be you educating me on why peaches from South Carolina are far superior to those from Georgia, trying to not break down when I used iced tea and sweet tea interchangeably, or teaching me the art of polarized instrumentation and engineering, you always created a friendly and safe space for us to work and your support and friendship is the reason I may use the title Dr. You have been there through it all, times of success and what felt like utter defeat. You are my most trusted and colleague and greatest friend. PS: I will name one of your Helium cells one day. To Benjamin Heacock, you are the most gifted scientist I know. I will forever cherish the time I spent learning from you and will continue to wish that it could have been longer. Your patience as a teacher, insight as a scientist, and support as a friend is what kept me going through the hardest of times. Thank you for always standing up for me and for encouraging me in every way possible. I will miss our crazy collaborations, our adventures to Oak Ridge and Switzerland, and our many enthusiastic conversations spanning jazz to Nordic skiing. Your undeserved faith in me is the reason I may call myself a scientist and sorry for racking up your phone bills for our calls between America to Canada to discuss experiment ideas.

I would like to acknowledge the unconditional, and at times frustratingly optimistic, support offered by my friends and family. To my favorite physicist, Albert Lee, we have come a long way since our days of recreating Young's double-slit experiment using lasers in my moms living room. Your guidance and lessons always inspired my curiosity and have made me the physicist I am today. To my sister Jennifer, who has always thought I am smarter than I am. Your undeserved confidence in me kept me going through times of paralyzing self-doubt. Thank you for always looking out for me, challenging me outside of physics, and finding fun adventures for us to go on. To my brother-in-law, Chad, you have been a most reliable and dependable figure in my life. Your resounding faith in my pursuits and your hopeful outlook on life has taught me how to navigate many challenges and joys. Thank you for sitting through countless discussions of physics at Sunday dinners, for being my best taster of new recipes, and for always making me laugh. Our mutual bonding over the respective challenges and triumphs we have faced in becoming a pilot and physicist has served as some of my greatest moments of solace and excitement. I can't wait for the day when I get to be a passenger in your plane as you fly me to my next neutron experiment and for our future mountaineering trip in Switzerland. To my mom, you are the most courageous woman I know. The determination and work ethic you instilled in Jen and myself is the driving force behind all of our achievements. Your career as a pilot taught us adventure and the pursuit of the unknown and I am eternally grateful for your sacrifice as a single parent. Everything I am is because of you. Finally, to my partner, Trenton, I will never be able to fully articulate the support and strength you offered me during my Ph.D., so I will instead thank you for the hundreds of hours you spent listening to my many proposals/papers, for the weekends you dedicated to letting me discuss my experiment ideas, for inspiring me outside of physics, and for being my one constant during my many travels. You are my most valued critic and my greatest advocate, and I can't wait for our next adventure together, scientific or not.

I dedicate this to all of the fallen plants that died in my apartment so that I could perform my many neutron experiments abroad. Your sacrifice will never be forgotten.

Dedication

To my mom, Suzanne.

Table of Contents

List of Figures

List of Tables

Chapter 1

Introduction

1.1 Skyrmions and Topology

Topology, order, and symmetry are inextricably linked, inducing non-trivial phases and quasi-particle excitations which manifest exotic properties and new classification schemes for novel states of quantum materials [1, 2, 3, 4]. Topological phases and their transitions in condensed matter systems constitute a unique genre of quantum matter which transcend the traditional Landau-Ginsburg framework of continuous phase transitions [5, 6]. No longer marked by the onset of a spontaneously broken symmetry, these topological phases exhibit an emergence of non-trivial physical properties that cannot be described by a local order parameter, but must instead be described by a topological invariant [5, 7]. Perhaps one of the most seminal examples of such a system is that of a two-dimensional electron gas. When observed in a magnetic field applied normal to the gas plane, a vanishing longitudinal conductance was observed, accompanied by a quantized hall conductance [8, 9, 10]. The quantized hall conductance could only be described in terms of an integer which counts the number of conducting chiral channels at the edges of the system [8, 11, 12, 13, 14, 15, 16]. The existence of such topological states inspired exotic classification schemes of matter based on this new kind of topological order, where quantized observables are described by discrete topological invariants [17, 18, 19, 7].

Since then, topological phenomena have been predicted and observed in a myriad of systems spanning dislocations in condensed matter [19, 20] to skyrmions in particle physics [21], manifesting across a variety of physical degrees of freedom such as spin, space, energy, and momentum [22, 23, 24, 25, 26, 27]. Skyrmions, in particular, represent an especially prolific topological object; originally proposed as a topologically protected quasi-particle to describe the stability of hadrons through a non-linear sigma model [21], they have since been predicted and realized across diverse quantum states of matter such as superconductors [28, 29, 30], superfluids [31, 32], Bose-Einstein condensates [33, 34], liquid crystals [35, 36, 37], and magnets [38, 39]. In quantum magnets, skyrmions manifest in the winding degree of the magnetization, producing localized vortex-like spin configurations, characterized by an integer mapping to the unit sphere (Fig. 1.1). The number of times the physical space spanned by a 2D (x,y) plane of magnetization, $\mathbb{R}^2$, wraps the order parameter space of the surface of a 3D unit sphere, $\mathbb{S}^2$, denotes the topological charge of the skyrmion [40]. This integer topological charge mathematically forbids a continuous change of homotopy, introducing a finite energy barrier for topological transitions in a real physical system [41]. These localized topological features give rise to a myriad of protected states, non-equilibrium phenomena, and extreme dynamics [42, 43, 44, 45, 46, 47] with countless applications across information, sensing, and energy technologies [48, 49, 50, 51, 52, 53].

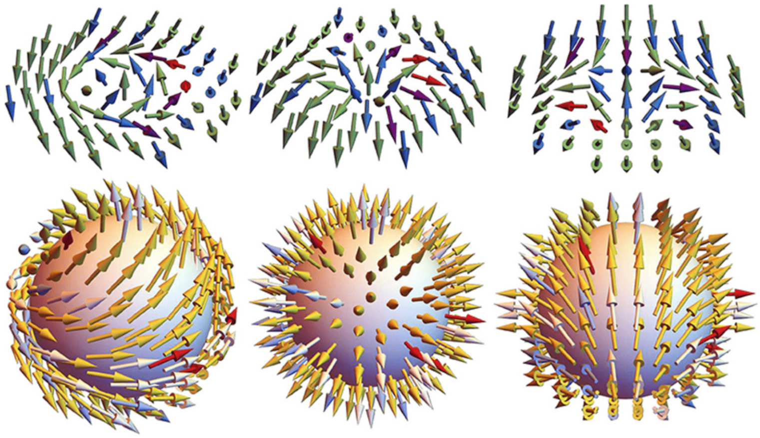

Figure 1.1: Illustrations of Bloch, Neél, and antiskyrmion spin textures (left-to-right) of polarity $p = 1$ and topological charge $Q = 1$ (left, middle) and $Q = -1$ (right). Their corresponding inverse stereographic projections are shown on the unit sphere. Reproduced from [54].

The local spin texture of an isolated skyrmion within a ferromagnetic background can be visualized by considering a smooth π rotation between upward pointing spins at the periphery, to downward pointing spins at the core, subtending a solid angle of 4π [55]. Integrating the magnetization density, $\boldsymbol{n}(\boldsymbol{r})$, over the solid angle defines the topological charge of a skyrmion as:

$$N_{Sk} = \frac{1}{4\pi} \iint_S \boldsymbol{n} \cdot \left(\frac{\partial \boldsymbol{n}}{\partial x} \times \frac{\partial \boldsymbol{n}}{\partial y} \right) d^2\boldsymbol{r} \tag{1.1}$$

Here, $\boldsymbol{n}(\boldsymbol{r}) = \frac{\boldsymbol{M}}{|\boldsymbol{M}|}$, describes the unit vector order parameter pointing in the direction of the magnetization, $\boldsymbol{M}$. Referring to Fig. 1.1, we can see that the various skyrmion configurations all wrap the unit sphere once, and so have a topological charge corresponding to $|N_{Sk}| = 1$. In contrast, topologically trivial spin textures, such as ferromagnetic states or helical configurations, would only map to one spin orientation or trace out a closed radial loop of spin orientations on the unit sphere, respectively, thus endowing them with a topological charge of 0. Structures possessing half-integer topological charges, so called merons and antimerons, where $\boldsymbol{n}$ rotates by $\frac{\pi}{2}$ from its center to its periphery, have also been observed in chiral lattice skyrmion hosting materials [56], in addition to a wide range of higher-order topological structures such as biskyrmions [57], thus emphasizing the rich zoology of topological spin textures and their transitions through fractionalization [58] and hybridization [56] pathways in chiral magnets.

While the topological charge of a skyrmion is paramount to its description, it is not sufficient to uniquely characterize the skyrmion state given the large degeneracy of skyrmion spin textures for a given topological charge. For the complete classification of a skyrmion spin texture we turn to additional magnetic degrees of freedom, such as helicity, polarity, and vorticity, which characterize the angle of the global rotation around the z-axis, the direction of magnetization at the skyrmion center, and the rotation direction of the in-plane spin components, respectively [54, 56]. These parameters distinguish various degenerate topological charge skyrmion spin textures from one another, such as Bloch, Néel and antiskyrmions (Fig. 1.1), which all possess a topological charge of $|N_{Sk}| = 1$ but maintain different helicities, polarities, and vorticities [54, 51] We can define these quantities by introducing polar coordinates, $\boldsymbol{r} = (r\ cos\varphi, r\ sin\varphi)$, and exploiting the circular symmetry of the magnetization to express a skyrmion as:

$$\boldsymbol{n}(\boldsymbol{r}) = (cos\Theta(\varphi)sin\Phi(r), sin\Theta(\varphi)sin\Phi(r), cos\Phi(r))\,. \tag{1.2}$$

Inserting this expression into equation 1.1, we obtain the skyrmion topological charge which can be evaluated in terms of r and φ as:

$$N_{Sk} = \frac{1}{4\pi} \int_0^\infty dr \int_0^{2\pi} d\varphi \left(\frac{\partial \Theta(r)}{\partial r} \times \frac{\partial \Phi(\varphi)}{\partial \varphi} \right) \tag{1.3}$$

$$N_{Sk} = \left[\cos\Theta(r)\right]_{r=0}^{r=\infty} \left[\Phi(\varphi)\right]_{\varphi=0}^{\varphi=2\pi} \tag{1.4}$$

Here, the topological charge is a function of both the out-of-plane, Θ, and in-plane, Φ, magnetization. Accordingly, one can define a skyrmion by supposing the spins point up at $r \to \infty$ and point down at $r = 0$, evaluating the first portion of equation 1.4 as $[\cos\Theta(r)]_{r=0}^{r=\infty} = 2$. Determining $\Phi(\varphi)$, however, requires the introduction of helicity, γ, and vorticity, m. The vorticity is defined by the integer, $m = [\Phi(\varphi)]_{\varphi=0}^{\varphi=2\pi}$. Therefore, the topological charge is determined by the product of the vorticity, m, and polarity, P, as $N_{Sk} = m \cdot P$. The helicity represents the phase difference that can appear in the rotation of the magnetization, $\Phi(\varphi)$, modeling the chirality of the magnetization as:

$$\Phi(\varphi) = m\varphi + \gamma. \tag{1.5}$$

Whereas the polarity and vorticity assume integer skyrmion values, the helicity is a continuous parameter which allows for skyrmions as intermediate states between Bloch and Néel spin textures. Using these quantities, we can rewrite the magnetization defined in equation 1.2 as:

$$\boldsymbol{n}(\boldsymbol{r}) = (sin(m\varphi+\gamma)cos\Phi(r), sin(m\varphi+\gamma)sin\Phi(r), cos\Phi(r))\,. \tag{1.6}$$

Together, these parameters uniquely define a host of skyrmion spin textures belonging to Bloch, Néel, and antiskyrmion configurations with various chiralities [51]. By homotopy theory and conservation of topological charge, it is apparent that topological transitions between skyrmion states and their competing helical, conical, and ferromagnetic $N_{Sk} = 0$ states, requires the presence of a topological defect to introduce a discontinuity into the material field. The discontinuous transition from $N_{Sk} = 1$ to $N_{Sk} = 0$ and vice versa, poses a topological energy barrier associated with the production of such a singularity. In real skyrmion systems, these defects are thought to be associated with magnetic Bloch points [59, 60] which may arise due to underlying crystalline or magnetic disorder, thermal fluctuations, and magnetic field tuning. This topological energy barrier associates stability and robustness against energetic perturbations which might otherwise disrupt topologically trivial states. As a result, skyrmions are said to be topologically protected, exhibiting exceptionally robust states, exotic emergent dynamics, and novel transport properties ideal for spintronic applications.

Magnetic skyrmions were originally predicted to spontaneously form in [61] chiral magnets through competing exchange interactions, namely ferromagnetic interactions and Dzyaloshinskii–Moriya interactions (DMI), within a finite temperature window. As a result, a range of cubic B20 helimagnets with non-centrosymmetric crystal structures, capable of stabilizing twisted magnetic states, were proposed as skyrmion-hosting candidate materials. Their discovery in real materials was marked by the small angle neutron scattering

(SANS) measurements performed in the A-phase of a bulk chiral itinerant-electron magnet MnSi [62]. Here, the broken inversion symmetry from the B20 crystal structure, belonging to symmetry class $P2_13$, and the resultant spin-orbit coupling, generates a DMI. The Hamiltonian is then comprised of three hierarchically ordered magnetic interaction terms with well separated interaction energies, since the latter two interactions are second- or higher-order perturbation terms of the spin-orbit interaction [63]. The competition between the strongest ferromagnetic exchange interaction, which favors co-linear spin arrangements, and second strongest antisymmetric DMI, which favors perpendicular alignment of the spin, stabilizes a spiral spin state with a periodicity decoupled from the underlying atomic lattice [62]. This long-range helimagnetic order is defined by a helical propagation vector, Q, pinned along the cubic space-diagonal $< 111 >$ by higher order spin-orbit coupling terms which represent the weakest interaction—anisotropic exchange. Application of a magnetic field unpins the helical propagation vector, Q, and aligns it parallel to the magnetic field, forming a triangular lattice skyrmion phase within a certain temperature-magnetic field (T-H) envelope [62]. Since then, magnetic skyrmions have been realized in variety of systems and forms, including artificial lattices [64], thin films at ambient conditions [65], and centrosymmetric systems stabilized by additional magnetic contributions such as geometric frustration or four-spin interactions mediated by itinerant electrons [66, 67, 68].

1.2 Skyrmion Stabilization

Skyrmion stabilization mechanisms are predominantly determined by the interplay of the systems various exchange interactions with additional contributions arising from the sample's dimensionality and geometry, such as coupling to surfaces/interfaces, skyrmion-skyrmion interactions, demagnetization, and confinement effects [69, 70, 71, 72, 73]. In noncentrosymmetric helimagnets, skyrmions are typically stabilized through competing DM and magnetic exchange interactions which stabilize helical ground states and skyrmion states in the respective absence and presence of an external magnetic field [40, 74]. These skyrmion states exist in a small region of the T-H phase diagram, stabilized by thermal fluctuations in equilibrium pockets just below the Curie temperature, T_c [62, 38, 75, 76, 77, 43]. In bulk systems, broken inversion symmetry of the underlying crystal lattice serves as the origin for the DMI, whereas in thin film systems an interfacial DMI arises from a lack of inversion symmetry at dissimilar interfaces of magnetic multilayers or from strong spin–orbit coupling at heterointerfaces [78]. However, skyrmions are not unique to acentric magnets; more recently, skyrmions have been observed in centrosymmetric systems that are not endowed with macroscopically subsisting DMI. In these cases, the skyrmions may be stabilized via alternative microscopic mechanisms such as geometrical frustration or multiple-spin interactions involving itinerant electrons [68, 79].

The diversity of skyrmion stabilization mechanisms has lead to their formation across a multitude of lengthscales, energetic phases, lattice structures, dimensions, magnetic orders, topologies, vorticities, and helicities, encompassing a rich collection of exotic topological magnetic configurations ranging from braided superstructures to topologically trivial skyrmioniums [80, 81, 82, 83, 84, 85]. Skyrmions may exist as isolated structures [86, 87] or form lattice arrangements in both two and three dimensions [59, 88]. Three-dimensional skyrmions may be visualized through the homogeneous extension of the two-dimensional skyrmion magnetization sheets into tube-like structures along the direction of the external magnetic field. These tube-like structures typically fall into two regimes on the basis of their sample thickness and surface-to-volume effects, exhibiting fundamentally different energetics, structures, and defects. In thin and confined systems, where the sample thickness is comparable to—or slightly greater than—the helical period, geometric constraints and reduced dimensionality imposed by a samples shape and thickness, have been shown to mediate a variety of surface and boundary related effects. Surface induced interactions/coupling, such as magnetic anisotropy and demagnetization effects, have been shown to affect skyrmion stability in cubic helimagnets [89, 90], while surface/boundary induced distortions like chiral twists, axial tube modulations, and pronounced edge states that have been observed to pin, nucleate, and destroy skyrmions across a myriad of systems [91, 70, 69, 73, 92, 93, 94, 95, 96, 97]. In contrast, bulk systems, where the sample thickness is much larger than the helical period, tend to be dominated by volume effects which favor skyrmion-skyrmion interactions and stabilization via the three-dimensional proliferation of defects [59]. As a result, bulk systems exhibit drastically different skyrmion shapes, structures, trajectories, defects, topological transition energy barriers and dynamics compared to confined systems [60]. Their added degrees of freedom, offer new skyrmion orientations and spatial morphologies, in addition to exotic transition pathways and emergent dynamics. Bulk systems have also been shown to host metastable skyrmion objects via rapid quenching of the equilibrium skyrmion phase [98, 99, 100]. These metastable objects exist over a drastically enhanced T-H window with unprecedented lifetimes and persistent memory effects [101, 71, 102]. This collection of properties make bulk skyrmion systems promising candidates for information carriers in future spintronic devices. For the purposes of this work, we will be primarily concerned with DMI stabilized skyrmion-hosting bulk cubic helimagnets.

The magnetic properties of solids originate from the spin degrees of freedom of electrons and their associated rotational motions. These two forms of rotation represent two distinct types of angular momentum. In the former, an intrinsic angular momentum is responsible for the electron spin, $\mathbf{s}$, while the latter represents an extrinsic form which generates an orbital angular momentum, $\mathbf{l}$. These forms of motion couple through spin-orbit interactions and generate magnetic moments whose collective contributions give rise to magnetism in samples. In accordance with quantum mechanics, we can associate magnetic dipole moments of $\mu_{\mathbf{l}} = \mu_B \mathbf{l}$ and $\mu_{\mathbf{s}} = -g\mu_B \mathbf{s}$ with the spin and orbital components, where $g = 2.0023$ is the relativistic gyromagnetic ratio of the electron and $\mu_B = \hbar e/2m_e$ represents the Bohr magneton, given an electron charge e and mass m_e. The total angular momentum for a free magnetic atom or ion is then given by

$$\mathbf{J} = \mathbf{S} + \mathbf{L} = \sum_i \mathbf{l}_i + \sum_i \mathbf{s}_i, \tag{1.7}$$

where quantum numbers J, L, and S can assume half-integer or integer values. This leads to a total magnetic moment of

$$\mathbf{M} = -\left\langle \sum_i \left(\mathbf{l}_i + 2\mathbf{s}_i\right) \mu_B \right\rangle, \tag{1.8}$$

where $\langle \sim \rangle$ represents the quantum mechanical expectation value.

The interaction energies of the magnetic moments are governed by the Hamiltonian of the system. Various interactions can arise depending on the composition, symmetry, and environment of the system. A magnetic moment, $\boldsymbol{\mu}$, in an external magnetic field, $\mathbf{B}$, will experience a Zeeman interaction which tends to align the magnetic moment along the direction of the external field, as described by the Zeeman Hamiltonian below:

$$H_{Ze} = -\boldsymbol{\mu} \cdot \boldsymbol{B}. \tag{1.9}$$

A combination of electrostatic forces and the Pauli exclusion principle gives rise to the Heisenberg exchange interaction,

$$H_{Ex} = J_{ex}\, \boldsymbol{S}_i \cdot \boldsymbol{S}_j. \tag{1.10}$$

Perhaps one of the most prolific interactions in magnets, this interaction favors collinear spins, $\boldsymbol{S}$, with positive and negative exchange constants, J_{ex}, corresponding to parallel and antiparallel spin alignments in ferromagnets and antiferromagnets, respectively. Since this interaction is short-ranged, typically one only needs to consider interactions between nearest neighbour spins. Together, these two interactions are sufficient to describe the behavior of ferromagnets and antiferromagnets.

To generate chiral spin textures, an additional term is needed which effectively twists the spin texture over some period. A combination of spin-orbit coupling and broken inversion symmetry produces a competing exchange interaction, known as the DMI, which favors perpendicular spin arrangements given by

$$H_{DM} = \boldsymbol{D}_{ij} \cdot (\boldsymbol{S}_i \times \boldsymbol{S}_j) \tag{1.11}$$

$\boldsymbol{D}_{ij}$ is the coupling vector which depends on the type of relativistic spin-orbit coupling present in the system, and therefore the symmetry of the magnetic exchange path between the two involved nearest neighbour spins [103]. Transverse and longitudinal DMI are responsible for Néel versus Bloch type skyrmion magnetizations [104]. Together, these energy contributions stabilize incommensurate magnetic ordering, such as helical, conical, and skyrmion states in bulk cubic helimagnets. In particular, the competition of the exchange and DM interactions favors canted spin ground states, stabilizing incommensurate spiral modulations just below T_c in zero field. These helical textures are characterized by a continuous rotation of spins orthogonal to a propagation vector, $\mathbf{q}$, forming single-harmonic modes with their rotation sense determined by the sign of the DM constant, D. The reduced strength of the DM interaction relative to the Heisenberg exchange interaction acts like a perturbation on the underlying dominant collinear spin structure, yielding modulated spin structures with propagation vectors much greater than the dimensions of the crystallographic unit cell. As a result the spin texture is said to be decoupled from its underlying atomic lattice. The helical periodicity may be defined from the helical wavevector $|\mathbf{q}| = D/J$, which is related to the helical wavelength, λ, by $q = 2\pi/\lambda$. These states are continuously degenerate with respect to the helical propagation directions, where $\mathbf{q}$ is typically pinned by magnetic anisotropy to lie along the easy axes [63, 105], such as the body diagonals in MnSi or the cubic axes in FeGe or Cu_2OSeO_3 [106].

Application of a magnetic field lifts the degeneracy, stabilizing conical modulations which acquire a canted angle as the magnetization vector rotates along the surface of the cone, combining the properties of the helical and ferromagnetic states. Reorientations of these chiral modulations have been observed upon changes in temperature and field [107, 108, 106, 109], mediating a variety of tilted one-dimensional spiral states and low-temperature skyrmion lattice states [110, 106, 111]. Competition between the Zeeman and magnetic anisotropy energies determines the critical field of the transition from the helical to conical spiral states [106]. Further increase in the magnetic field induces a transition from the conical state to a field-saturated ferromagnetic state above some critical value, while an increase in temperature above T_c produces a transition to a paramagnetic state (Fig. 1.2).

While the ferromagnetic, DM, and Zeeman interactions are on their own sufficient to

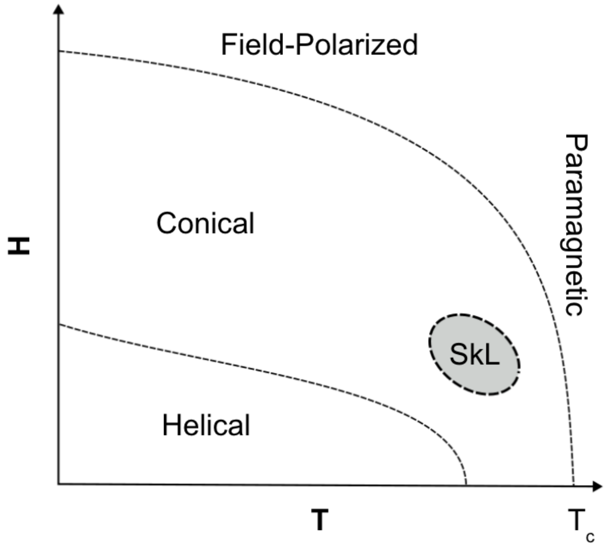

Figure 1.2: Typical temperature-magnetic field (T-H) phase diagram of a bulk DMI skyrmion lattice (SkL) material, illustrating the thermal equilibrium skyrmion lattice pocket just below the Curie temperature, T_c.

stabilize a skyrmion state, magnetocrystalline anisotropy has been shown to mediate exotic skyrmion ordering and domain dynamics [112, 113, 114], structural lattice transitions [115, 116, 99, 100], in addition to stabilizing a variety of novel low-temperature chiral and skyrmion states as mentioned above [117, 110, 111, 118, 106]. Magnetocrystalline anisotropy is rooted in spin-orbit coupling, where it represents the amount of energy required to overcome the coupling between the spin and the orbital motion of the electron while rotating a spin away from the easy axis of the magnetisation. Its energy density for a cubic system can be written as:

$$\frac{E}{V} = K_0 + K_1(\alpha^2\beta^2 + \beta^2\gamma^2 + \gamma^2\alpha^2) + K_2\alpha^2\beta^2\gamma^2 + \mathcal{O}^4, \tag{1.12}$$

where K_0, K_1, and K_2 are anisotropy parameters, α, β, and γ are the directional cosines, and $\mathcal{O}^4$ represents higher order terms. The relative strengths and signs of K_1 and K_2 determine the easy axis of the magnetic system [119]. Therefore, the delicate balance of these anisotropy constants, together with additional contributions such as magnetic disorder, effectively pin the helical propagation vectors, setting the orientation of the helical ground state relative to the crystal axes. Shape anisotropy effects arising from demagnetizing effects due to the shape of the sample have also been shown to influence skyrmion formation, shape, and stability [111, 72, 71].

These interactions can be modelled using the classical continuum model [40]:

$$H = \int \left[\frac{J_{ex}}{2} \left[\nabla \mathbf{n}(\mathbf{r}) \right]^2 + D\, \mathbf{n}(\mathbf{r}) \cdot \left[\nabla \times \mathbf{n}(\mathbf{r}) \right] - \mathbf{B} \cdot \mathbf{n}(\mathbf{r}) + K_E \right] d\mathbf{r}. \tag{1.13}$$

Here, D/J is small and the skyrmion size is sufficiently greater than the underlying atomic lattice period. As a result, we may treat the spin texture as a local spin texture, $\mathbf{n}(\mathbf{r})$, rather than individual spins. The first term represents the Heisenberg exchange interaction, with exchange constant J_{ex}, followed by the DM term, whose strength is given by the constant D. The third and fourth terms represent the Zeeman and anisotropy interactions, respectively. The ground state of equation 1.13 is a helical state, where the spin plane is perpendicular to $\mathbf{q}$, thereby minimizing the energy [40]. The triangular lattice skyrmion state can be viewed as a hybridized triple-$\mathbf{q}$ state consisting of the superposition of three helices perpendicular to the external magnetic field, each offset by 120 degrees relative to each other [40], satisfying the relation

$$\sum_{i=1}^{3} \mathbf{q}_i = 0. \tag{1.14}$$

The local spin texture, $\mathbf{n}(\mathbf{r})$, can be expressed as a sum of the background uniform ferromagnetic state and the helices as

$$\mathbf{n}(\mathbf{r}) \approx \mathbf{n}_{\mathbf{uniform}}(\mathbf{r}) + \sum_{i=1}^{3} \mathbf{n}_{\mathbf{q}_i}(\mathbf{r} + \Delta\mathbf{r}_\mathbf{i}), \tag{1.15}$$

where $\mathbf{n}_{\mathbf{q}_i}(\mathbf{r}) = A\left[\mathbf{n}_{i1}\, cos\left(\mathbf{q}_i \cdot \mathbf{r}\right) + \mathbf{n}_{i2}\, sin\left(\mathbf{q}_i \cdot \mathbf{r}\right)\right]$ represents the magnetization of a single helix of amplitude A and wavevector $\mathbf{q}_i$, possessing a phase $\mathbf{q}_i \cdot \Delta\mathbf{r}$. The two-dimensional Fourier transform of this magnetic structure manifests a hexagonal pattern, with the norm of the hexagon given by $|\mathbf{q}|$. As a result, the triangular lattice skyrmion phase has a distinct scattering signature in reciprocal space techniques, like SANS, for geometries where the skyrmion lattice is on the plane normal to the incident neutron wavevector.

1.3 Skyrmionic Topological Transitions Through Defects

Conduction electrons coupled to non-collinear spin textures acquire quantum mechanical phases [38]. In the case of skyrmions, this phase can be identified as a Berry phase that

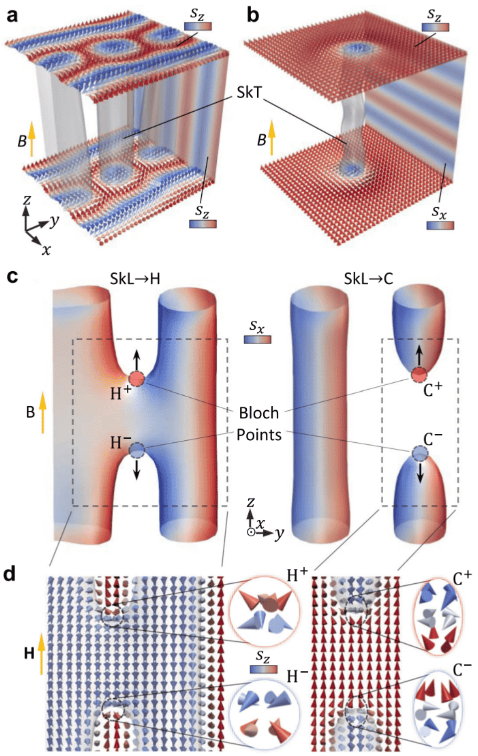

Figure 1.3: Three-dimensional visualisations of Bloch-point mediated skyrmion annihilation mechanisms through the helical (H) and conical (C) states from simulations (a,b). The grey contours represent the z-component of magnetization, $s_z = 0$. The back right surface of each simulation has been coloured according to the local s_z or s_x components respectively, highlighting the orientation of the surrounding helical and conical structures. Visualisations of the skyrmion to helical (SkL $\rightarrow$ H), and skyrmion to conical (SkL $\rightarrow$ C) annihilation mechanisms (c), showing the nucleation of a pair of Bloch points where either the SkT connects to the local helical structure (left, $H+$ and $H-$), or breaks in two to form the conical state (right, $C+$ and $C-$). d) Cross-sections of the spin texture around the Bloch-point structures shown in c). Insets display the local spin arrangement around each Bloch point. Colours indicate the m_z component. Reproduced from [60].

the spin of a conduction electron accumulates when following the magnetic texture adiabatically [59, 120]. This phase can be rewritten as an effective Aharonov–Bohm phase, associated with 'emergent' magnetic and electric fields, $\boldsymbol{B}^e$ and $\boldsymbol{E}^e$:

$$\boldsymbol{B}^e = \frac{\hbar}{2}\varepsilon_{ijk}\hat{n}\cdot(\partial_j\hat{n}\times\partial_k\hat{n}) \tag{1.16}$$

$$\boldsymbol{E}^e = \hbar\hat{n}\cdot(\partial_i\hat{n}\times\partial_t\hat{n})\,. \tag{1.17}$$

These emergent fields produce measurable phenomena such as the Topological Hall effect, ulta-low current drive of skyrmions, and emergent electromagnetic induction, making skyrmions objects easily controllable and manipulable for future spintronic applications [38]. Since the emergent fields measure the solid angle for an infinitesimal loop in space and space–time, $\hat{n} = (\boldsymbol{r}, t)$, $\partial_i = \partial_{r_i}$, and ε_{ijk} is the totally antisymmetric tensor. Integration of the skyrmion spin over the unit sphere associates one quantum of emergent magnetic flux with each skyrmion tube, where

$$\begin{aligned}\int \boldsymbol{B}^e\,d\sigma &= 4\pi\hbar,\\ &= \frac{-2\pi\hbar}{|q_e|}.\end{aligned} \tag{1.18}$$

The convention used here associates 1/2 (-1/2) charges with the conduction electrons of the majority (minority) bands. Because the emergent flux that defines skyrmions is quantized, their nucleation and termination is mediated by emergent magnetic charges that must also be quantized [59]. These emergent magnetic monopoles (MP)/ antimonopoles (AMP) can be identified as the source terms for the emergent magnetic field. As a result, any changes in topology are therefore thought to take place via emergent magnetic (anti)monopoles along the tubes depth, which act as sources or sinks for the quantized emergent magnetic skyrmion flux. In particular, the formation of monopoles at skyrmion branching and segmenting points and their motion along the tubes length in response to changes in external parameters, such as field or temperature conditions, have been proposed to drive a change in skyrmion topology through the unwinding of individual skyrmions [121, 60] and the zipping/unzipping of neighboring skyrmion tubes [59, 122, 60]. The emergent magnetic (anti)monopoles can be identified with real-space Bloch point magnetic defects which constitute topological singularities represented by points of vanishing magnetization where the magnetization rotates by 180 degrees in the space of a single spin. Since total emergent charge is conserved, skyrmionic transitions can only take place in three dimensions when emergent (anti)monopoles are either pinned to a material defect or jammed in place and unable to overcome the activation energy required to travel to the material surface or reach an oppositely-charged monopole to annihilate [123, 122, 69].

While skyrmions may conceptually extend uninterrupted along the entire depth of the crystal, real systems at non-zero temperatures contain a finite density of defects which disrupt the tubes propagation. Topological defects, like Bloch point magnetic defects, naturally occur on material defects and surfaces but are otherwise energetically-unfavorable in skyrmion-hosting material. These pre-existing topological defects may be associated with impurities or site-occupancy disorder which introduces local variations in exchange parameters. The variations may act as nucleating and pinning defects, stabilizing jammed states comprised of labyrinth and orientationally disordered chiral phases [112]. In the absence of such defects, there exists a finite energy barrier for (anti)monopole creation, owing to the discontinuous change in topology. Tuning the free energy contributions of external parameters to exceed the original spin-exchange interaction energy overcomes the topological energy barrier for MP/AMP creation, serving as an additional pathway for defect creation[124]. These free energy contributions may be thermal or field induced, creating (anti)monopoles in opposing pairs within the system or uniquely at the system's surface. While MP/AMP nucleation and propagation is known to stabilize thermodynamic skyrmion phases through thermal fluctuations, this mechanism was more recently used to explain the disentangling of jammed states during a magnetic field rotation ordering sequence [112]. Here, the proliferation of the MP/AMP pairs along various angular trajectories is thought to break up labyrinth states, with the final order of the skyrmion phase determined by the degree to which the monopoles propagated along the depth of the material. The final ordered phase would therefore be marked by the complete MP/AMP pair-annihilation or surface annihilation, leaving behind minimal (anti)monopole defect densities. In addition to magnetic field orientation, magnetic field magnitudes which are detuned above or below the ideal skyrmion value may also nucleate (anti)monopoles. Skyrmion annihilation upon field-increasing and field-decreasing conditions is thought to occur via disparate transition pathways, nucleating segmentation and branching monopoles, respectively [59].

A variety of Bloch-point mediated topological structures have been proposed and observed, ranging from interrupted segmenting and branching skyrmion string structures [59, 60, 122], to localized skyrmion filaments [125]. In the latter case, these localized skyrmion states may manifest as chiral bobbers [80] and magnetic torons [118, 109, 125] which represent surface-localized skyrmion stacks with continuously reducing diameters and finite penetration depths marked by termination on a Bloch point, and skyrmion fragments cupped by Bloch points on either end, respectively. However, existing studies of skyrmions and their defects are primarily limited to micrmomagnetic investigations and static imaging measurements in confined systems. Two-dimensional examinations of skyrmions have revealed a myriad of in-plane skyrmion string deformations including elongated structures [59] and bent skyrmion strings which terminate on the surface [92] or form at edges [69], in addition to chiral bobbers at the surface of FeGe lamellae [80]. Three-dimensional imaging in confined systems has revealed axial modulation of skyrmion tubes [70], while a recent study [126] confirmed the presence of interrupted and merging-type skyrmion strings in a sparsely populated micrometer sized thin plate needle-shaped sample of $Mn_{1.4}Pt_{0.9}Pd_{0.4}Sn$ using scalar magnetic X-ray tomography. The observations, however, are limited to individual skyrmion strings in a sample thickness only a few times the skyrmion tube diameters, whose confined geometry and thickness gradient fundamentally alters the skyrmions shape and behaviour; bulk lattice skyrmion behavior has yet to be experimentally observed.

1.4 Bulk Co-Zn-Mn Skyrmion Compounds

Practical implementation of skyrmions in future spintronic devices entails their stability and efficient control over a wide range of temperatures and fields, most notably room temperature and zero field. Integral to this, is a complete understanding of their dynamics and stabilization through defects in three dimensions as there should exist some optimal thickness and defect density for skyrmion stability and manipulation in three dimensions. While thin films have been shown to exhibit enhanced skyrmion equilibrium pockets owing to destabilized conical phases [76, 77], thicker regimes have revealed drastically reduced skyrmion drive current densities and impurity effects [91]. Defect-related pinning has similarly shown to play a critical role in skyrmion dynamics and stability, with disorder effects mediating a wide range of exotic phenomena and stabilization pathways. In particular, static persistent skyrmion signals/memory effects, and extended lifetimes have been associated with magnetic defects/disorder [118], whereas pinning has been shown to both facilitate and inhibit dynamics [46, 127, 128, 129, 130, 122], particularly topological transitions [59, 122, 60]. This competition between disorder and elasticity generates a complex energy landscape which promotes diverse skyrmion states with exotic dynamics. Characterization of the interplay of topological stability and skyrmion dynamics with disorder could be used to establish ideal defect densities for enabling skyrmion reorientations and enhancing stability, guiding the tailoring of future material parameters for spintronic applications.

The chemically doped $Co_xZn_yMn_{20-x-y}$ compositional series presents a unique platform to investigate skyrmion behaviour, owing to it's interplay of magnetic anisotropy, site disorder, and frustration, which generates diverse topological phases and lattice forms across thermal equilibrium and metastable minima in the free energy landscape at a variety of temperatures including room temperature [116, 99, 56, 75, 131, 132]. The Co-Zn-Mn alloys belong to the β-Mn-type family of cubic chiral magnets [75], with a different chiral space group from that of the traditional B20-type skyrmion-hosting compounds [40]. This family of intermetallics belongs to the $P4_132$ or $P4_332$ cubic chiral space group, depending on its handedness [133], and exhibits diverse properties and skyrmion phases depending on the degree of Mn-doping. The pure β-Mn compositional family has a unit cell which consists of 20 atoms distributed across 2 crystallographic sites; Co atoms occupy the 8c site, while and both Co and Zn atoms occupy 12d sites [133, 75, 134]. The chemically substituted ternary Co-Zn-Mn alloy system has been reported to be stable in a wide composition range $Co_xZn_yMn_{20-x-y}$ from $Co_{10}Zn_{10}$ to Mn_{20}, with T_c dependent on the composition ratio [134]. The end β-Mn system is a well established spin liquid arising from magnetic frustration amongst antiferromagnetically coupled Mn spins in the hyperkagome network of the 12d sites [135, 136]. The other end member binary $Co_{10}Zn_{10}$ alloy is a ferromagnet with T_c around 460 K, stabilizing a helimagnetic ground state under ambient conditions with a magnetic periodicity of 185 nm [75]. Partial substitution of Mn produces a rapid reduction in the magnetic modulation period and the paramagnetic-to-helimagnetic transition temperature, T_c [116], developing a spin-glass state in an x-region $3 < x < 6$ due to a combination of magnetic frustration inherent to β-Mn and magnetic disorder from competing ferromagnetic and antiferromagnetic Co and Mn spins [116, 137, 138]. Notably, $Co_8Zn_8Mn_4$ hosts a thermal equilibrium phase just above room temperature, making it an ideal candidate for spintronic applications under ambient conditions.

The properties of the chiral spin textures are set by the interplay of the magnetic energy terms which govern the system, in addition to various contributions such as disorder and shape effects. Tuning this complex energy landscape may be accomplished via changes in temperature, magnetic field, and/or chemical substitution, revealing a variety of skyrmion phases and lattice types. For example, the relative influence of the ferromagnetic exchange, DM, and anisotropic interactions can be varied via the manipulation of degrees of magnetic disorder through chemical substitution. Mn-doping in the Co-Zn-Mn intermetallic series has been shown to influence magnetic disorder, frustration and anisotropy, mediating skyrmion lattice transitions between triangular, rhombic, square, and disordered types. In particular, the cooperative enhancement of magnetocrystalline anisotropy and $\mathbf{q}$ value drives a triangular-square structural lattice skyrmion transformation in $Co_7Zn_7Mn_6$, $Co_8Zn_8Mn_4$, and $Co_9Zn_9Mn_2$ upon cooling [116, 99, 115] (Fig. 1.4). Magnetic frustration arising from the antiferromagnetic correlations of Mn spins dominates at lower temperatures, producing spin-glass states in $Co_7Zn_7Mn_6$ and $Co_8Zn_8Mn_4$ compounds, in addition to the stabilization of a disconnected thermal equilibrium phase in $Co_7Zn_7Mn_6$ [139, 140] far below T_c.

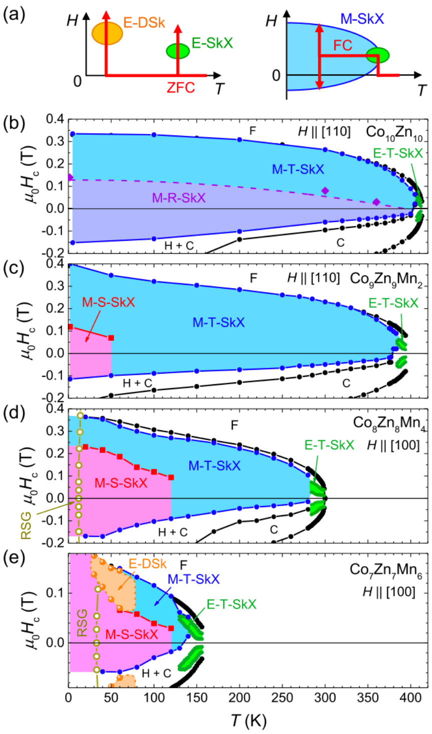

Figure 1.4: Summary of temperature-magnetic field (T-H) phase diagrams for equilibrium and metastable skyrmion states for (b) $Co_{10}Zn_{10}$, (c) $Co_9Zn_9Mn_2$, (d) $Co_8Zn_8Mn_4$, and (e) $Co_7Zn_7Mn_6$, produced from measurement processes illustrated by the state diagrams in (a). The following notations are used: H, helical; C, conical; F, ferromagnetic; E, equilibrium; M, metastable; T, triangular; R, rhombic; S, square; SkX, skyrmion crystal; DSk, disordered skyrmions; and RSG, reentrant spin glass. Reproduced from [116].

Rapid field-cooling (FC) processes, by way of the equilibrium skyrmion phase pocket, have been shown to stabilize metastable skyrmion states across triangular, rhombic, and square lattice types. Similar to glass transitions in liquids, these skyrmions exist in quenched states which kinetically avoid the skyrmion-to-conical transition pathway, forming metastable skyrmion strings. Metastable skyrmion phases have been universally found in skyrmion materials spanning MnSi to Cu_2OSeO_3 [100, 141, 122, 59, 118, 110, 142, 98, 38], exhibiting disorder dependent cooling rates and lifetimes governed by both the height of the decay energy barrier and the density of pinning sites [141, 101]. Since this state is not the energy minimum of the system, and so has a finite lifetime, there exists a topological energy barrier that must be overcome for skyrmion annihilation processes. This energy barrier scales with temperature, leading to observed skyrmion lifetimes in excess of a week [143, 141], with much greater lifetimes predicted theoretically [101, 116]. Defect pinning also serves to enhance skyrmion lifetimes and decrease cooling rates by inhibiting the proliferation of magnetic Bloch points—the mechanism by which skyrmions are proposed to decay. Whereas nominally disorder-free systems such as MnSi require rapid cooling rates on the order of hundreds of Kelvin per second to minimize any thermal fluctuations which could overcome the activation energy of topological transition between skyrmion-lattice and conical states [100, 141], doped systems such as Cu_2OSeO_3 and the Co-Zn-Mn series require only moderate cooling temperatures on the order of Kelvin per minute, owing to enhanced skyrmion stability through their pinning to impurities/defects [99, 71, 101]. Moreover, metastable supercooled states belonging to the Co-Zn-Mn alloys have also been demonstrated in thin-plate samples, showing L-shaped elongated skyrmions [117]. Similar exotic skyrmion structures in thin-plate Co-Zn-Mn skyrmion samples have been observed spanning smectic liquid-crystalline arrangements of skyrmions in $Co_{8.5}Zn_{7.5}Mn_4$ [144], to in-plane string defects in $Co_9Zn_9Mn_2$ [92], to skyrmion chains and meron-antimeron square lattices in $Co_8Zn_9Mn_3$, stabilized by in-plane shape anisotropy [56]. Together, this collection of exotic defects, structures, dynamics, and tunable energetics makes the Co-Zn-Mn a rich platform from which to study, guiding the future development and manipulation of skyrmions for spintronic applications.

Chapter 2

Theoretical Formalism and Experimental Techniques

2.1 The Neutron and Its Interactions

The neutron possesses a unique collection of properties that endows it with extraordinary sensitivity and novel probing abilities, making it an ideal test particle of fundamental/exotic physics and an unmatched tool for material investigations. The neutron is a composite spin 1/2 particle, which has a mass of $1.674928(1) \times 10^{-27}$kg and carries a magnetic moment of -1.9130427(5) nuclear magnetons. While electrically neutral, the neutron is composed of charged quarks with an asymmetric distribution which generate a radial charge distribution [145] that lends itself to fundamental studies of nucleon dynamics [145]. Free neutrons are unstable with a lifetime of approximately 15 minutes, after which time they undergo β decay into a proton, an electron, and an antineutrino, mediated by the weak interaction. Studies of the neutron lifetime have powerful implications for physics beyond the standard model, with measurements ranging from verification of Big-bang nucleosynthesis (BBN) through predictions of primordial light element abundances [146], to examinations of V-A structure of the weak interaction and the quark-mixing Cabibbo–Kobayashi–Maskawa (CKM) matrix [147]. In matter, neutrons are subject to short-range nuclear forces, scattering from nuclei primarily through the strong force. Longer range dipole-dipole interactions between the magnetic moment of the neutron and unpaired electrons produce magnetic scattering interactions on the same order of magnitude as the nuclear contribution [148]. We will neglect contributions from additional electromagnetic interactions as they are typically two orders of magnitude smaller than the magnetic dipole interaction. Neutrons therefore provide experimental access to all of the four fundamental forces, with promise of sensitivity to a fifth force [149], spanning an extraordinary range of lengthscales and timescales with a unique hierarchy of energies. This collection of properties makes neutrons an invaluable tool for interferometric, spectroscopic and scattering investigations of fundamental physics and quantum materials, unrivaled in their sensitivity and diversity of interactions. Existing studies encompass foundational tests of quantum mechanics, such as entanglement [150, 151] and the 4π symmetry of fermions [152, 153], to hypothetical beyond-standard-model interactions and dark sector models [154, 155, 156], to explorations of emergent and exotic magnetism [157, 158, 59]. Additionally, neutrons have demonstrated unique promise in quantum information models of dynamical diffraction, enabling new approaches to complex diffraction problems and the design of novel neutron optical elements [159, 160, 161, 162, 163].

According to the wave-particle duality, the de Broglie wavelength of the neutron with mass m and momentum p, is given by:

$$\lambda = \frac{h}{p}, \tag{2.1}$$

where h represents Plank's constant. Alternatively, a neutron with wavevector $\mathbf{k} = 2\pi/\lambda$ may be expressed in terms of its momentum,

$$\mathbf{p} = \hbar\mathbf{k}, \tag{2.2}$$

where $\hbar = h/2$ is the reduced Plank's constant. The energy of the neutron can then be expressed in terms of these quantities as:

$$E = \frac{p^2}{2m} = \frac{h^2}{2m\lambda^2} = \frac{\hbar^2 k^2}{2m}. \tag{2.3}$$

Neutron matter wave fields $\Psi(\boldsymbol{r}, t)$ can be described by the Schrödinger equation:

$$\mathcal{H}\Psi(\boldsymbol{r}, t) = \left(-\frac{\hbar^2}{2m}\nabla^2 + V(\boldsymbol{r}, t)\right)\Psi(\boldsymbol{r}, t) = i\hbar\frac{\partial\psi(\boldsymbol{r}, t)}{\partial t}, \tag{2.4}$$

where $\mathcal{H}$ is the Hamiltonian and $V(\boldsymbol{r}, t)$ is the external potential. This is a linear equation which can be solved in free space using the plane wave Ansatz

$$\Psi(\boldsymbol{r}, t) = e^{i(\boldsymbol{k}\cdot\boldsymbol{r} - \omega t)}, \tag{2.5}$$

where $\omega = E/\hbar$. For purposes of this thesis, we will be concerned only with stationary situations in which there are time-independent potentials, $V(\boldsymbol{r})$. In these cases, equation

2.4 can be solved using the method of separation of variables, where $\Psi(\boldsymbol{r},t) = \psi(\boldsymbol{r})\psi(t)$. This yields solutions of the form

$$\Psi(\boldsymbol{r},t) = \psi(\boldsymbol{r})e^{\frac{-iE}{\hbar}t}, \tag{2.6}$$

where $\psi(\boldsymbol{r})$ satisfies the the time-independent Schrödinger equation given by:

$$\left(-\frac{\hbar^2}{2m}\nabla^2 + V(\boldsymbol{r})\right)\psi(\boldsymbol{r}) = E\psi(\boldsymbol{r}). \tag{2.7}$$

The exponential term represents the unitary time-evolution operator. This equation is a Helmholtz scalar wave equation which can be re-written in close mathematical analogy to the optics of electromagnetic waves as

$$\nabla^2\psi(\boldsymbol{r}) + K^2(\boldsymbol{r})\psi(\boldsymbol{r}) = 0. \tag{2.8}$$

$K(\boldsymbol{r})$ is the spatially dependent wavevector in the region of the potential, defined by

$$K^2(\boldsymbol{r}) = \frac{2m}{\hbar^2}\left[E - V(\boldsymbol{r})\right]. \tag{2.9}$$

As mentioned earlier, the neutron interacts via all four fundamental forces, therefore a variety of potentials may exist in equation 2.7 ranging from gravitation to Coriolis [164]. Neutron-matter interactions, are typically dominated by short-range strong nuclear forces which can be described by the point-like Fermi pseudopotential for each nucleus at site $\boldsymbol{r}_j$, such that

$$V_{nuc}(\boldsymbol{r}) = \sum_j \frac{2\pi\hbar}{m}\, b_c\, \delta\left(\boldsymbol{r} - \boldsymbol{r}_j\right), \tag{2.10}$$

where δ is the three-dimensional Dirac delta function. Here, the true strong neutron interaction is replaced by a small interaction potential which leads to a correct s-scattering amplitude in the first Born approximation. This approximation is valid for thermal neutrons in which the range of the strong nuclear force, which roughly corresponds to the nuclear radius R and is typically on the order of fm, is much smaller than the de Broglie wavelength, λ. In such cases, the scattering interaction is characterized by a single parameter, b_c, which describes the scattering length. Expanding this potential to a real material which consists of an assembly of nuclei— averaging over a macroscopic volume—the potential scales to an effective optical potential,

$$V_{nuc}(\boldsymbol{r}) = \frac{2\pi\hbar^2}{m}\, b_c\, N, \tag{2.11}$$

where N is the atom density and b_c is the scattering length density of the material. Note that in the case of absorption processes, the scattering length density becomes complex valued. This optical potential generates a material index of refraction at a vacuum-solid interface as governed by Snell's Law,

$$n = \frac{k}{k_0} = \frac{v}{v_0} = \frac{sin(\gamma_0)}{sin(\gamma)}, \tag{2.12}$$

where an incident ray of wavevector $\boldsymbol{k}_0$ makes an angle γ_0 with the surface normal, and the refracted ray inside the medium of wavevector $\boldsymbol{k}$ makes an angle γ with the surface normal. Expressing this equation in terms of material properties, given the definition of k in equation 2.9 yields:

$$n = \sqrt{1 - \frac{V}{E}}, \tag{2.13}$$

This can also be directly seen from a first order expansion of the refractive index n, in terms of neutron momentum,

$$n = \frac{p}{p_0} = \sqrt{\frac{p_0^2 - 2mV_0}{p_0^2}}. \tag{2.14}$$

Neutron optical potentials are typically on the order of 100 nV, while cold neutrons have kinetic energies on the order of 10 meV. Using $E_{kin} = 10^6 \times V_0$, the first order expansion of equation 2.14 yields

$$n \simeq 1 - \frac{V_0}{2E_{kin}} = 1 - \frac{\lambda^2 N b_c}{2\pi}. \tag{2.15}$$

From here, we observe that the refractive index n is very close to unity, with $n \sim 1 - 10^{-6}$ for cold neutrons and $n \sim 1 - 10^{-5}$ for thermal neutrons. This is in stark contrast to photons in the optical regime, which exhibit refractive indices upwards of 1.5 for insulating materials [164]. While this property makes refraction at large angles unfeasible, the exceptional precision and control of neutron deflection at small angles is realizable, through refracting prisms for example [165, 166]. Total external reflection at surfaces for angles less than the critical angle θ_c is another consequence of equation 2.15. For thermal neutrons, this angle is typically less than 0.3°, while for ultra-cold neutrons the critical angle can reach 90° [164], enabling neutron storage and trapping methods for times which are only limited by the neutrons β decay lifetime [167]. These devices have expansive applications for particle physics and cosmology, namely involving precision measurements of the neutron lifetime and electric dipole moment (EDM) [147, 168, 169].

Until now, we have excluded magnetic-based neutron interactions, however, the relatively large intrinsic magnetic moment of the neutron couples to unpaired electrons from the magnetic atoms. In magnetic materials, the neutron interacts with the magnetic induction field, $\boldsymbol{B}$, via its magnetic dipole moment, $\boldsymbol{\mu}$, by

$$V_{mag}(\boldsymbol{r}) = -\boldsymbol{\mu} \cdot \boldsymbol{B}(\boldsymbol{r}) = -\mu\boldsymbol{\sigma} \cdot \boldsymbol{B}(\boldsymbol{r}), \tag{2.16}$$

where we have expressed magnetic dipole moment of the neutron in terms of the Pauli spin operator $\boldsymbol{\sigma} = (\sigma_x, \sigma_y, \sigma_z)$. Expanding equation 2.16 in terms of the Pauli spin matrices and magnetic dipole momentum $\boldsymbol{\mu} = -\gamma\mu_N\boldsymbol{\sigma}$, where μ_N is the nuclear magneton and $\gamma = 1.832 \times 10^8\ T^{-1}s^{-1}$ is the neutron gyromagnetic ratio, yields:

$$V_{mag}(\boldsymbol{r}) = \frac{-\hbar\gamma}{2}\left(\sigma_x B_x + \sigma_y B_y + \sigma_z B_z\right), \tag{2.17}$$

where the Pauli spin matrices are

$$\sigma_x = \begin{pmatrix} 0 & 1 \\ 1 & 0 \end{pmatrix},\ \sigma_y = \begin{pmatrix} 0 & -i \\ i & 0 \end{pmatrix},\ \sigma_z = \begin{pmatrix} 1 & 0 \\ 0 & -1 \end{pmatrix}. \tag{2.18}$$

This potential underpins the magnetic-neutron interaction, serving as the basis for magnetic neutron scattering as we shall see in section 2.1.4.

2.1.1 Quantum Phase Shifts

Phase is a universal quantum property of a wavefunction, required for the existence of interference and diffraction effects. The neutron wavefunction can be modified in phase by various means, involving nuclear, magnetic, electric, or gravitational potentials. This feature serves as the basis of perfect crystal neutron interferometry and grating interferometry techniques [170, 171, 172, 173, 174, 175, 176, 177, 178]. The quantum phase $\boldsymbol{\Phi}(\boldsymbol{x}, t)$ of a matter wave evolving in space and time can be defined according to the Feynman-Dirac path integrals along trajectories defined in classical mechanics. This is equivalent to the eikonal approximation used in geometrical optics, which states that neutron rays are the classical trajectories of neutrons, and is valid for neutrons when the potential is slowly varying compared to the neutron wavelength. The neutrons phase can then be expressed as the path integral over the Lagrangian, $\mathcal{L}$, in space-time, given by

$$\boldsymbol{\Phi}(\boldsymbol{x},t)=\frac{1}{\hbar}\int\mathcal{L}dt'. \tag{2.19}$$

The Lagrangian, $\mathcal{L}$, is related to the Hamiltonian H by a Legendre-transformation,

$$\mathcal{L}=\boldsymbol{p}\cdot\boldsymbol{v}-\mathcal{H}. \tag{2.20}$$

Substituting equation 2.20 into equation 2.19 yields

$$\boldsymbol{\Phi}(\boldsymbol{x},t)=\frac{1}{\hbar}\int_{x_0}^{x}\boldsymbol{p}\cdot d\boldsymbol{s}-\frac{1}{\hbar}\int_{t_0}^{t}\mathcal{H}dt'=\int_{x_0}^{x}\boldsymbol{k}\cdot d\boldsymbol{s}-\int_{t_0}^{t}\omega dt'. \tag{2.21}$$

Here, we consider only energy conserving potentials and ignore the second term which results in a global phase. A stationary phase shift is represented by a potential $V(x)$, which changes the momenta in accordance with energy conservation as

$$\frac{(p+\delta p)^2}{2m}+V(x)=E\Rightarrow v\cdot\delta p\approx -V(x) \tag{2.22}$$

given a the "golden rule" of small perturbations. The relative phase shift $\Delta\phi$, which corresponds to the induced phase shift in the material relative to the phase shift in free space, becomes

$$\Delta\phi=\frac{1}{\hbar}\int_{t_0}^{t}\delta p\cdot v dt'\approx -\frac{1}{\hbar}\int_{t_0}^{t}V dt'=-\frac{1}{\hbar v}\int_{x_0}^{x}V dx. \tag{2.23}$$

As per convention, we shall use ϕ to denote $\Delta\phi$. Equivalently, using equation 2.11 for a generalized scattering length, the phase shift can be expressed as

$$\phi=\lambda\int dl\langle b\rangle, \tag{2.24}$$

where $\langle b\rangle$ is the scattering length density of the sample. Therefore the nuclear phase shift that a neutron accrues when traveling along the $\hat{z}$ direction through a material is given by

$$\phi=\frac{2\pi N b_c D}{k_{z0}}. \tag{2.25}$$

The corresponding evolution of the neutron wavefunction is found by integrating over the potential as follows:

$$\Psi_{out}(z)=\psi_{in}(z)\int_{-\infty}^{\infty}e^{\frac{-i}{\hbar}\int_{t_0}^{t}V dt}dk_z=\psi_{in}(z)\int_{-\infty}^{\infty}e^{-i\frac{N b_c D 2\pi}{k_z}}dk_z\approx\psi_{in}(z)e^{-i\frac{N b_c D 2\pi}{k_{z0}}}=\psi_{in}(z)e^{i\phi}. \tag{2.26}$$

Similarly, the phase accumulated by a neutron with magnetic dipole moment, $\boldsymbol{\mu}$, in a magnetic field, $\boldsymbol{B}$, is given by

$$\phi = \lambda \langle b_M \rangle \int dl \; \boldsymbol{\sigma} \cdot \boldsymbol{B}. \tag{2.27}$$

We can consider the case of the neutron spin aligned parallel and anti-parallel to the external magnetic field, in which case equation 2.27 reduces to

$$\phi = \pm \frac{u_N B m_n \lambda l}{2\pi \hbar^2}, \tag{2.28}$$

where the ± sign is due to Zeeman splitting of the spin-up and spin-down states, m_n is the mass of the neutron, and l is the path length through the magnetic field. The corresponding unitary operator which describes the time evolution of the neutron spin in a magnetic field can be computed from equations 2.16 and 2.23, as

$$\hat{U}_m = e^{-\frac{i}{\hbar}\int_{t_0}^{t} V_{mag}\, dt'} = e^{i\frac{\gamma t}{2}\boldsymbol{\sigma}\cdot\boldsymbol{B}}. \tag{2.29}$$

Alternatively, the operator can be computed from the exponential term in equation 2.26,

$$\hat{U}_m = \mathcal{T}\{e^{-i\int \mathcal{H}\, dt'}\}, \tag{2.30}$$

where $\mathcal{T}\{...\}$ denotes the time-ordered product. Taking the first order term in the Dyson series expansion of equation 2.30 yields the infinitesimal time evolution operator:

$$\hat{U}_m = 1 - i\mathcal{H}dt. \tag{2.31}$$

2.1.2 Topological Phase Shifts

Topological states, characterized by phase singularities, such as vortices, are inherent to any wave phenomena spanning light [179, 180, 181, 182, 183] to electrons [184, 185]. These states manifest helical wavefronts with phase singularities that describe a quantized form of azimuthal motion, known as orbital angular momentum (OAM). Therefore, just as quantum particles, such as photons and electrons, can possess linear and spin angular momentum, they are also capable of hosting a quantized topological genre of momentum, OAM. Note that this form of OAM is not to be confused with the OAM associated with the motion of electrons around the atomic nucleus in atoms and molecules [186]. This twisted property can be expressed as an azimuthal phase dependence in which the wavefunction varies as $e^{il\phi}$, yielding quantized values of OAM equal to $l\hbar$, where l is the OAM value which corresponds to the topological charge of the centre phase singularity and ϕ denote the azimuth around the propagation axis [186, 187]. The topological charge of the phase is given by

$$l = \frac{1}{2\pi} \times \oint_C \nabla\varphi(\boldsymbol{r})dr, \tag{2.32}$$

which counts the number of 2π phase jumps for a tiny closed loop surrounding the singularity, C. This phase singularity produces a ring-like "doughnut" intensity pattern upon propagation to the far field [186].

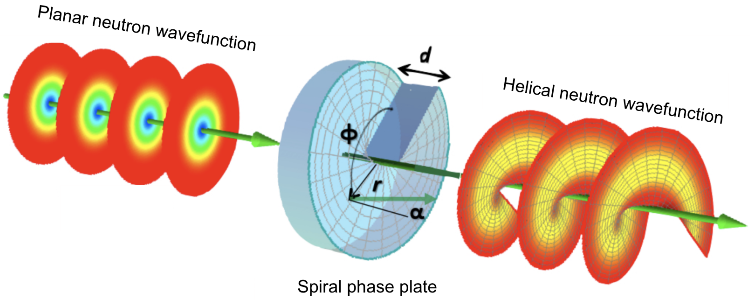

Figure 2.1: Illustrations showing the conversion from incident plane wavefronts to helical wavefronts using a spiral phase plate. Adapted from [188].

These states present novel avenues for the generation of selective probes, providing unprecedented access to structures and interactions spanning nuclear physics to vision sciences [189, 190, 191, 192, 193]. For neutrons, the realization of OAM states provides a new degree of freedom and subspace from which to explore fundamental interactions and topological material properties, spanning gravity to magnetism. This mode also offers topological protection from noise, inspiring various applications for non-trivial neutron propagation techniques and quantum information science. The coherent control of neutron OAM holds special promise for the study of topological structures and excitations in materials. Here, the coherent diffraction and interference of neutron OAM states from topological material states across imaging and scattering techniques could serve as a direct and novel route of characterizing defect densities, topological charge, correlation lengths, and phase transitions for a myriad of systems. Moreover, examining the dynamics of topological-to-neutron sample interactions and incorporating spin couplings could unveil exotic interactions and excitations such as magnon-OAM transfer and controlled rotations of bulk nanometric magnetic structures.

The generation of neutron OAM states was recently accomplished through a spiral phase plate (SPP) in which the thickness of the device varies uniformly as a function of the plate's azimuthal angle, ϕ, as $h = h_0 + h_s\phi/2\pi$, where h_0 is the base height and h_s is the step height (see Figure. 2.1) [194]. Given equation 2.25, the azimuthal phase shift can be calculated as

$$\phi = -Nb_c\lambda \left(h_0 + h_s\phi/2\pi\right). \tag{2.33}$$

The wavefunction after passing through the SPP, Ψ', can therefore be expressed as $\Psi' = e^{i\phi}\Psi$. Using this technique, the average OAM of the beams was measured for various topological charges using a perfect-crystal neutron interferometer to image the phase profile [194]. Since then, numerous demonstrations of neutron OAM have been proposed and performed [195, 196], including generations of spin-orbit coupled neutron beams and their lattices [197, 198]. These beams present unique opportunities to study quantum materials which exhibit similar correlations between spin and OAM, such as magnetic topological materials like skyrmions. However, existing techniques entail the manipulation of the average neutron OAM value, with the creation of a neutron state with helical wavefronts dominated by a single OAM value remaining elusive. Moreover, current generation techniques suffer limitations in the production of OAM lengthscales below hundreds of microns, severely restricting the accessible lengthscales that can be probed and making these techniques incompatible with nanometric studies of quantum materials. Overcoming these challenges is critical to realizing tunable implementations for quantum material characterization applications.

2.1.3 Neutron Scattering

Neutron scattering is a powerful experimental technique ideally suited for structural and dynamical studies of condensed matter by way of the neutrons nuclear/magnetic properties and its broad tunability in energy. The weak interactions and electric neutrality of the neutron enables high penetration depths into materials, making neutron scattering a non-destructive bulk probe of materials unparalleled by X-rays or electrons. While this property is clearly desirable for studies of quantum materials, it is also quite attractive for the fabrication of complex sample environments. Since neutrons penetrate robust materials such as silicon, quartz, and sapphire, and heavy elements like aluminum and titanium, we may utilize demanding and bulky setups with sizeable amounts of material in the beam, such as in cryogomagnets and rheological devices—setups that are non-trivial for conventional electron and X-ray diffractive techniques. The implementation of these vast sample environments enables in situ real-time investigations of soft and hard materials spanning temperatures from 35 mK - 2270 K, magnetic fields exceeding 13 T, and a range of high-pressure environments, electric fields and current pulses, and internal stresses, amongst others.

Since the neutron interacts weakly with matter, each neutron normally only scatters once in the sample volume such that it is strong enough to be measured, while still being weak enough so as to not disturb the system too severely. The de Broglie wavelength of thermal neutrons is on the order of the interatomic distances in solids, while its energy and momenta match the atomic and magnetic excitations in condensed matter, making interference effects possible [199]. The high tunability of the energy of neutrons through moderation processes, spanning 0.1 meV to 100 meV for cold to thermal neutrons, respectively, [200], enables nuclear and magnetic structural investigations across angstrom to micrometer lengthscales. While discussions of neutron scattering applications to soft matter are excluded in this thesis, it should be noted that small angle scattering techniques are particularly suited for microstructure investigations of soft materials [201, 202, 203, 204]. These studies range from characterizing the structural parameters of particulate systems like surfactants and polymers [205], to uncovering diffusive motions of biological macromolecules [205]. Furthermore, the isotopic sensitivity of the neutron enables contrast matching studies through selective deuterium labelling which may be used to highlight structural details or tag molecules to study dynamic processes [205] such as phase behavior and molecular conformation, in both solutions and the bulk [206]. Therefore, neutrons are able to provide deep insights into the nuclear and magnetic structural and dynamical properties of bulk materials, endowing it as a highly versatile tool across a wide range of systems and sample environments.

Scattering Geometry and Cross-sections

A typical neutron scattering experiment involves preparing an incident beam of neutrons with a well-defined wavevctor $\mathbf{k}_i$ and flux $\phi_i(\mathbf{k}_i)$, through various collimation and monochromating techniques, to scatter from a sample of interest. The scattered neutron properties such as energy and momentum may be analyzed to deduce the structural and dynamical properties of the interacting sample. The incident neutron flux is defined as the number of neutrons, n, passing through a unit area per second (typically expressed in n/cm^{2}s), with the surface area being perpendicular to the incident neutron beam. This can be nicely represented by the differential scattering cross-section, which describes the phase space density of the scattered current. Disregarding changes in energy and momentum, we can define the systems collective ability to scatter neutrons using the total neutron scattering cross section given by $\sigma_{tot} = 1/\phi_i$ (which has units of area). However, the interaction of the beam with the sample will scatter the neutrons into a small volume of the phase space, at a wavevector $\mathbf{k}_f$. As a result, we must introduce the differential scattering cross-section, which is defined by the the ratio of this scattered current density to the incident neutron flux density and incorporates the angular dependence of the scattered state in terms of a solid angle $d\Omega$ in the direction θ and ϕ. For elastic scattering, the differential scattering cross-section is defined as

$$\frac{d\sigma}{d\Omega} = \frac{C}{\eta\Phi\Delta\Omega}, \tag{2.34}$$

where C is the measured count rate at the detector which subtends a solid angle of $\Delta\Omega$, with an efficiency η. For inelastic scattering, we use a double differential cross-section,

$$\frac{d^2\sigma}{d\Omega dE_f} = \frac{C}{\eta\Phi\Delta\Omega\Delta E_f}, \tag{2.35}$$

which describes the scattering interaction in terms of a final energy, E_f, and the interval of energy transfer in the detector, ΔE_f. The scattering geometry, and various scattering processes are illustrated below in Fig. 2.2. The phase space element in a beam can then be defined as the product of the collimation solid angle, the width of the energy distribution, and the beam cross-section.

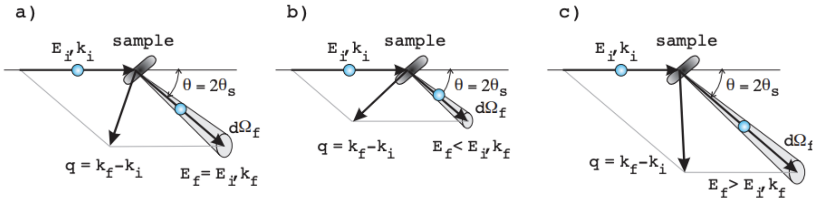

Figure 2.2: Schematics depicting typical neutron scattering modalities, such as elastic neutron scattering (a), and inelastic scattering with neutron energy loss (b) and gain (c). Reprinted with permissions from [207].

The changes in neutron energy and momentum are governed by conservation laws,

$$\mathbf{Q} = \mathbf{k_i} - \mathbf{k_f}, \tag{2.36}$$

$$E = E_f(\eta_f) - E_i(\eta_i), \tag{2.37}$$

$$E = \frac{\hbar^2}{2m_n}(\mathbf{k}_i^2 - \mathbf{k}_f^2), \tag{2.38}$$

which determine the scattering triangles of Fig. 2.2. An intuitive understanding of neutron diffraction from crystalline materials may be given in the context of Bragg's Law, in which constructive interference of waves scattered from adjacent planes of atoms at a scattering angle, θ, only occurs when the path length difference is an integer multiple of wavelength, λ. Bragg's Law is mathematically expressed as $n\lambda = 2dsin(\theta)$, where n is an integer and d is the lattice plane spacing. Alternatively, this may be derived by considering the scattering triangle given by $\mathbf{Q} = \frac{4\pi}{\lambda}sin(\theta)$, in combination with the condition for constructive interference given by $\mathbf{Q}\,d = 2\pi n$, where $\mathbf{Q}$ is perpendicular to the two scattering planes. Neutron diffraction therefore produces Bragg peaks which correspond to each set of lattice planes, denoted by three Miller indices (h, k, l), yielding information on the microscopic structure of the material. These need not be limited to atomic-scale structures; neutrons can diffract from a variety of periodic nuclear and magnetic structures, exceeding micrometer lengthscales, limited by the lower energy limit of conventional moderation processes.

The total cross-section, σ_{tot}, is therefore obtained upon integration of equations 2.34 and 2.35:

$$\sigma_{tot} = \int \frac{d\sigma}{d\Omega} d\Omega = \iint \frac{d^2\sigma}{d\Omega dE_f} d\Omega dE_f = \frac{C}{\eta\Phi}, \tag{2.39}$$

It should also be noted that in this discussion we have considered ideal beams of neutrons, whereas in real-life experiments we must consider distributions in neutron energy and momentum, centered on some mean value. Optimization of these beams depends on the competition between the resolution requirements and flux/counting time considerations of the experiment. Too strict of collimation, and therefore resolution, will lead to a fruitless loss of neutrons and degradation of statistics. Conversely, while a reduction in collimation offers enhancements in flux, the loss in instrument resolution can smear the signal. Recent advancements in high-transmission neutron optical focusing methods have been made using micro-machined triangular array refractive prisms [208], however, these devices are not yet ready for widespread implementation on SANS beamlines.

Scattered State

This section largely follows from Sears [148]. The scattered neutron state can be computed as a simple solution of the Schrödinger equation involving perturbation theory, as described here. We begin with equation 2.4. Considering only time-independent potentials, we arrive at stationary solutions of the form shown in equation 2.6. The task of determining the scattered state therefore equates to finding the eigenfunctions, $\psi(\mathbf{r})$, which satisfy equation 2.7. Since the incoming and outgoing neutron particles are free, we can neglect bound states of the potential. The incoming neutron wavefunction of the state $|\boldsymbol{k}\rangle$, with wavevector $\mathbf{k}$, can be described by a complex plane wave $\Psi_i(\mathbf{r}) = e^{i(\mathbf{k}_i \cdot \mathbf{r})}$. This follows from the time-independent version of equation 2.5 with the normalization factor excluded since the differential cross-section depends only on the ratio of the scattered wave amplitude to that of the in-going wave. When the interaction potential is adiabatically switched on, the scattered state, $\Psi_{\mathbf{k}}$, can be constructed as an integral equation using the retarded Green function, G, and transition operator, T, as

$$\Psi_{\boldsymbol{k}}(\boldsymbol{r}) = (1 + GT)\,|\boldsymbol{k}\rangle. \tag{2.40}$$

Note, the transition operator determines the transition rate from the incoming plane wave state to the scattered state. Here, the free particle energy dependent outgoing Green's function, G, is given by

$$G = (E + i\varepsilon - H_0)^{-1}\,, \tag{2.41}$$

where H_0 represents the neutron free-particle Hamiltonian satisfying

$$H_0|\phi\rangle = E|\phi\rangle. \tag{2.42}$$

Here, $|\phi\rangle$ is the zero mode eigenket of H_0 with the energy eigenvalue E. Since H_0 has a continuous spectrum that will include E, we can express E as a complexified energy $E + i\varepsilon$. The exact purpose of this "$i\varepsilon$" prescription becomes apparent when solving the Green's function in momentum space using an integral representation over k'. In doing so, a singularity is present when $k'^2 = k^2$. Performing contour integration and taking the limit as $\varepsilon \to 0$ shifts the poles slightly off of the real k' axis, distorting the contour to a semicircle on which the wavefunctions vanish. As a result, the integral is given as a sum of the residues at the various poles.

We recognize equation 2.40 as a Lippmann-Schwinger equation which has a unique solution satisfying the given boundary conditions of the incident plane wave wavevector, $\mathbf{k}$, and purely outgoing scattered waves. Expressing 2.41 in the coordinate representation and taking the limit as $\varepsilon \to 0^+$, we get

$$\langle \boldsymbol{r}|G|\boldsymbol{r}'\rangle = -\frac{m}{2\pi\hbar^2}\frac{e^{ik|\boldsymbol{r}-\boldsymbol{r}'|}}{|\boldsymbol{r}-\boldsymbol{r}'|}. \tag{2.43}$$

This equation represents an outgoing spherical wave of the form $G(\mathbf{r}) = \frac{e^{i\mathbf{kr}}}{\mathbf{r}}$; incoming spherical waves, identical to equation 2.43, with an opposite sign in their exponent are produced in the limit as $\varepsilon \to 0^-$. Expressing the scattered wave, $\Psi_{\mathbf{k}}$, in the coordinate representation yields

$$\Psi_{\boldsymbol{k}}(\boldsymbol{r}) = \psi_{\boldsymbol{k}}(\boldsymbol{r}) + \int d\boldsymbol{r}' \langle \boldsymbol{r}|G|\boldsymbol{r}'\rangle \langle \boldsymbol{r}'|T|\boldsymbol{k}\rangle. \tag{2.44}$$

This represents a coherent superposition of the incident plane wave $\psi_{\boldsymbol{k}}(\boldsymbol{r})$ and a spherical scattered wave $\langle \boldsymbol{r}|G|\boldsymbol{r}'\rangle$ from every point $\boldsymbol{r}'$ where $\langle \boldsymbol{r}'|T|\boldsymbol{k}\rangle \neq 0$. In small angle neutron scattering geometries where the neutron detector position is much larger than the range of the potential (i.e., in the limit as $r \to \infty$), we can take the asymptotic behavior of $\Psi_{\boldsymbol{k}}(\boldsymbol{r})$ for $\boldsymbol{r} \gg \boldsymbol{r}'$, reducing the scattered waves, $\langle \boldsymbol{r}|G|\boldsymbol{r}'\rangle$, to a single spherical scattered wave. This transforms the above equation to

$$\Psi_{\boldsymbol{k}}(\boldsymbol{r}) = \{e^{i\boldsymbol{k}\cdot\boldsymbol{r}} + f(\theta)\frac{e^{ikr}}{r}\}, \tag{2.45}$$

which describes the potential as a source of perturbation to the incident plane wave. Therefore, the scattered state is the sum of an incident plane wave and outgoing spherical wave, yielding asymptotic and stationary solutions to the Schrödinger equation. The quantity $f(\theta)$ gives the amplitude of the scattered wave relative to the incident wave and is defined according to

$$f(\theta) = -\frac{4\pi^2 m}{\hbar^2}\langle \boldsymbol{k}'|T|\boldsymbol{k}\rangle. \tag{2.46}$$

Thus, the challenge of solving the Schrödinger equation for the scattered state, reduces to finding the transition operator, T.

Following from the Lippmann-Schwinger equation 2.40, the transition operator is defined as

$$T = V\left(1 - GV\right)^{-1}. \tag{2.47}$$

T must then satisfy the equation $T = V + TGV$, the iterated solution of which gives the Born series,

$$T = V + VGV + VGVGV + ... \tag{2.48}$$

The physical origin of equation 2.48 arises from the fact that the scattered spherical waves become sources of scattering in their own right. Therefore, the neutron-matter interaction produces an infinite series of scattering processes and can be expressed as a von Neumann series of the form

$$T = V\left(1 + \sum_n (GV)^n\right). \tag{2.49}$$

This can be viewed as a multiple scattering expansion, where the first term represents the contribution from single scattering. Unlike nuclear interactions, the magnetic interaction is a weak long-range interaction which may be treated by retaining only the first time in the expansion, such that $T = V$ and $b = -\frac{m}{2\pi\hbar^2}V$, which follows from equation 2.10. In this case, the scattering process is so weak that terms with non-zero angular momentum can be neglected, resulting in a scattered wave which has spherical symmetry with respect to the scattering centre. This is known as the s-wave or Born approximation and is valid for thermal/cold neutron scattering processes, excluding neutron reflectivity. The solution for the scattered wave therefore reduces to the problem of calculating the transition matrix element of the interaction potential. Operating in the Born approximation and using the relations for the scattering wavevector given by $\mathbf{Q} = \mathbf{k}' - \mathbf{k}$, equation 2.46 can be expressed as

$$f(\theta) = \frac{-m}{2\pi\hbar^2} \int d^3\mathbf{r}'\, e^{i\mathbf{Q}\cdot\mathbf{r}'}\, V(\mathbf{r}'). \tag{2.50}$$

Therefore, the scattering amplitude is simply the Fourier transform of the interaction potential, $V(\mathbf{r}')$. Looking at equations 2.10 and 2.50, we see that $f(\theta) = -b$.

The incoming neutron flux may be expressed as $\Phi_{in} = |\Psi_{in}|^2 v = |A|^2 v$, where v is the neutron velocity and A is the amplitude of the function. Similarly, the scattered flux at a distance, r, from the scattering nucleus can be written as $\Phi_{out} = |\Psi_{out}|^2 v = \frac{|A|^2 v b^2}{r^2}$. The total cross-section can therefore be defined as the total flux passing through a sphere of radius, R, around the nucleus, divided by the incoming flux

$$\sigma_s = \frac{|\Psi_{out}|^2\, v\, 4\, \pi\, R^2}{|\Psi_{in}|^2 v}. \tag{2.51}$$

This yields the following expressions for the differential scattered cross-section and scattered cross-section:

$$\begin{aligned} \frac{d\sigma}{d\Omega} &= |f(\theta)|^2 = |b|^2, \\ \sigma_s &= \int_{4\pi} |f(\theta)|^2 d\Omega = 4\pi|b|^2, \end{aligned} \tag{2.52}$$

where $b = b_0 + b' + ib''$ is the scattering length which is a sum of the length associated with the potential scattering (b_0), and the real (b') and imaginary (ib'') parts of the resonance scattering [199]. Alternatively, using equations 2.10 and 2.50 we may define the scattering amplitude as

$$A(\boldsymbol{q}) \propto \sum_j f(\boldsymbol{q}) e^{2\pi i \boldsymbol{q}\cdot\boldsymbol{r}_j} \tag{2.53}$$

and express the differential scattered cross-section as

$$\frac{d\sigma}{d\Omega} = |\sum_j -b_j e^{i\boldsymbol{Q}\boldsymbol{r}_j}|^2, \tag{2.54}$$

given the atomic scattering length, b_j, from an individual nucleus, j. Note, equation 2.54 is proportional to the scattered intensity, $I(\mathbf{Q})$.

2.1.4 Magnetic Neutron Scattering

The magnetic interaction potential between a neutron in a spin state $\boldsymbol{\sigma}$, and a moving electron of momentum, $\boldsymbol{p}$, charge $-e$, and spin $\boldsymbol{s}$ can be described by equation 2.16. The magnetic flux density, $\boldsymbol{B}$, may be separated into two contributions: the first is due to the interaction of the neutron with the spin magnetic moment of the electrons, $\boldsymbol{B}_s$, and the second is due to the interaction of the neutron magnetic field with the electric current produced by the electron's orbital motion, $\boldsymbol{B}_l$. The magnetic dipole moment for a neutron at position $\boldsymbol{r}_n$ gives rise to a vector potential at the position of an electron, $\boldsymbol{r}_e$, according to

$$\boldsymbol{A}_n(\boldsymbol{r}_e, \boldsymbol{r}_n) = \boldsymbol{\mu}_N \times \frac{\boldsymbol{r}}{r^3}, \tag{2.55}$$

where $\boldsymbol{r} = \boldsymbol{r}_e - \boldsymbol{r}_n$ and $r = |\boldsymbol{r}|$. The magnetic interaction Hamiltonian from equation 2.16 between a neutron and a single electron, neglecting diamagnetic terms of second order in μ_N, becomes

$$\begin{aligned} \mathcal{H}_{int}(\boldsymbol{r}_e, \boldsymbol{r}_n) &= \frac{1}{2m}\left(\boldsymbol{p} + \frac{e}{c}\left(\boldsymbol{A}_e + \boldsymbol{A}_n\right)\right)^2 - \frac{1}{2m}\left(\boldsymbol{p} + \frac{e}{c}\boldsymbol{A}_e\right)^2 + 2\mu_B \boldsymbol{s}\cdot\boldsymbol{B}_n \\ &= 2\mu_B\left(\frac{1}{\hbar}\boldsymbol{A}_n\cdot\boldsymbol{p}' + \boldsymbol{s}\cdot(\nabla\times\boldsymbol{A}_n)\right), \end{aligned} \tag{2.56}$$

where $\boldsymbol{A}_e$ denotes the additional contribution to the total vector potential from the surrounding electrons, or an external magnetic field. If $\boldsymbol{A}_e$ is nonzero, then $\boldsymbol{p}'$ becomes $\boldsymbol{p}+\frac{e}{c}\boldsymbol{A}_e$. From equation 2.56 we see that the interaction potential is given by

$$\boldsymbol{V}(\boldsymbol{r}) = -\gamma\mu_N 2\mu_B \boldsymbol{\sigma}\cdot\left[\nabla\times\left(\frac{\boldsymbol{s}\times\boldsymbol{r}}{r^2}\right) + \frac{1}{\hbar}\frac{\boldsymbol{p}\times\boldsymbol{r}}{r^2}\right], \tag{2.57}$$

which consists of the following spin and orbital contributions to the magnetic flux density:

$$\boldsymbol{B}_s(\boldsymbol{r}) = -2\mu_B\frac{\mu_0}{4\pi}\,\nabla\times\left(\frac{\boldsymbol{\sigma}\times\boldsymbol{r}}{r^3},\right) \tag{2.58}$$

$$\boldsymbol{B}_l(\boldsymbol{r}) = -2\mu_B \frac{\mu_0}{4\pi} \frac{1}{\hbar} \frac{\boldsymbol{p} \times \boldsymbol{r}}{r^3}. \tag{2.59}$$

In order to calculate the magnetic scattering cross-section from a material which contains many unpaired electrons, we must calculate the transition matrix element of the interaction potential given by,

$$\langle \boldsymbol{k}_1 \sigma_1 \lambda_1 \left| V \right| \boldsymbol{k}_0 \sigma_0 \lambda_0 \rangle. \tag{2.60}$$

The first matrix element $\langle \boldsymbol{k}_1 \left| V \right| \boldsymbol{k} \rangle$ for a sample containing many unpaired electrons is given by the sum

$$\sum_i \langle \boldsymbol{k}_1 \left| V \right| \boldsymbol{k}_0 \rangle = 4\pi \gamma \mu_N 2\mu_B \boldsymbol{\sigma} \cdot \boldsymbol{M}_\perp (\boldsymbol{k}_1 - \boldsymbol{k}_0), \tag{2.61}$$

where $\boldsymbol{M}_\perp$ is the magnetic interaction operator given by

$$\boldsymbol{M}_\perp = \sum_i \{ \hat{\boldsymbol{Q}} \times \left(\boldsymbol{s}_i \times \hat{\boldsymbol{Q}} \right) + \frac{i}{\hbar Q} \left(\boldsymbol{p}_i \times \hat{\boldsymbol{Q}} \right) \} e^{i \boldsymbol{Q} \cdot \boldsymbol{r}_i}. \tag{2.62}$$

This operator can be expressed in terms of its spin and orbital components as

$$\boldsymbol{M}_\perp = \boldsymbol{M}_{\perp S} + \boldsymbol{M}_{\perp L} = \hat{\boldsymbol{Q}} \times \left(\boldsymbol{M} \times \hat{\boldsymbol{Q}} \right), \tag{2.63}$$

where

$$\boldsymbol{M} = \boldsymbol{M}_S + \boldsymbol{M}_L = -\frac{1}{2\mu_B} \boldsymbol{M}(\boldsymbol{Q}). \tag{2.64}$$

This operator $\boldsymbol{M}$ represents the Fourier transform of the real-space magnetization, $\boldsymbol{M}(\boldsymbol{r})$, given by

$$\boldsymbol{M}(\boldsymbol{Q}) = \int \boldsymbol{M}(\boldsymbol{r}) e^{i \boldsymbol{Q} \cdot \boldsymbol{r}} d\boldsymbol{r} \tag{2.65}$$

and $\boldsymbol{M}_\perp$ is the projection of $\boldsymbol{M}(\boldsymbol{Q})$ onto the plane perpendicular to $\hat{\boldsymbol{Q}}$, given by

$$\boldsymbol{M}_\perp = \boldsymbol{M} - \left(\boldsymbol{M} \cdot \hat{\boldsymbol{Q}} \right) \hat{\boldsymbol{Q}}. \tag{2.66}$$

This equation corresponds to the magnetic selection rule and shows that magnetic scattering is only sensitive to components of the magnetization that lie perpendicular to the direction of the momentum transfer, $\boldsymbol{Q}$. For elastic scattering, the magnetic cross section is therefore given by

$$\frac{d\sigma}{d\Omega} = \left(\frac{\gamma r_0^2}{2\mu_B} \right)^2 \left| \langle \boldsymbol{M}_\perp (\boldsymbol{Q}) \rangle \right|^2. \tag{2.67}$$

Equation 2.67 illustrates the relationship between the the Fourier transform of the sample magnetization to the scattered intensity, while highlighting the magnetic configurations that can be accessed from different geometries. For example, on page 10 we noted that the triangular lattice skyrmion pattern manifests as a hexagon in SANS when probed with the incident neutron wavevector normal to the lattice plane. Conversely, the conical spin phase with the wavevector parallel to the magnetic field and incident neutron wavevector generates no pattern on this plane. Therefore, conical and other chiral magnetic states whose propagation wavevectors lie parallel to the incident neutron wavevector, must be probed from perpendicular geometries.

2.2 Magnetometry

Superconducting Quantum Interference Device (SQUID) magnetometry is an extremely sensitive and invaluable characterization technique that enables the determination of a samples bulk magnetic magnetic properties, given the direct measurement of its magnetic flux [209]. Since SQUIDs rely on the measurement of magnetic flux, they are capable of measuring any physical quantity that can be converted into a magnetic flux, such as magnetic fields, magnetic field gradients, current, voltage, displacement, and magnetic susceptibility, making it a versatile interdisciplinary technique spanning the detection of tiny magnetic signals from the brain/heart in biomagnetism, to the search for axions in cosmology [210, 211]. In general, the device consists of 3 main components, the pick-up circuit, the SQUID volume, and the feedback electronics [212]. At the heart of the SQUID is a superconducting loop interrupted by either one or two Josephson junctions for the RF or dc SQUID, respectively [210]. In the works presented here, measurements were performed on a a Quantum Design MPMS 5 RF SQUID. From here on, we will therefore limit our discussions of SQUID's to those of RF types. For a single-junction loop driven by an AC current, the current-voltage curve exhibits discrete steps whose separation is given by integer multiple of $f\phi_0$, where f is the frequency of the AC current. In an RF SQUID, the loop is inductively coupled to the inductor of an LC-resonant circuit via a mutual inductance M, and is driven by an RF current spanning tens of megahertz to several gigahertz [210], producing an RF voltage which is periodic in the flux applied to the SQUID. Since the amplitude of the oscillating voltage across the resonant circuit is periodic in the applied flux, with a period of one flux quantum, $\Phi_0 = \frac{h}{2e}$ [213], its detection capabilities are on the order of $\approx 10^{-5}\Phi_0$ [213, 210].

Measurement of a samples magnetic properties is accomplished via the inductive coupling of the loop to a local external magnetic field, combining the physical phenomena of flux quantization and Josephson tunneling [210] to produce an output voltage that is periodic in the applied magnetic flux. In direct current (DC) operation mode, the sample is magnetized by a superconducting magnet and is moved through the pick-up coils, inducing a change of a magnetic flux threading the loop, which is converted to a voltage [214]. These detection coils constitute a second-order gradiometer shown in Fig. 2.3, thereby eliminating noise effects due to spatially homogeneous fields and fields that vary linearly with distance [213]. This output voltage corresponds to the voltage required to keep the SQUID flux-locked at the desired working point as a function of distance. From here, the magnetic moment of the sample is given in emu from comparison to carefully calibrated voltage curves for a known magnetic sample, yielding a DC magnetization curve $M(H)$.

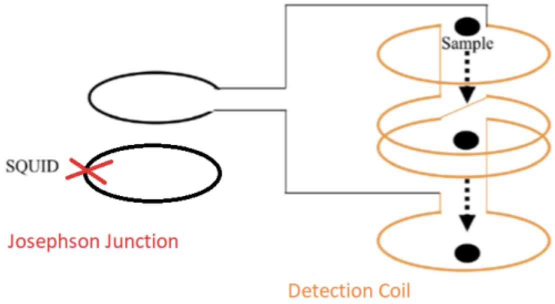

Figure 2.3: Illustration of a DC SQUID measurement for an RF SQUID showing the sample movement through the detection coil (orange), the SQUID (black), and the single Josephson junction (red X). Adapted from [215].

.

While DC measurements employ static fields to measure a constant magnetic moment, AC measurements may be performed to measure the AC magnetic moment, providing information on the magnetization dynamics of the sample. In AC measurement mode, the sample is held in the center of the detection coil and a small AC drive magnetic field is superimposed on the DC field, producing a time-dependent moment in the sample without sample motion. For small drive frequencies, in the measurement regime most closely resembling that of DC measurements, the moment of the sample follows the M(H) curve that would be measured in a DC experiment. For a small AC field with an amplitude of H_{AC} and driving frequency ω,the induced AC moment is given by

$$M_{AC} = \left(\frac{dM}{dH}\right) \cdot H_{AC} sin\left(\omega t\right). \tag{2.68}$$

The amplitude of the observed M_{AC} signal, or equivalently the slope of the $M(H)$ curve, is given by a quantity known as the magnetic susceptibility, defined as $\chi = dM/dH$. The sensitivity of this term to differential changes in M is responsible for the unparalleled sensitivity of this technique, detecting small magnetic shifts even when the absolute moment is large. At higher drive frequencies, the magnetization of the sample may lag behind the drive field, yielding a phase shift ϕ, relative to the drive signal. The susceptibility can therefore be separated into a real in-phase component, χ', and an imaginary out-of-phase component, χ'' given by

$$\begin{aligned} \chi' &= \chi \cos(\phi) \\ \chi'' &= \chi \sin(\phi), \end{aligned} \tag{2.69}$$

where χ is given by $\sqrt{\chi'^2 + \chi''^2}$ and $\phi = \arctan(\chi''/\chi')$. In the low frequency limit, similar to DC measurements, the real component is equivalent to the susceptibility; the imaginary component indicates dissipative dynamic processes such as relaxation and irreversibility in spin-glasses, domain wall motion in ferromagnets, and phase transitions and their dynamics across a wide variety of samples and magnetic states from skyrmions [216, 101] to superconductors [217, 218, 219].

2.3 X-ray Diffraction

X-ray diffraction serves as a valuable technique which provides complementary information to neutron diffraction. X-rays interact with matter primarily through electromagnetic interactions with the electron cloud of atoms, yielding information on electron distributions inaccessible by neutrons. This also leads to a predictable scattering cross section for elements, proportional to their electron density, enabling a different contrast between elements. As a result, combining neutron and X-ray scattering techniques leads to a more detailed interpretation of the scattering patterns as compared to a single-contrast experiment.

X-ray diffraction experiments in particular, enable the determination of fundamental parameters of a crystalline sample, such as the positions, arrangements, and size of the constituent crystals. In monochromatic single crystal diffraction under the von Laue formalism, incident X-rays with wavevectors $\boldsymbol{k}$, will undergo diffraction if the following condition is met:

$$e^{2\pi i(\boldsymbol{k}-\boldsymbol{k}')\cdot\boldsymbol{R}} = 1, \tag{2.70}$$

where $\boldsymbol{R}$ represents the set of Bravais lattice vectors [220] which satisfy $\boldsymbol{R}\cdot(\boldsymbol{k}-\boldsymbol{k}') = 2\pi m$ for integral m. An equivalent formulation derives from Bragg's Law where constructive interference occurs when the path difference between two X-rays specularly reflected from an incident angle θ via successive parallel planes of ions spaced a distance d apart, must equal an integral number of wavelengths λ for their constructive interference,

$$n\lambda = 2d\sin(\theta). \tag{2.71}$$

The equivalence of these two criteria for the constructive interference of X-rays can be seen by considering the Laue condition for constructive interference, where the change in wavevector $\boldsymbol{K} = \boldsymbol{k} - \boldsymbol{k}'$ must be a vector of the reciprocal lattice. This condition can be reformulated entirely in terms of the incident wavevector $\boldsymbol{k}$ as $\boldsymbol{k}\cdot\hat{\boldsymbol{K}} = \frac{1}{2}K$, which states that an incident wavevector $\boldsymbol{k}$ will satisfy Laue's condition if the tip of the vector lies in a plane corresponding to the perpendicular bisector of a line joining the origin of k-space to a reciprocal lattice point $\boldsymbol{K}$. From here, it is apparent that the origin of the diffraction peaks in both the Laue and Bragg formalism's arises from parallel planes, namely from the k-space Bragg planes in the Laue case, and a family of direct lattice planes in the Bragg case [220]. Since the Laue condition assumes elastic scattering, it follows that the incident and scattered wavevectors make the same angle θ with the plane perpendicular to $\boldsymbol{K}$. Therefore, a unified approach describes the scattering as a Bragg reflection, with Bragg angle θ, from a family of direct lattice planes perpendicular to the reciprocal lattice vector $\boldsymbol{K}$.

As shown in section 2.1.3, the scattering amplitude is described by equation 2.53, with the exception that now the scattering factor for each atom, f_j, arises due to interactions with the electron cloud, depending strongly on atomic number. The intensity of the Bragg peaks is given by the square of the scattering amplitude, $|A(\boldsymbol{q})|^2$, yielding equation 2.54.

2.3.1 Powder X-ray Diffraction

Powder X-ray Diffraction (PRXD) is a principal characterization technique used in the phase identification and structural characterization of crystalline materials. Its operational principles rely on the Bragg diffraction of incident X-rays from crystallographic planes, denoted by three Miller indices (h, k, l) upon variation of the angle of incidence θ. In the Ewald sphere construction which is fixed in k-space, as the sample is rotated the reciprocal lattice rotates causing each reciprocal lattice point to traverse a circle about the axis of rotation of the sample. As a result, Bragg diffraction occurs whenever this circle intersects the Ewald sphere [220]. For a single crystal sample, these scattering intensities produce distinct Bragg peaks as a function of scattering angle. For a powdered sample which consists of randomly oriented grains, the incident direction is isotropically averaged, wherein the axis of rotation is varied over all possible orientations, thereby yielding diffraction cones. The diffraction pattern of such a sample can be viewed as the summation of the diffraction patterns from all possible orientations of a single crystal. The diffraction spots of a single crystal therefore transform into concentric rings in the limit of random orientational disorder. However, given the one-dimensional nature of PXRD where scattering intensity is measured as a function of scattering angle 2θ, symmetry-equivalent reflections are summed yielding a multiplicity effect. For example, given the $\langle 100\rangle$ family of planes in a cubic crystal system, the scattered peak will arise from the superimposition of diffraction spots belonging to the $(100),(010),(001),(\bar{1}00),(0,\bar{1},0),(0,0,\bar{1})$ planes. Therefore each peak in a PXRD pattern serves as a measure of the d-spacing that represents a family of lattice planes, providing critical information on the crystal structure and phase purity, including lattice parameters, crystallite sizes, and atom positions/occupancies.

The reduction of the three-dimensional reciprocal space data onto one-dimensional 2θ data sets leads to a drastic loss of information, resulting from accidental and systematic peak overlap [221]. From this it is typically not possible to make a full structure solution determination. However, using a model for a calculated PXRD, the crystal structure may be refined in a process known as a Rietveld refinement. This process implements the least-squares method, minimizing the weighted residuals between the calculated pattern and experimental data. The model is described by a set of parameters which includes contributions from the background, lattice parameters, atomic positions, strain, microstructure, and instrumental factors, amongst others [222, 221].

PXRD measurements presented here were performed at McMaster University for a monochromatic X-ray beam with filtered Cu $K_{\alpha 1}$ radiation of wavelength 1.541 Å. Polycrystalline samples used in measurements were ground into fine powders in order to both reduce nonsystematic inaccuracies from large crystallites and peak broadening due to finite size effects from small crystallites [222]. The powdered samples were unformly distributed on a rotating disk which was placed at the joint of the goniometer. The sample rotation serves to enhance the orientational randomness of the crystallites, eliminating any preferred orientation and texturing effects which would otherwise bias the measurement. The Rietveld refinement was performed using Fullprof [223].

2.3.2 Laue Diffraction

Contrary to Powder X-ray Diffraction in which the sample is rotated to successively satisfy conditions for Bragg Diffraction from different crystallographic planes, the Laue method involves the variation of wavelength to achieve Bragg diffraction from different crystallographic planes. In Laue diffraction experiments, a stationary sample with a fixed orientation (θ) and incident direction $\boldsymbol{n}$, is illuminated by a beam of polychromatic X-rays, thereby satisfying Bragg's condition for multiple reciprocal lattice vectors simultaneously. In the Ewald sphere construction, the Bragg peaks correspond to reciprocal lattice vectors which lie within the region contained between two spheres determined by $\boldsymbol{k}_0 = \frac{2\pi\boldsymbol{n}}{\lambda_0}$ and $\boldsymbol{k}_1 = \frac{2\pi\boldsymbol{n}}{\lambda_1}$. This method is therefore best suited for determining the orientation of crystals in a sample whose structure is known, since the diffraction pattern reflects the symmetry of the symmetry axis of the crystal [220]. In polycrystalline samples, this method can also be applied to get estimates of sample mosaicity through the systematic scanning of a samples surface based on the misorientation of smeared or split Laue patterns from different crystallites. However, due to the limited penetration depth of X-rays, neutron pole figures are best suited for this application.

Laue diffraction measurements presented here were performed in the backscatter geometry. Systematic scanning and slicing of the crystal was performed to analyze the samples crystallinity and align the sample to one of the dominant grains.

Chapter 3

Characterization of the Disordered $Co_8Zn_8Mn_4$ Skyrmion Material

The study presented in this chapter is adapted from [224].

As discussed in section 1.4, the Co-Zn-Mn alloys play host to a rich variety of magnetic and topological phases which have been characterized over a wide range of techniques [75, 116, 131, 115, 140, 56], including the triangular lattice thermal equilibrium phase of $Co_8Zn_8Mn_4$ [75]. The tuning of the Mn-doping for the compositional series introduces both magnetic frustration and magnetic disorder due to antiferromagnetically coupled Mn spin correlations [116, 140, 137] and site mixing of the ferromagnetic Co and antiferromagnetic Mn spins [137, 116], respectively. Magnetic anisotropy has also been shown to vary both in magnitude and orientation of its easy axes upon variation of the Co/Mn ratio [115]. It is precisely this cooperative interplay of magnetic anisotropy, spin disorder, and frustration which stabilizes such a rich energy landscape with a high density of defects in these materials. Accordingly, a myriad of exotic long-period chiral structures/phases have since been realized in the Co-Zn-Mn series, ranging from meron-antimeron lattices generated by in-plane magnetic anisotropy [56], to disconnected low-temperature disordered skyrmion phases stabilized by frustrated interactions [140]. However, previous studies have been constrained to single-crystalline samples and magnetically ordered skyrmion phases, disregarding the influence of disorder in skyrmion stabilization. In this chapter, we report the synthesis procedure and characterization of a polycrystalline $Co_8Zn_8Mn_4$ disordered bulk sample. We employ powder X-ray diffraction, and backscatter Laue diffraction as characterization tools of the crystallinity of the samples, while magnetic susceptibility and SANS measurements are performed to study the skyrmion phase. Magnetic susceptibility measurements show a dip anomaly in the magnetization curves, which persists over a range of approximately 305 K – 315 K. SANS measurements reveal a rotationally disordered polydomain skyrmion lattice. Applying a symmetry-breaking magnetic field sequence, we were able to orient and order the previously jammed state to yield the prototypical hexagonal diffraction patterns, with secondary diffraction rings. This emergence of skyrmion order serves as a unique demonstration of the fundamental interplay of structural disorder, and anisotropy, in stabilizing the thermal equilibrium phase, reinforcing the rich energy landscapes inherent to these materials.

3.1 Synthesis

The material was synthesized via the solid state reaction $8\mathrm{Co} + 8\mathrm{Zn} + 4\mathrm{Mn} \rightarrow \mathrm{Co_8Zn_8Mn_4}$. The powders were mixed in stoichiometric ratios in an agate mortar under an argon atmosphere. Once thoroughly ground, the resulting mixture was pressed into a pellet, which was then sealed in an evacuated quartz tube with a conically shaped end. The conical shape of the ampoule served to facilitate nucleation along a dominant growth direction, imposed by the geometry of the confining tube. The ampoule was inserted into a furnace at 700°C and the temperature was increased to 1025°C over the course of 12 hours. It was then cooled at a rate of 2°C/h until 700°C was reached. Finally, it dwelled at 700°C for 12 hours, and was removed. The final product was a conical shaped silver polycrystal (approximately 2-3 grains) with dimensions 0.8 cm x 1.4 cm (diameter x length) and mass of 2 g as shown in Fig. 3.1.

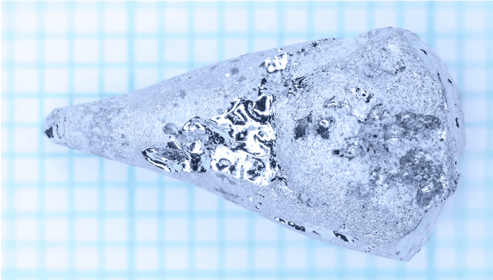

Figure 3.1: Polycrystalline $\mathrm{Co_8Zn_8Mn_4}$ sample mixed under argon of dimensions 0.8 cm x 1.4 cm and mass 2 g. Each grid line corresponds to 1 mm. Reprinted from [224].

The reaction products were analysed via powder X-ray diffraction in the scattering angular (2θ) range of $20° - 110°$ using the Cu $K_{\alpha 1}$ wavelength of 1.54056 Å. A Rietveld refinement of the diffraction data to the $P4_132$ space-group (β-Mn-type) was performed using the FullProf program, from which we were able to extract a lattice constant of 6.37161(1) Å. Fig. 3.2 shows the Rietveld refinement for the powder X-ray diffraction spectra, where the red dots are the measured spectra, the black line is the predicted spectra (where the vertical blue lines below indicate expected peak locations), and the blue line is the difference between the two. The sharpness of present peaks (evidenced by the zero slope of the blue curve), and absence of additional peaks indicate the sample is phase pure.

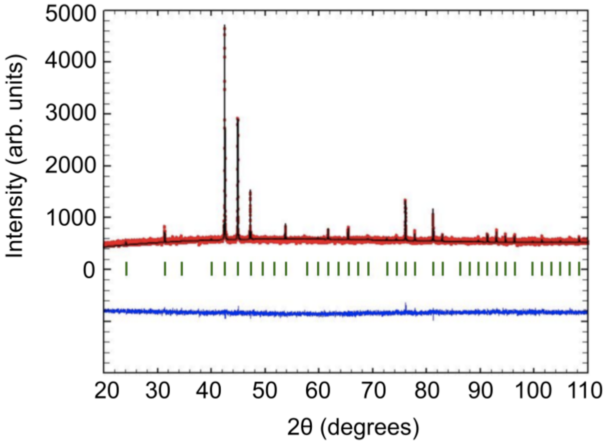

Figure 3.2: Rietveld refinement for powder X-ray diffraction of $Co_8Zn_8Mn_4$. The black curve is the predicted spectra, the red line is the data, and the blue is the difference between the two. The green vertical lines indicate the locations of the expected peaks. The refinement demonstrates the sample is phase pure with space-group β-Mn and lattice constant 6.37161(1) Å. Reprinted from [224].

3.2 Characterization

Backscatter X-ray Laue diffraction was performed as a preliminary investigation of the crystallinity and orientation of the material (Fig. 3.3). Based on a changing diffraction pattern during translation, we were able to identify grain boundaries. Through systematic scanning and slicing, the polycrystal was cut into a rectangular prism of dimensions 3.4 mm x 3.3 mm x 3.0 mm while mapping the crystal orientation of the polycrystalline sample. The final product was polycrystalline with the (100) direction of the dominant grain along

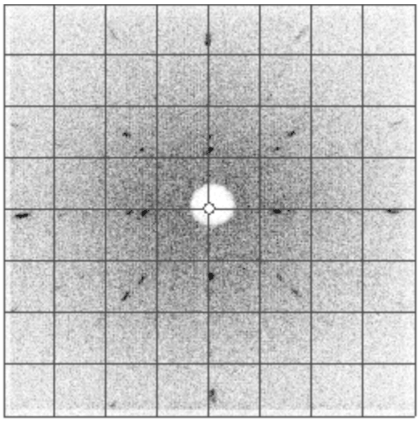

Figure 3.3: Laue image along (100) direction of dominant grain on the front face of the cube. All peaks were indexed to the (100) direction, verifying the single grain portion of this material. The fourfold symmetry of the pattern is characteristic for the (100) direction of a cubic crystal. Reprinted from [224].

one face of the rectangular prism. Fig. 3.3 shows a Laue pattern for the dominant grain, demonstrating the archetypal 4-fold symmetry of the cubic lattice along the (100) direction.

Magnetic susceptibility measurements were performed using a Quantum Design MPMS 5 Superconducting Quantum Interference Device with an AC option installed. The high temperature ferromagnetic phase was verified via FC from 400 K (Fig. 3.4). The onset of the transition was found to be 320 K. A Curie-Weiss fit between 350 K and 400 K results in an effective magnetic moment of 1.6 μ_B. The high temperature vertical offset between the FC and ZFC (zero-field cooled) curves is a result of the disparity in magnetization due to the aligned ferromagnetically ordered domains in the FC case, as opposed to the misaligned domains in the ZFC case which produce a smaller net moment. Further cooling revealed a notable path dependence of the susceptibility on different magnetic field cooling protocols (i.e. ZFC or FC), as is evident by the sharp change in temperature dependence of the ZFC magnetization at around 7 K (illustrated by the arrow in Fig. 3.4). This magnetic behavior is evidence of a spin-glass transition, wherein the marked irreversible magnetic behavior after field cooling is a result of the cooperative freezing of spin-glass [225]. FC measurements bias the energy landscape, whereas for ZFC measurements the existence of many metastable states leads to an irreversible path dependence, as the material may not follow the same path to escape the energy valley. The mechanisms underpinning this transition have been previously reported via crystal structure analysis by neutron powder diffraction in [137], occurring due to site mixing between the Co and Mn atoms on the 8c crystal-

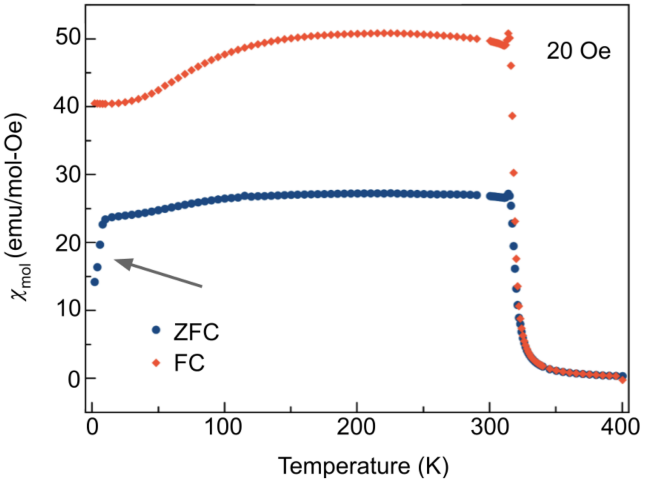

Figure 3.4: Magnetic susceptibility per mol of $Co_8Zn_8Mn_4$ after zero field cooling (ZFC) and field cooling from 400 K in a magnetic field of 20 Oe. The bifurcation behaviour of the ZFC and FC curves at 7 K results from the path-dependent behaviour of the susceptibility (as indicated by the arrow in the ZFC curve), which is indicative of a spin-glass transition. Reprinted from [224].

lographic sites, which gives rise to random competition amongst the ferromagnetic and antiferromagnetic interactions, yielding quenched magnetic disorder. Further susceptibility measurements were carried out to confirm the presence of the skyrmion phase; Fig. 3.5 shows isothermal magnetization measurements as a function of magnetic field for a 20.0 mg polycrystalline piece of the sample. The magnetization measurements were taken while increasing the DC field from 0 Oe to 400 Oe, after which measurements were taken while decreasing the field (not shown). The notable decrease in magnetization for temperatures above 320 K is consistent with exiting an ordered phase into a paramagnetic phase.

We performed differential magnetic susceptibility measurements at 300 K, 305 K, 310 K, and 315 K. This was investigated by taking numerical derivatives of the M vs H curves and, after smoothing the data, show abrupt dips in the susceptibility (with the strongest dip occurring at 310 K contained within the rectangular dotted box in Fig. 3.6), suggestive of a phase transition.

AC susceptibility measurements were performed which depend upon $\frac{dM}{dH}$ but do not involve using a numerical derivative, which can be susceptible to large fluctuations. AC measurements are therefore a much more sensitive technique, yielding a much smaller uncertainty than the above differential magnetic susceptibility measurements. The AC

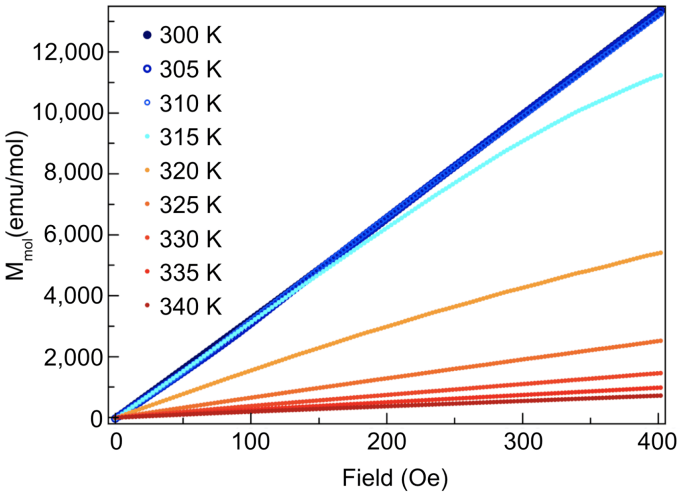

Figure 3.5: Magnetic field dependent magnetization upon increasing magnetic fields from 0 Oe to 400 Oe for a temperature range of 300 K-340 K, in 5 K increments. Low-high temperature corresponds to blue-red curves. Note a substantial decrease in magnetization for temperatures greater then 320 K, consistent with a paramagnetic phase. Reprinted from [224].

susceptibility measurements show similar peaks as a function of applied field, indicating a phase transition. The most pronounced dip structure is again observed at a temperature of 310 K (contained within the magnetic field range defined by the two lines and arrow in Fig. 3.7), consistent with Fig. 3.6. These dip structures are well-known markers of the temperatures and fields over which the skyrmion phase exists [75]. The AC susceptibility shows much cleaner and more defined dip structures than Fig. 3.6. AC measurements also probe the dynamics of the system and may be included in future work to probe the time-scales of the metastable skyrmion phases found below 300 K.

We performed unpolarized SANS at the NG7-30m beamline at the National Institute for Standards and Technology (NIST) for a 15 m beam configuration and a neutron wavelength of 6 Å[226, 227]. At room temperature in zero field, our initial SANS measurements revealed four smeared magnetic satellites atop a circular ring, indicating multi-domain single q-helical structures, with the preferential smearing direction of the peaks elucidating the anisotropy direction (Fig. 3.8a). Upon field-cooling through the ferromagnetic phase, from 420 K to 310 K in a field of 250 Oe, a ring developed. The absence of the signature triangular lattice skyrmion hexagonal pattern is a result of the polycrystalline nature of the material; the misalignment of the skyrmion domains breaks the order in many directions

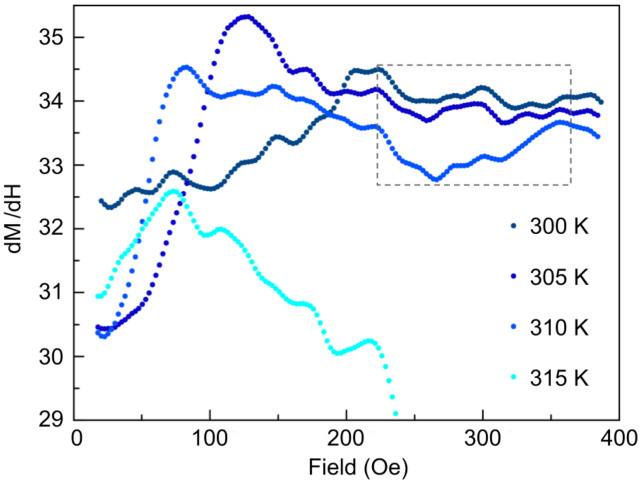

Figure 3.6: Temperature dependent isothermal differential magnetic susceptibility upon increasing magnetic fields from 0 Oe to 400 Oe. Low-high temperature corresponds to dark blue-light blue curves. The dip structure (region contained within the rectangular dotted box) is most clearly pronounced for 310 K, and presents at a field of ∼ 200 Oe, indicating the onset of the skyrmion phase. Reprinted from [224].

thereby smearing the hexagonal patterns, precipitated by each individual domain, to produce a ring. Using a symmetry-breaking magnetic field sequence [112] where the sample is rotated symmetrically in the static magnetic field to precipitate ordered and oriented skyrmion lattices despite the overwhelming structural disorder, the underlying triangular lattice skyrmion phase was revealed. The development of a first order ring with 6 peaks and an additional secondary ring was observed after 10 symmetric rotations. Fig. 3.8c shows the fully discernible 6-fold primary ring after 30 rotations, accompanied by a second-order ring mimicking the same hexagonal symmetry with 12 peaks. The presence of the secondary ring indicates potential multiple scattering and/or higher order diffraction. The underlying mechanism is left to be investigated for future experiments. The energetics of the skyrmion ordering sequence showed, through micromagnetic simulations, magnetic moments to diverge away from the external field when approaching a magnetic hard axis, consequently increasing the DM energy, resulting in a lattice reorientation [112]. Therefore, the response of our material to the ordering sequence highlights the role of anisotropy in skyrmion formation, and reorientation dynamics.

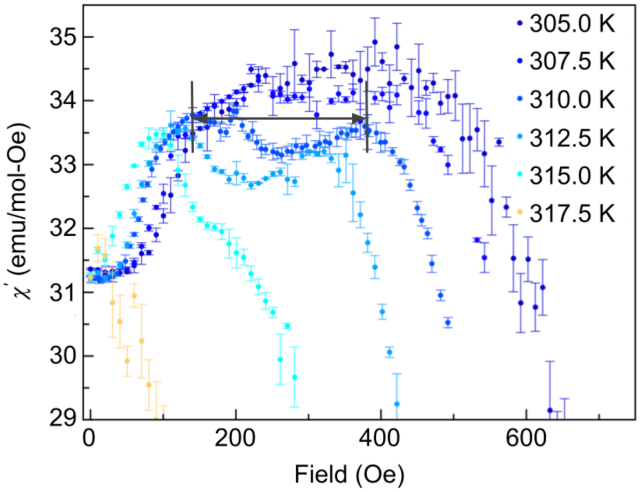

Figure 3.7: Temperature dependence of AC magnetic susceptibility per mol of $Co_8Zn_8Mn_4$ over a range of 305 K-317.5 K after increasing magnetic fields from 0 Oe to 500 Oe in a 100 Hz driving field, with an amplitude of 0.1 Oe. Low-high temperature corresponds to dark blue-lighter colored curves. The skyrmion phase is most pronounced at a temperature of 310 K, and is observed to persist in the dip anomaly between 100 Oe and 450 Oe (contained within the region bounded by the lines, as indicated by the arrow). The field value at the minimum of the dip determines the largest and most robust skyrmion phase; these temperature and field parameters are then used for SANS measurements on the material. Reprinted from [224].

3.3 Conclusions

We have successfully demonstrated the synthesis and characterization of the above room temperature bulk disordered triangular lattice skyrmion material $Co_8Zn_8Mn_4$. Powder X-ray diffraction studies revealed a pure phase, while backscatter Laue diffraction and neutron diffraction indicated a polycrystalline material. SANS measurements demonstrated the underlying rotationally disordered skyrmion domains. Application of the symmetry-breaking rotation sequence [112] precipitated ordered and oriented triangular skyrmion lattices, yielding secondary diffraction rings. These secondary diffraction rings are most likely a combination of double scattering (owing to the thickness of the sample), and higher-order diffraction, in turn elucidating the effectiveness of the technique in [112] for ordering and even promoting the growth of skyrmions, despite the presence of disorder, thereby producing long-range order. While the phenomena of skyrmion ordering is by no

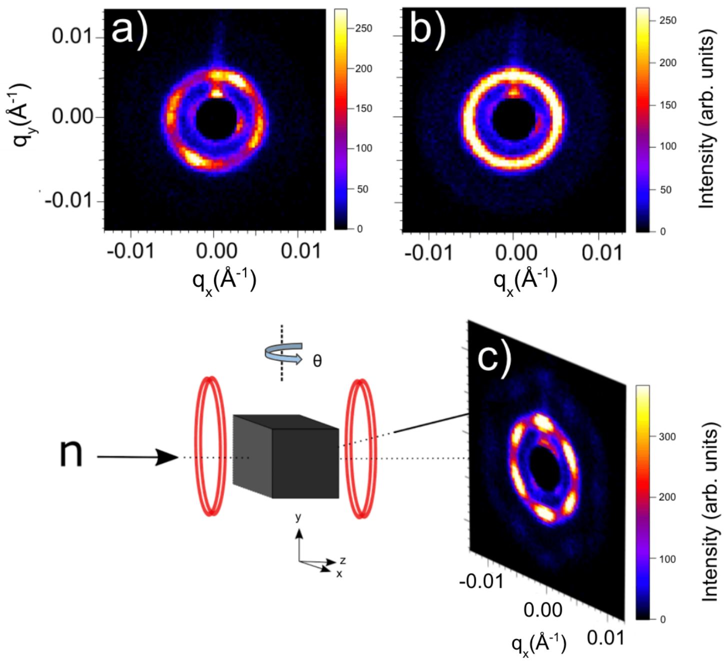

Figure 3.8: SANS images showing disordered helical ground state at room temperature in zero field a), initial scattering ring for disordered skyrmion domains at 310 K in a magnetic field of 250 Oe b), schematic of symmetry-breaking field rotation setup, and SANS image after 30 rotations of the rotation sequence at 310 K in a field of 250 Oe, c). The increased intensity/preferential smearing of the peaks in the top right and bottom left diagonals of the fourfold helical image elucidate the anisotropy direction for the crystal. Schematic of the rotation setup illustrates neutron propagation direction (n) is in the z-direction. For the symmetry-breaking rotation sequence the sample is rotated symmetrically in the xz plane about θ, with the magnetic field fixed in the z-direction. Reprinted from [224].

means novel, experimental demonstrations of the conversion from disordered chiral states to ordered skyrmion lattice forms—in varying host compounds—contributes fundamental insights into the nature of skyrmion formation energetics, pinning phenomena, and stabilization mechanisms. This study serves as a unique demonstration of the interplay of anisotropy and disorder in the thermal equilibrium phase for the Co-Zn-Mn skyrmion series, reinforcing the influence of crystalline disorder and material defects on skyrmion formation and orientations in skyrmion phases stabilized by thermal fluctuations. Future experiments may explore the ratio of multiple scattering to higher-order diffraction through the use of Renninger scans [228]. Furthermore, we intend to use a newly developed reconstruction algorithm [229] to perform 3D tomography of skyrmion topological transitions in the bulk, as well as incorporate spin components to explore the structure of the neutron wavefunction after passing through a skyrmion sample [160, 197, 195].

Chapter 4

Skyrmion Alignment and Pinning Effects in a Disordered Multi-Phase Skyrmion Material $Co_8Zn_8Mn_4$

The study presented in this chapter is adapted from [113].

Underlying disorder in skyrmion materials may both inhibit and facilitate skyrmion reorientations and changes in topology. The identification of these disorder-induced topologically active regimes is critical to realizing robust skyrmion spintronic implementations, yet few studies exist for disordered bulk samples. In this chapter, we employ small angle neutron scattering and micromagnetic simulations to examine the influence of skyrmion order on skyrmion lattice formation, transition, and reorientation dynamics across the phase space of a disordered polycrystalline $Co_8Zn_8Mn_4$ bulk sample. Our measurements reveal a new disordered-to-ordered skyrmion square lattice transition pathway characterized by the novel promotion of four-fold order in SANS and accompanied by a change in topology of the system, reinforced through micromagnetic simulations. Pinning responses are observed to dominate skyrmion dynamics in the metastable triangular lattice phase, enhancing skyrmion stabilization through a remarkable and previously undetected skyrmion memory effect which reproduces previous ordering processes and persists in zero field. These results uncover the cooperative interplay of anisotropy and disorder in skyrmion formation and restructuring dynamics, establishing new tunable pathways for skyrmion manipulation.

4.1 Disordered Skyrmion States

Bulk skyrmion states have been realized over a broad temperature-magnetic field phase space, with stabilization mechanisms ranging from thermal fluctuations just below T_c in thermodynamic equilibrium states [75], to quenching processes via rapid field-cooling (FC) procedures in metastable states [141]. Such metastable skyrmion phases have been shown to exhibit disorder-dependent cooling rates (i.e., dependent on doping, vacancies, etc, present in the system) [99, 141, 122, 101, 116, 59, 118], with a unique hierarchy of interaction terms determining unconventional skyrmion formation and stabilization energetics [230]. One notable example is the anisotropy-stabilized low-temperature skyrmion lattices realized in the bulk cubic helimagnet, Cu_2OSeO_3, through competition between anisotropic exchange and cubic anisotropy [118]. Additionally, studies of disordered skyrmion systems with weak magnetocrystalline anisotropy have demonstrated the precipitation of skyrmion order in triangular lattice phases through sequences which rock the external magnetic field relative to the sample [112]. As such, examining the role of disorder and anisotropy in skyrmion systems [231, 101] serves as an excellent testbed for realizing new pathways and mechanisms which stabilize metastable phases and facilitate structural lattice transitions.

The chemically doped $Co_xZn_yMn_{20-x-y}$ compositional series outlined in section 1.4, presents a unique platform to investigate skyrmion behaviour, owing to its interplay of magnetic anisotropy, site disorder, and frustration, which generates diverse topological phases and lattice forms [116, 99, 56, 75]. Of particular interest are the thermal equilibrium and metastable phases, which host skyrmion lattices of both triangular and square forms. Random site occupancies of Co and Mn atoms on the 8c site, and Co, Zn, and Mn atoms on the 12d site introduces site-disorder which stabilizes a high density of defects [137, 116], enabling quenching to triangular lattice metastable phases with moderate cooling rates [99, 116, 232, 117]. Upon further cooling, the interaction energy hierarchy shifts: magnetocrystalline anisotropy increases [115, 116] and the development of antiferromagnetic correlations of the Mn spins decreases the ratio of the ferromagnetic exchange to DM interaction [232, 116, 137, 117]. Together, these two actions drive a large increase in q, which triggers a triangular-to-square lattice transition, where anisotropy determines the directionality and type of distortion [99, 116, 232, 117].

4.2 Methods

Unpolarized SANS was performed at the NG7-30m beamline at the National Institute for Standards and Technology (NIST) for a 15 m beam configuration and a neutron wavelength of 6 Å(Fig. 4.1a) [226, 227, 233]. The sample used for these measurements was that of a polycrystalline cube of dimensions 3.4 mm x 3.3 mm x 3.0 mm, whose growth and characterization was outlined in chapter 3 [224]. Prior to changing any temperature or field parameters, the ground-state helical phase was verified at room temperature in zero field (Fig. 4.1b). A field-cooling procedure was executed from the ferromagnetic phase to enter the skyrmion envelope (Fig. 4.2), with the magnetic field applied along the neutron flight path (z-direction in Fig. 4.1a), lowered until 250 G, determined from the maximal dip in previous AC susceptibility measurements [224]. Using a skyrmion-ordering sequence [112], the sample was rotated symmetrically in the static magnetic field to precipitate an ordered and oriented skyrmion lattice (Fig. 4.1a).

To examine the influence of underlying disorder on skyrmion lattice transitions, the low-temperature metastable square lattice skyrmion phase (M-S-SkX) was investigated by way of the disordered thermal equilibrium triangular lattice skyrmion phase ((D)E-T-SkX) phase (Fig. 4.11a). The (D)E-T-SkX phase was regained from its ordered counterpart by saturation into the ferromagnetic phase, through the application of a strong magnetic field, and subsequent lowering of the field back into the skyrmion envelope (b.2 of Fig. 4.11). A square phase was then realized at 28 K in a field of 100 G (b.3 of Fig. 4.11).

In a separate SANS experiment, the ordered thermal equilibrium triangular lattice skyrmion phase ((O)E-T-SkX) was brought into the ordered metastable triangular lattice skyrmion phase ((O)M-T-SkX) via FC (c.2 of Fig. 4.11). In the (O)M-T-SkX phase, at a temperature of 173 K, the skyrmion phase was saturated into the ferromagnetic phase by increasing the field to 1 T, from its previous value of 10 G (indicated by the vertical arrow in Fig. 4.2). The field was then lowered back to 10 G (c.3 of Fig. 4.11) in an attempt to regain the phase to examine the nature of the metastability, and any potential memory effects. The ordering sequence was then performed in the resultant phase for two different field values (c.4 and c.5 of Fig. 4.11) in order to investigate the energetics and pinning dynamics of the persisting phase. Finally, the ordered square phase was entered (c.6 of Fig. 4.11) using another FC procedure for comparison with the disordered square phase, to understand the mechanisms of the transition.

4.3 Skyrmion Ordering in the Thermal Equilibrium Phase

The experimental setup for the SANS experiments is shown in Fig. 4.1a. The SANS pattern for the initial helical state was that of four smeared magnetic satellites atop a circular ring, indicative of multi-domain single q-helical structures (Fig. 4.1b) [75, 224]. After FC through the ferromagnetic phase, from 420 K in a field of 250 G, a ring developed at 310 K (Fig. 4.1c). The absence of the signature triangular lattice skyrmion hexagonal pattern is most likely a combination of the chemically disordered and above-room-temperature nature of the phase/material.

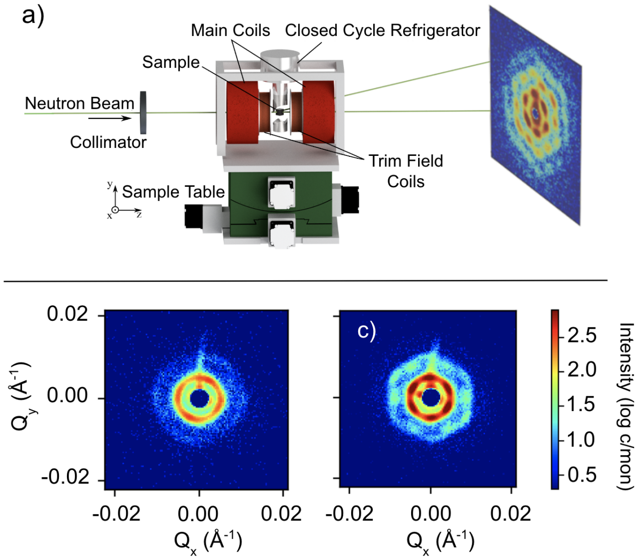

Figure 4.1: Schematic of the experimental SANS setup (a). The neutron propagation direction and magnetic field direction are parallel (along z). For the ordering sequence the sample was rotated symmetrically about the y-axis (in the xz-plane), with the magnetic field held fixed in the z-direction. SANS images for b) disordered helical state at 290 K in 0 G, and c) initially disordered thermal equilibrium phase (D-Skx) at 310 K in 250 G, both exhibiting magnetic scattering at approximately the same q_0 of 0.0052 Å^{-1} (reproduced from [224]). Note that the presence of a flare in both images is caused by scattering off of the samples surface due to a neutron beam size exceeding the sample size. Both images are normalized to a fixed number of standard monitor counts to enable direct comparison between images, with the same scale for the color plots. Note the colorbar is a log-scale of intensity. Adapted and reprinted from [113].

When referring to the levels of disorder in the material, there are two principle length scales we may address: the exchange interaction field (i.e the combination of ferromagnetic exchange (A), DMI (D), and anisotropy from site-to-site), and the periodicity of the spin texture (as determined on average from the ratio of A/D). For this material, the exchange length is approximately 11 nm as defined in [234] using material parameters from [232].

The crystal mosaicity was previously reported in [224] as consisting of approximately 2-3 grains, with the crystal cut such that the (100) direction of the dominant grain is along the front face of the rectangular prism. Systematically scanning and slicing of the material using Backscatter X-ray Laue diffraction provided estimations of sample mosaicity consisting of 2-3 grains, one occupying a majority volume fraction, with low-angle grain boundaries. In order to produce a ring-like scattering image, one would need a large collection of slightly misoriented grains—assuming the grains are composed of idealized skyrmion domains which exhibit perfect triangular packing of the skyrmions (i.e., long transverse correlation lengths) and therefore minimal azimuthal smearing in their diffraction peaks. Each grain would then precipitate a sixfold pattern, with their superposition smearing the individual hexagonal patterns into a ring. In the event that the sample was comprised of a few grains, large-angle grain boundaries would be required to sufficiently rotate the hexagonal scattering patterns enough to smear their collective scattering pattern into a ring. Given the reported crystallinity of the sample, these two cases are unlikely to be responsible for the observed disorder. We will therefore concern ourselves primarily with the two length scales of disorder mentioned earlier, and take note that grain boundaries may act as sources of disorder, interrupting skyrmion long-range ordering in a non-linear manner [235]. While this effect is not quantifiable given only a single polycrystalline sample and the compounding influence of site-disorder, sample polycrystallinity may become more relevant when discussing defect-related pinning in the metastable phase.

Alternatively, the compositional disorder inherent to the unit cell of the $\mathrm{Co}_x\mathrm{Zn}_y\mathrm{Mn}_{20-x-y}$ series of materials may manifest as random local variations in the exchange field, which can serve as nucleating and pinning defect sites, irrespective of the crystallinity of the material. Examples include single crystal samples of doped (Fe, Co)Si, which have been shown to produce disordered chiral jammed states [112]. In particular, the internal chemical disorder and weak magnetocrystalline coupling produces multiple degenerate helical domains, which transform into skyrmion domains with weak relative orientation, upon application of a laboratory field [112]. This leads to orientational disorder of the second length scale, wherein one domain will propagate, becoming trapped upon intersecting another domain and/or defect. This trapping precludes long-range order, precipitating intermediate chiral spin textures due to the domain spacing not satisfying integer skyrmion lattice constant multiples, resulting from randomly distributed nucleating sites [112]. The inability of these structures to propagate or reorient leads to "jammed" configurations, such as chiral or labyrinth domains, amongst skyrmion domains [112]. Therefore, the chemical disorder collectively generates a rich energy landscape exhibiting intermediate chiral and jammed skyrmion states.

Similarly, $\mathrm{Co}_x\mathrm{Zn}_y\mathrm{Mn}_{20-x-y}$ possesses both internal chemical disorder [116, 137] and rel-

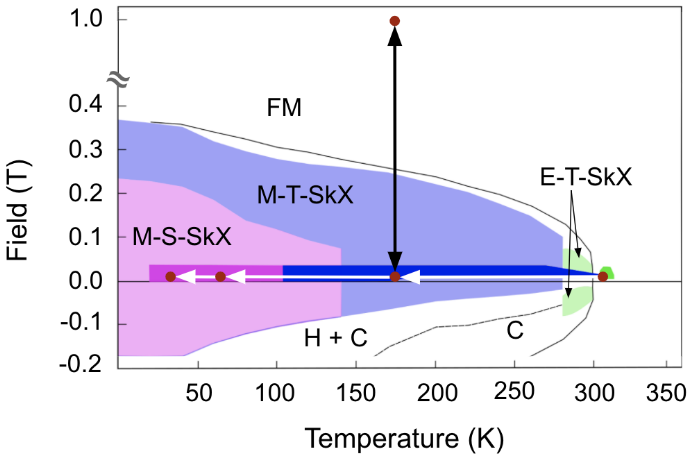

Figure 4.2: Known phase diagram of $Co_8Zn_8Mn_4$ material (lightly shaded regions) compiled from [116], with region of phase space which we have sampled through AC and SANS measurements (both in this paper and in [224]) illustrated by darkly shaded regions. Red dots illustrate measurement points of SANS images in the paper. White and black arrows indicating the field-cooling procedures and memory test performed in the experiments, respectively. Field-cooling procedures were performed over a magnetic field range spanning 50 G to 400 G. Green regions correspond to the thermal equilibrium skyrmion phase (E-T-SkX). Note: for our material, this skyrmion window is shifted up by approximately 10 K as compared to [116]. Purple and pink regions correspond to metastable triangular lattice (M-T-SkX) and square lattice phases (M-S-SkX), respectively. Helical, conical, and ferromagnetic states are indicated by H, C, and FM, respectively. Reprinted from [113].

atively weak magnetocrystalline anisotropy around room temperature [115]. The ring-like scattering pattern displayed in Fig. 4.1c may therefore be attributed to the misalignment and trapping of the skyrmion and chiral domains which breaks the order in many directions. In reciprocal space, this would produce a ring scattering pattern due to the superimposition of rotationally offset hexagonal patterns and other magnetic structures, such as rotationally disordered helical domains, with no net orientation, but the same preferred q. Therefore, the degree of order may be interpreted from the angular width of the diffraction peaks, which we will examine later. Moreover, it is not to be ignored that we are in an above-room-temperature phase; thermal fluctuations which stabilize this phase may also contribute fluctuation-disorder by way of skyrmion merging, splitting, collapse, and nucleation.

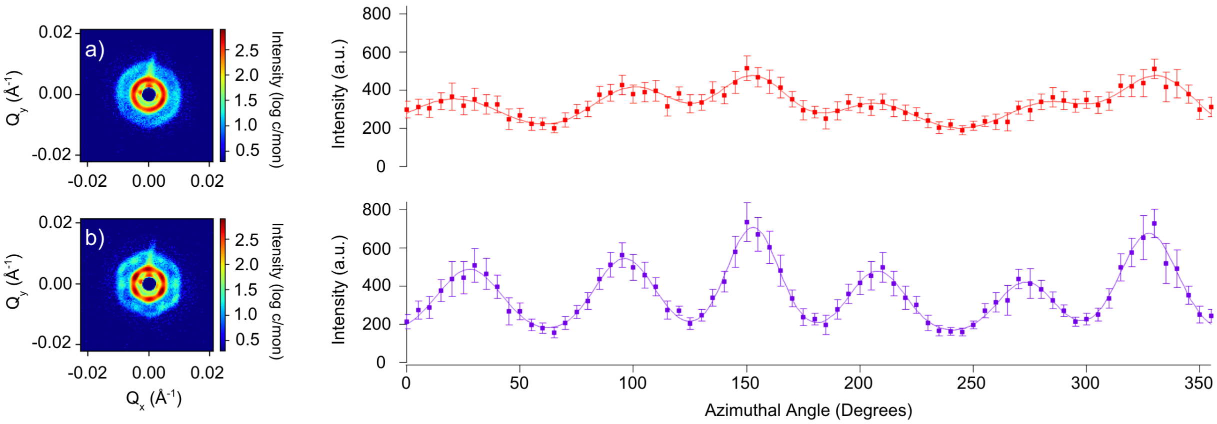

Figure 4.3: SANS measurements as a function of magnetic field skyrmion-ordering sequence. Diffraction patterns and their corresponding annular averages of first-order scattering rings after 10 (a), and 40 (b) rotations of the ordering sequence at 310 K in a magnetic field of 250 Oe. Solid lines are fits of the measurement points to six Gaussian peak functions with a constant baseline intensity. Note the peak heights and widths are drastically altered between a) and b). All images are normalized to a fixed number of standard monitor counts to enable direct comparison between images, with the same scale for the color plots. Note the colorbar is a log-scale of intensity. Reprinted from [113].

The skyrmion-ordering sequence which was used in the SANS experiments entails rotating the sample in the static magnetic field (about the y-axis in Fig. 4.1a), with the rotational range determining the efficacy of the skyrmion ordering response. This technique has been previously demonstrated to disentangle jammed chiral states, thought to reduce defect densities and nucleate additional skyrmion topological charge [112]. This sequence was used in combination with various FC procedures and samplings of the phase space of the material (outlined in Fig. 4.2). Upon application of the ordering sequence in the (D)E-T-SkX phase, the development of a first-order ring with 6 peaks was observed, accommodated by an additional secondary ring mimicking the same hexagonal symmetry with 12 peaks. Fig. 4.3a and b show the developing, and fully discernible 6-fold primary rings after 10 and 40 rotations, respectively. The presence of the secondary ring indicates potential multiple scattering and/or higher order diffraction. Comparing Fig. 4.1c and Fig. 4.3, we observe the conversion of the disordered phase to the ordered triangular lattice phase via the dissolution of the ring diffraction pattern, and promotion of hexagonal peaks. Looking at the azimuthal projection of the primary diffraction rings of Fig. 4.3, we see that this transition manifests as an evolution of six peaks, accompanied by decreasing peak widths and baseline intensity. Note that there is no direct conversion between the decrease in ring intensity and increase in peak intensity, reinforcing the conclusion that the ring is comprised of additional chiral magnetic structures that upon rotation nucleate additional topological charge structures. This action is consistent with disentangling a jammed state of chiral domains, through the collective reorientation of skyrmion domains and formation of new skyrmions via the breakup of labyrinth domains through emergent monopole nucleation and propagation [112, 59]. Therefore, the reported behaviour in Fig. 4.3 occurs as the rotational skyrmion alignment improves, and previously jammed states comprised of mixed helical/labyrinth phases are disentangled, enabling further skyrmion nucleation and propagation, which additionally contributes to the sixfold scattering signal.

4.4 Disordered Metastable Skyrmion Transitions

As we cooled the sample by a FC procedure through the (D)E-T-SkX phase into the disordered metastable triangular phase ((D)M-T-SkX), there was a subtle development of peaks atop the ring diffraction pattern. The promotion of these peaks was observed to alternate with continued cooling, dissolving peaks into the background ring, while enhancing new peaks. The SANS measurement in the disordered square phase (Fig. 4.4) shows a heavily smeared four-fold pattern with significant promotion of the peaks along a preferred orientation of the q-vector. Subsequent re-warming processes into the room-temperature skyrmion phase, in addition to AC susceptibility measurements performed in the square phase, confirmed the presence of skyrmions which contributed to the square pattern. The annular average confirms the presence of four peaks; the variable baseline intensity, height, and width of the peaks suggests preferential development of the square lattice phase along a preferred q-direction. That is to say, the two peaks along the anisotropy direction display decreased baseline intensities and peak widths, and increased scattering intensities compared to the remaining two peaks. This is consistent with recent studies examining cubic anisotropy in the $\mathrm{Co}_x\mathrm{Zn}_y\mathrm{Mn}_{20-x-y}$ skyrmion series, which found that anisotropy controls the angular distribution of the q-vectors, exhibiting a trend with temperature similar to that of the inverse of the full width at half maximum of the SANS peaks [115]. In our case, however, the mere presence of four-fold peaks suggests a more complex action, generating improved rotational alignment in addition to increased development of the skyrmion tubes in the preferred q direction—whether it be through lengthening of existing tubes and/or nucleation of new tubes, contrary to what one would expect. In [115], increased anisotropy enhances orientational order and defines the distribution in rotational alignment of the skyrmions. Alternatively, for the case of disordered skyrmions there is this additional mechanism of skyrmion development, wherein anisotropy may play a greater role by facilitating the disentangling of jammed states to allow reorientations to a square phase. We note that the overall scattering intensity of the square lattice peaks are greatly reduced from the ordered triangular lattice, a fact which may be attributed to disorder somewhat inhibiting skyrmion development and reorientations, resulting in leftover topologically trivial states such as helical, conical, and ferromagnetic domains. Neither conical or ferromagnetic states would contribute to the scattering signal as the ferromagnetic signal is masked in the central peak by the beam block, while conical domains would have to be probed in a perpendicular field geometry.

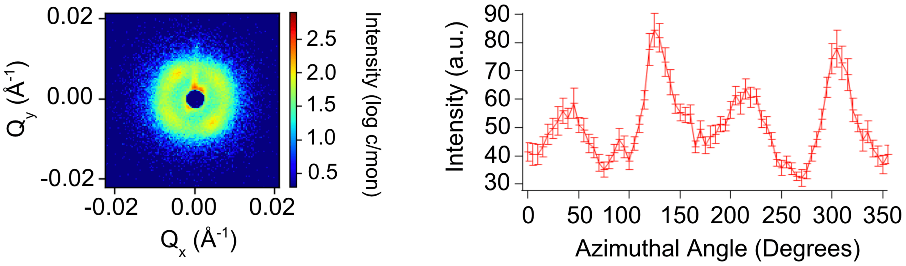

Figure 4.4: SANS image, and its corresponding annular average, for the square lattice skyrmion phase, with significant promotion of the peaks along the anisotropy direction. Solid lines are fits of the measurement points to four Gaussian peak functions with a constant baseline intensity. Measurement was taken at 28 K in a field of 100 G. Note the colorbar is a log-scale of intensity. Reprinted from [113].

A decrease in the A/D ratio is stipulated to accompany the increase in anisotropy upon decreasing temperature. These two scalings are thought to trigger the triangular to square lattice transition through skyrmion elongation by directional expansion and subsequent rearrangement [99, 58]. The interplay of topological stability with an enhancement of q demands spin textures which satisfy conservation of skyrmion number between triangular and square phases. In thin plate samples, this is accomplished via the directional expansion of skyrmions into deformed bar and L-shaped elongated textures whose directionality is determined by magnetic anisotropy [117, 232]. In bulk samples, conservation of skyrmion number can be achieved through solutions which increase the volume occupied by each skyrmion, such as in deformed textures similar to [117, 232], or alternatively through solutions which decrease the volume occupied by the square lattice of skyrmions.

For our sample, the ratio of skyrmion density in the triangular phase at 310 K, to the square phase at 28 K, is given by $\frac{\rho_S}{\rho_T} = \frac{\sqrt{3}}{2}(\frac{Q_S}{Q_T})^2$ [116], where ρ_S and ρ_T are the skyrmion densities in the square and triangular phases, and Q_S and Q_T are the positions of the magnetic reflections for the square and triangular lattice forms in q-space. This expression derives from considering the ratio in packing density for an ideal triangular lattice ($\frac{\pi}{2\sqrt{3}}a_T^2$) versus square lattice ($\frac{\pi}{4}a_S^2$) given their lattice periodicity's, a_T and a_S, as defined by Q_T and Q_S in q-space. The q-centers for each phase were extracted as the peak centers from Gaussian functions fit to radial averages of the SANS images. This yields a ratio of $\frac{\rho_S}{\rho_T} \approx 1.78$, consistent with [116]. However, to keep skyrmion density constant between idealized triangular and square lattice phases, the square lattice constant should decrease by a factor of $\sqrt{\frac{2}{\sqrt{3}}} \approx 1.075$ corresponding to a square q value of 0.0056 Å^{-1}, contrary to our observed value of 0.008 Å^{-1}. Thus the skyrmion density violates conservation of topological charge when assuming a perfectly ordered square lattice. This can be resolved through solutions which decrease the volume occupied by the square lattice by incorporating additional magnetic structures with no topological charge that are defined by the same orthogonal double-q vectors, such as with helical or conical domains.

In the special case of a disordered square lattice transition pathway, the emergence of some net four-fold order when coming from a jammed labyrinth state suggests three possible physical cases. In the first case, skyrmions are nucleated from the mixed helical state present in the disordered phase, with their alignment determined by the direction of increased anisotropy. In the second case, an in-plane elongation and subsequent reorientation of the tubes may partially disentangle trapped domains and jammed states along distinguished direction, nucleating new skyrmions. In the final case, the in-plane elongation of the jammed state through merging and subsequent reorientation yields a deformed nematic-like square texture, similar to [232, 117]. In all of these cases it appears that, in order to overcome some of the jamming inherent to the disordered state, a change in topology is required in order to allow for skyrmion restructuring/reorientations through elongation, merging, and nucleation processes. For our material, we stipulate that mechanism (2) or (3) produces skyrmion reorientations that disentangle jammed states—improving skyrmion alignment and possibly nucleating oriented skyrmions upon disentangling. For mechanism (1), the magnetocrystalline anisotropy would have to increase to a large enough value so as to stabilize new skyrmions well below T_c however, for this doping series of materials, the only disconnected skyrmion phase observed at low temperatures is a disordered phase stabilized by magnetic frustration [140]. Whereas in support of (2) and (3), we have already observed skyrmion reorientations associated with anisotropic considerations [112, 224]. Note that mechanism (2) could still produce skyrmion textures reminiscent of (3) when transitioning in a disordered lattice, as skyrmions reorient and intersect jammed helical/skyrmion states, resulting in an elongated deformed skyrmion texture along a preferred q-direction consistent with anisotropy.

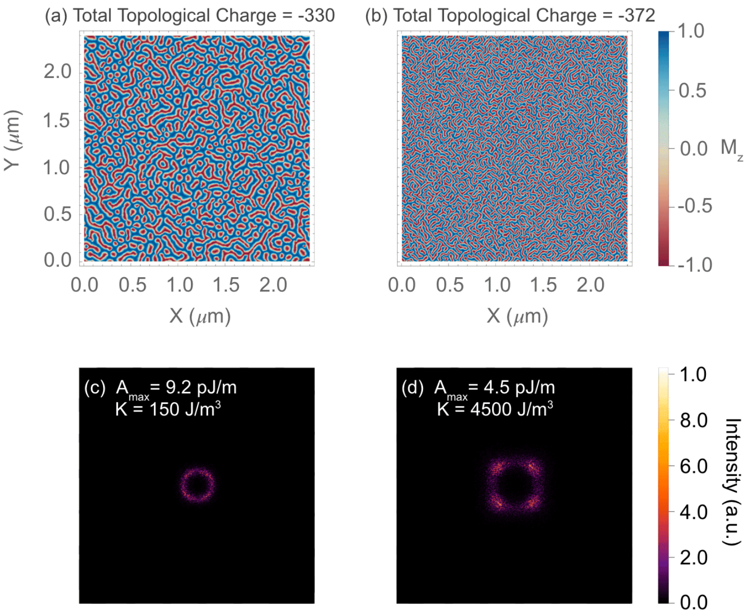

Figure 4.5: Micromagnetic simulations and their corresponding SANS patterns for a thin-plate $Co_8Zn_8Mn_4$ sample of dimensions 2.4 x 2.4 μm^2. Out-of-plane magnetization, M_z, is shown for the simulated triangular-to-square lattice transition starting from the initially disordered phase (a) phase at 310 K, to the disordered square phase at 30 K (c). The total topological charge per 2D slice is observed to increase during the transition by approximately 12%. Corresponding SANS images demonstrate an increasing scattering ring size, consistent with a reduction in A_{max}, while the development of four-fold order is observed in plot (d). Reprinted from [113].

Micromagnetic simulations performed on a disordered state suggest a transition pathway which entails a change in topology, contrary to observations made for ordered lattices [117, 232]. Simulations were performed using the Ubermag micromagnetic simulation package [236] on a lattice of size 2400 nm x 2400 nm x 5 nm, with a discretization cell size of 5 nm. A random spin configuration was initialized in an external magnetic field of 400 mT (along the z-direction) to mimic the experimental field-cooling procedures. A DMI constant of 0.00053 J/m was used [237, 232]. To simulate a disordered state with site-by-site disorder, a varying scalar exchange field was used, set to vary between 0 and a maximum value A_{max}. The equilibrium-square metastable lattice transition was performed by incrementally decreasing A_{max} from 9.2 pJ/m to 4.5 pJ/m to simulate the relative decrease in A/D ratio, while a cubic anisotropy term was simultaneously increased from 150 J/m^3 to

4500 J/m^3. The former change induces an enhancement of the q-vector, while the latter favors a particular elongation direction. While the decrease in A/D ratio may manifest a change in the helical periodicity similar to experiment, the primary origin of the change in q-vector is thought to be rooted in the low-temperature antiferromagnetic frustration of the Mn sublattice which can shorten the helical pitch and deform skyrmions [232, 238]. Similar competition between DMI and frustrated exchange interactions have been shown to produce short-size magnetic modulations [239, 240]. These simulation parameters were taken from studies which determined exchange and cubic anisotropy values as a function of temperature through soft X-ray scattering measurements coupled with simulations, and ferromagnetic resonance techniques [232, 115]. Relaxation times of 0.5 ns were introduced between each step. A two-dimensional magnetization slice of the out-of-plane magnetization M_z for the initial disordered state shows a mixed skyrmion and helical/labyrinth state, with a topological charge of -330 (Fig. 4.5a). A corresponding simulated SANS image exhibits a roughly uniform ring-like scattering pattern (Fig. 4.5c). Cooperatively decreasing A_{max} while increasing K shows results in a q-vector magnitude dependence consistent with our SANS data and $4\pi\frac{A_{max}}{D}$ which defines the helical pitch. Magnetization slices show a gradual merging and separation of labyrinth states, producing deformed skyrmions elongated along two orthogonal double-q vectors. These restructuring dynamics are in direct opposition to LTEM and micromagnetic simulation studies performed on ordered skyrmion states in [117] and [232], respectively. In the former two studies, deformation and elongation of the skyrmions along magnetic easy axis obeys conservation of topological charge. The deformations ensure the occupied skyrmion volume is constant despite the changing lattice shape and periodicity, thereby conserving skyrmion density. Conversely, our simulations demonstrate an increase in topological charge from -330 to -372 during the square lattice structural transition as skyrmion and labyrinth structures merge and dissolve, allowing skyrmion elongations and reorientations along preferred directions, which ultimately produce deformed textures reminiscent of [117]. The simulated and experimental SANS patterns exhibit a similar conversion from a ring-like to four-fold pattern. These results reinforce the requirement of a change in topology when undergoing disordered-to-ordered square structural lattice transitions. This observation suggests the disordered square lattice transition takes place by a unique pathway, not accessible by ordered states, which involves the merging and separation of helical and labyrinth states. This restructuring enables skyrmion nucleation, elongation, and reorientations necessary for the disordered square lattice structural transition.

4.5 Ordered Metastable Skyrmion Transitions

For the (O)E-T-SkX phase shown in Fig. 4.6a, transitioning to the lower temperature phase marked the development of higher order scattering rings up to the third order, while the baseline ring intensity approached zero (Fig. 4.6b). The significant reduction in peak widths and baseline intensity in Fig. 4.6a versus Fig. 4.3b points towards improved rotational alignment and development of the skyrmion lattice. We attribute this to the increased rotational range of the ordering sequence, consistent with [112]. Similarly, the increase in scattering order and decrease in baseline intensity between the thermal equilibrium (Fig. 4.6a) and corresponding (O)M-T-SkX phase (Fig. 4.6b) implies a lengthening and/or nucleation of the tubes and therefore increase in correlation lengths, possibly due to reduced thermal fluctuations and increased pinning/anisotropy contributions. The presence of additional scattering rings are most likely attributable to a combination of multiple scattering and higher-order scattering processes.

Remarkably, saturation of the metastable skyrmion lattice into the ferromagnetic phase generates a memory effect upon re-entry into the metastable skyrmion field window. Namely, a diffraction pattern reminiscent of the pattern prior to saturation is observed after lowering the field, with similar azimuthal peak positions and a prominent anisotropy direction (Fig. 4.7a). This reemergence of a skyrmion diffraction pattern in the metastable phase of a previously annihilated skyrmion lattice suggests that a memory of the skyrmion lattice is present, even in fields high enough to destroy all skyrmion and spiral scattering signals. This memory effect is quite surprising given the underlying disorder of the material which tends to precipitate jammed, rotationally disordered states. The competition between this disorder and the tendency of skyrmions to nucleate and maintain their previous orientations is apparent in the slightly broadened peak widths. Previous FC procedures from the (D)E-T-SkX through the metastable phase demonstrated a disordered ring SANS pattern for the same field and temperature. The skyrmion order parameter provides an additional measure of the memory effect. In particular, not only does the state after saturation have to produce topological skyrmion states, but it must overcome the natural energetics of the phase which favors disordered states. Relaxation into a disordered state after saturation would be possible if there was a slight memory effect set by low-temperature pinning sites, with jamming energetics still dominating. However, the reproduction of previous skyrmion order, which was generated in a separate phase, overcomes the naturally disordered ground state of the metastable skyrmion phase. The generation of this ordered state therefore requires additional energetics not available in the metastable phase. Therefore, the degree of order that is retained after saturation, in spite of the phase's underlying tendency towards disordered ring-like states, strongly suggests a

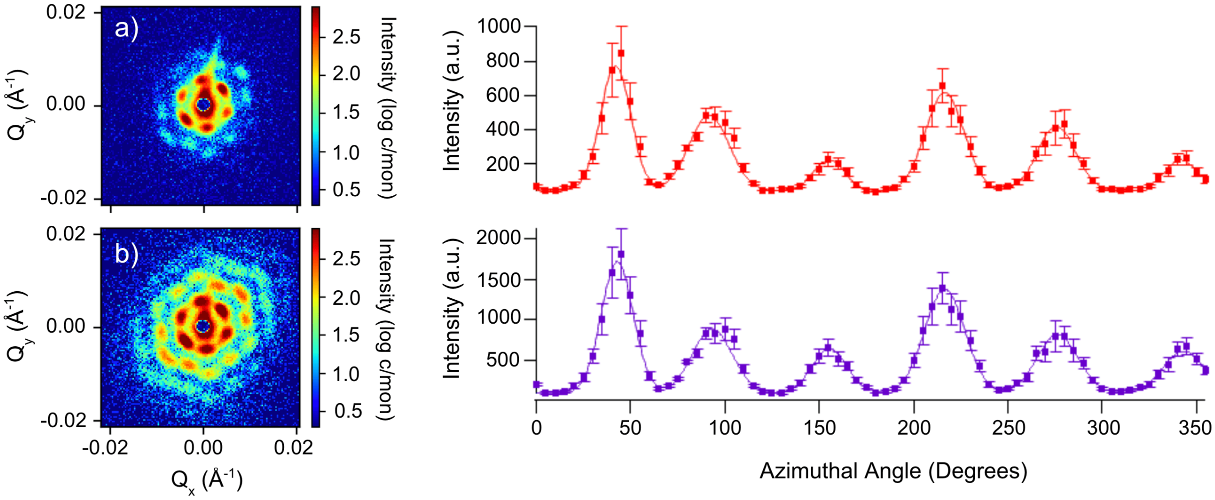

Figure 4.6: SANS diffraction patterns and their corresponding annular averages of their primary scattering rings for a) the sample after 20 rotations of the ordering sequence at 310 K in a magnetic field of 250 Oe, and b) after cooling to 173 K and 122 G from a). Solid lines are fits of the measurement points to six Gaussian peak functions with a constant baseline intensity. Note the baseline intensity essentially goes to zero from a) to b), and we observe the development of higher order scattering rings the more we cool into the (O)M-T-SkX phase. Both images are normalized to a fixed number of standard monitor counts to enable direct comparison between images, with the same scale for the color plots. Note the colorbar is a log-scale of intensity. Reprinted from [113].

memory effect.

Examining the influence of the ordering sequence on the memory effect provides an indication of the energetics of the phase. The ordering sequence was applied in fields of both 10 G (Fig. 4.7b) and 250 G (Fig. 4.7c). The baseline intensity is observed to slightly increase after the first ordering sequence, while the third and sixth peaks are further enhanced, reproducing previous peak asymmetries. This suggests the sequence may in fact orient skyrmions and helices, while also nucleating additional skyrmions from their pinning sites. These skyrmions appear to be both ordered and disordered, contributing to the peak and baseline intensities, respectively. This illustrates the dual nature of disorder: it may both enhance skyrmion development through defect pinning sites while also impeding reorientations and alignment through jammed chiral textures. Interestingly, there is significant development of the second order rings between ordering procedures, possibly indicating a lengthening of the skyrmion tubes, thereby reinforcing [125]. It is possible that

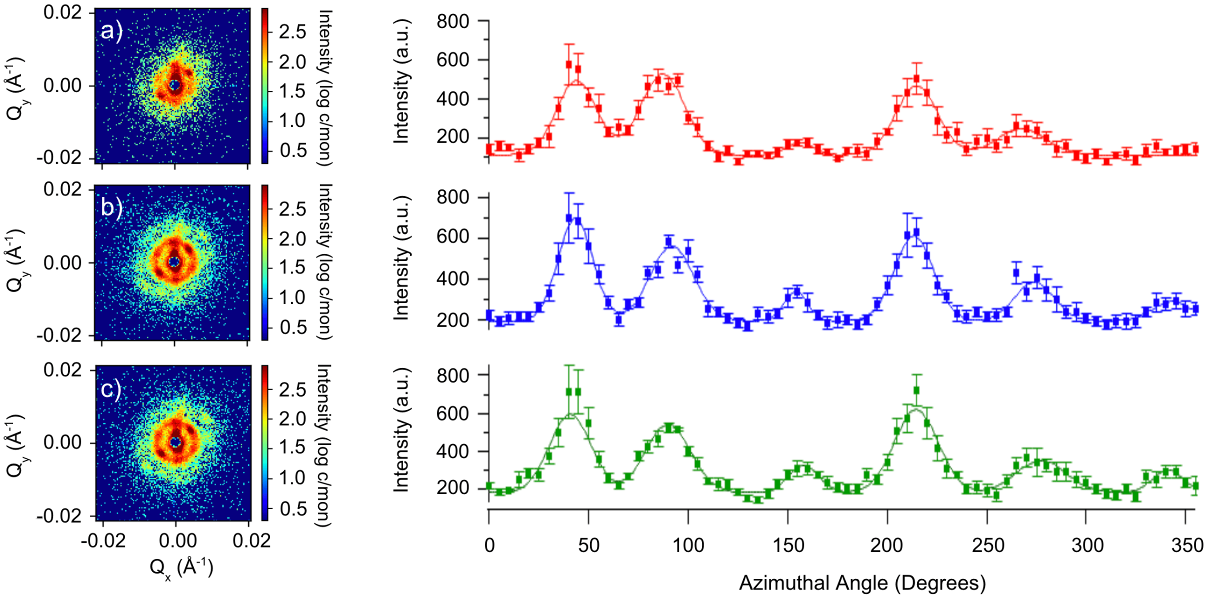

Figure 4.7: SANS images, and their corresponding annular averages of their primary diffraction rings for the (O)M-TSkX phase at 173 K upon a) lowering the field back to 10 G after saturation into the ferromagnetic phase in a field of 1 T, b) after 10 ordering sequence rotations in a field of 10 G, and c) after 10 ordering sequence rotations in a field of 250 G. Solid lines are fits of the measurement points to six Gaussian peak functions with a constant baseline intensity. All images are normalized to a fixed number of standard monitor counts to enable direct comparison between images, with the same scale for the color plots. Note the colorbar is a log-scale of intensity. Reprinted from [113].

the varying interplay of the magnetic field direction and anisotropy direction encourages an anisotropy favored elongation of magnetic torons into skyrmions [125]. Torons may be visualized as skyrmion fragments that terminate their prolongation on Bloch points [125]. These torons may exist as remnants of the previous skyrmion lattice [118]. Their survival is likely enhanced by pinning on defects. These defects may be naturally present in the material owing to internal disorder, which may be rooted in the site mixing of atoms [69] or presence of grain boundaries [235].

Upon further cooling, the square phase was entered, yielding four discrete peaks (Fig. 4.8). Comparing Fig. 4.8 and Fig. 4.4, we observe significantly increased scattering and discretization of the peaks for the square phase entered through the ordered phase, versus the disordered phase, emphasizing the role of previous order and/or pinning in structural

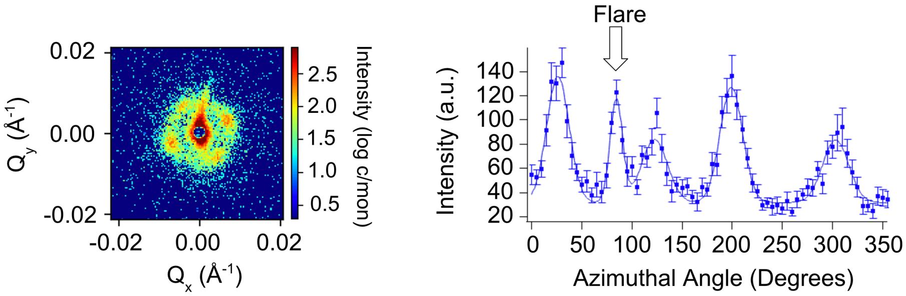

Figure 4.8: SANS image and it's corresponding annular average, for the ordered square lattice skyrmion phase. Solid lines are fits of the measurement points to five Gaussian peak functions with a constant baseline intensity. Measurement was taken at 60 K in a field of 6 G. The annular averages contains 5 peaks; the additional peak is due to a scattering flare from the surface of the sample. Note the colorbar is a log-scale of intensity. Reprinted from [113].

lattice transitions. Most likely, the cooperative increase in anisotropy and decrease in A/D drives a collective reorienting and elongation of skyrmion tubes, leading to an increase in scattering along distinguished directions, consistent with [117, 237]. The history dependence of the structural lattice transition on previous skyrmion order supports separate lattice transition pathways for ordered versus disordered skyrmion states. Namely, internal disorder has a strong influence on a skyrmion states ability to reorient, invoking different restructuring dynamics which may change the topology of the system.

Fig. 4.9a shows the azimuthally integrated radial $|q|$ dependence for triangular, metastable triangular, memory, and square skyrmion SANS images. All forms of triangular skyrmion lattice, i.e. equilibrium, metastable, and memory, display similar peak centers. Likewise, the two square lattice phases also exhibit similar peak centers, shifted to larger q relative to the triangular ones, consistent with [99, 116]. The two square phases display comparable scattering intensities, while the triangular phases are more varied in their respective scattering intensities. This larger variability in scattering intensity amongst the triangular lattice phases may be representative of the overarching diversity of stabilization mechanisms for the triangular versus square skyrmion phases, enabling the triangular lattice forms to achieve larger ranges of skyrmion development, i.e., formation, penetration, and alignment. Fig. 4.9b demonstrates the degrees of order for the various skyrmion phases, encapsulated in the angular peak widths as a function of temperature. Angular peak widths were calculated using the average of the azimuthal peak widths of the primary scattering ring, multiplied by the radial q location of the peaks taken from fits to data in Fig. 4.9a.

We note that although the two square phases are stabilized through two different pathways (i.e., ordered versus disordered), and display varying degrees of order, their comparable intensities may suggest square lattice formation occurs via a similar driving mechanism for this particular compound, with limited development/proliferation throughout the material. It is indeed possible that the square phase is not the majority phase, and is instead stabilized at surfaces, grain boundaries, and/or defects, resulting in its bounded formation irrespective of its transition pathway. If both the ordered and disordered square phases exhibit similar final states, the lattice transition must produce comparable skyrmion elongation and reorientation in the ordered and disordered states, precipitating similar volume fractions. This may suggest the presence of a dominant conical domain in the square lattice phase. There also appears to be an increase in diffuse scattering in the disordered square phase, suggestive of increased local disorder. This may result from disorder-enhanced q-vector fluctuations brought on by the deformation of the disordered triangular lattice state during the square lattice transition. Conversely, the presence of diffuse scattering in the thermal equilibrium phase may be indicative of thermal fluctuations or coexisting precursor helical or conical phases near the skyrmion phase boundary.

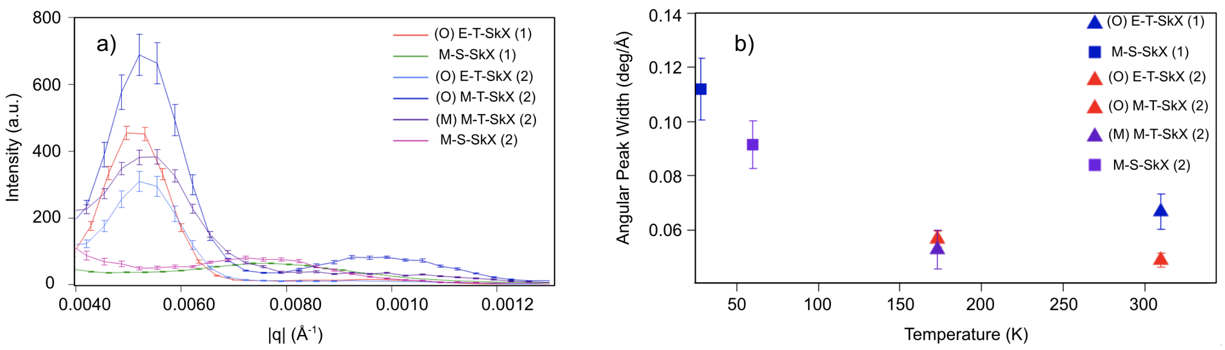

Figure 4.9: Radial $|q|$ dependence of SANS intensity, integrated azimuthally over entire SANS image for q $\geq$ 0.0040 Å^{-1} (smaller q was excluded due to the presence of flares) for triangular, metastable, memory, and square skyrmion phases (a). Angular peak width as a function of temperature for triangular, metastable, memory, and square skyrmion phases (b). Angular peak width is defined as the q value of the primary diffraction rings as determined from radial averages a), multiplied by the average peak widths extracted from the annular averages in Figures 4-8. Reprinted from [113].

Estimates of the relative skyrmion volume fractions for the (O)M-T-SkX vs (M)M-T-SkX phases can be generated by comparing the summed radial $|q|$ intensities. For a magnetic skyrmion sample, the scattered neutron intensity will depend on the saturated magnetization, the correlation length of the magnetic structures, and the volume fraction occupied by those structures. As an approximation, we may perform SANS simulations on magnetization arrays of various skyrmion volume fractions, with a fixed correlation length, to examine their independent influence on scattered neutron intensity. Magnetization arrays of size 640 nm x 640 nm x 2048 nm were generated with discretization cell sizes of 5 nm using the micromagnetic simulation package Ubermag [236]. Assuming contributions to the hexagonal diffraction patterns arise solely from skyrmionic structures which occupy the entire lattice volume, we may take their ratio in scattered intensities and use this to determine the approximate difference in skyrmion volume fraction. We created composite magnetization arrays of skyrmion domains with a ferromagnetic domain of varying volume fraction. We concern ourselves primarily with coexisting skyrmion and ferromagnetic domains, since we transitioned directly from the ferromagnetic to skyrmion state without crossing the zero field boundary. In doing so, we can estimate the relative change in skyrmion volume fractions for the ordered metastable skyrmion phase versus its memory counterpart. Hysteresis and low-temperature trapping of ferromagnetic domains is possible after saturation, with ferromagnetic contributions to the scattered intensity masked by the beam block, resulting in a reduced scattered intensity. While other chiral and/or non-chiral domains such as conical and helical are possible, decoupling the multi-variable contributions of the domain types and their correlation lengths is beyond the scope of this paper. Conical domains could similarly appear to reduce the scattered neutron intensity, with contributions only accessible in the perpendicular field geometry. Alternatively, helical domains could both increase and decrease the SANS intensity as a complex function of their longitudinal correlation lengths.

SANS simulations were performed for fixed size polydomain magnetization volumes with triangular lattice skyrmion volumes and ferromagnetic volumes shown in Fig. 4.10. The scattering intensity was examined for varying skyrmion lattice and ferromagnetic volume fractions, integrating the scattering intensity over the first order scattering ring. The scattering intensity was observed to decrease for increasing ferromagnetic volume fractions, displaying a linear relation (Fig. 4.10). The experimental SANS images were integrated over an annular region from q=0.0040 Å^{-1} to q=0.0080 Å^{-1} capturing the entire first order scattering ring, while excluding contributions from flares and higher orders. The ratio of the intensity in the (O)M-T-SkX (2) to (M)M-T-SkX (2) phases is $\simeq 1.4$. Assuming the (O)M-T-SkX phase has a skyrmion volume fraction of 95 %, we can estimate a decrease in the skyrmion volume to 68 % in the memory state.

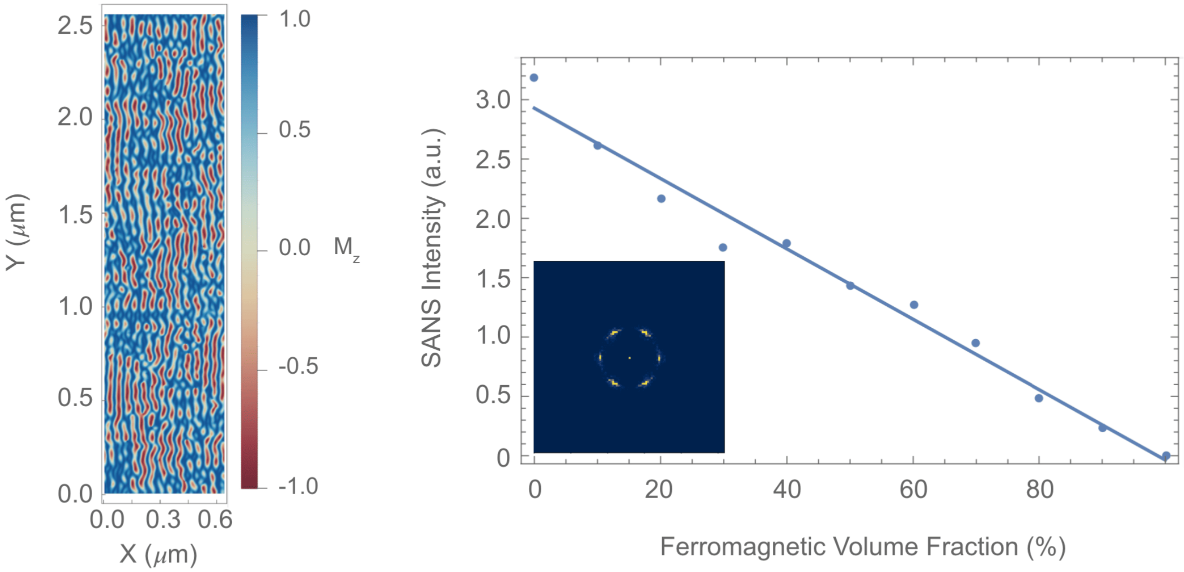

Figure 4.10: Simulations demonstrating the relationship between skyrmion to ferromagnetic volume fraction and scattered neutron intensity. XZ magnetization slices of the out-of-plane magnetization component, M_z, are displayed for the skyrmion magnetization volume. The simulated SANS intensity is plotted as a function of the ferromagnetic volume fraction in the magnetization array. A simulated SANS image is displayed in the bottom left corner of the plot for a composite magnetization arrays consisting of a triangular skyrmion lattice and ferromagnetic domain with 100 % and 0% volume fractions, respectively. The SANS intensity demonstrates a linear relationships which decreases for increasing ferromagnetic volume fractions. Reprinted from [113].

4.6 Discussion

Our SANS measurements demonstrate three distinct regimes in which thermal fluctuations, pinning, and anisotropy terms dominate skyrmion ordering responses and reorientations. A collective reorientation takes place in the thermal equilibrium phase, while pinning and memory effects are observed to enhance skyrmion stability in the metastable triangular phase. A new disordered-to-ordered skyrmion square lattice structural transition is revealed through elongations which necessitate a change in topology in order to enable reorientations of the jammed state to a deformed square pattern. This is reinforced through micromagnetic simulations on a disordered lattice as exchange and anisotropy parameters are incrementally varied, demonstrating an increase in topological charge during the transition through the breakup of labyrinth domains which nucleates deformed skyrmions. Together, these observations emphasize the fundamental mechanisms and interplay of magnetic anisotropy and defects in skyrmion stabilization and structural lattice transitions.

One might expect a disordered triangular skyrmion lattice to display similar degrees of disorder in the square lattice phase (b.3 of Fig. 4.11). In the extreme case, such disorder may even inhibit the triangular-to-square structural lattice transition, where pinning defects and trapped chiral domains preclude skyrmion elongation and reorientations, and suppress the monopole motion required for the breakup or merging of labyrinth domains. On the other hand, a finite amount of disorder may facilitate skyrmion ordering and transitions by lowering the barrier for monopole-antimonopole creation. In addition to the influence of disorder on square lattice transitions, the cruciality of anisotropy in such transitions has been reinforced across multiple studies. In MnSi the triangular-to-square lattice transition in quenched skyrmions entails a pathway in which the combination of reduced net magnetization upon decreasing magnetic field, and favored magnetic moment directions due to anisotropic perturbations, produced skyrmion reorientations which generate the square lattice [100]. Additional triangular-to-square lattice pathways invoke an increase in easy-plane anisotropy, in which anisotropy favored growth of skyrmions leads to skyrmion overlap, and the subsequent triangular-to-square lattice transition [58]. Most recent studies for this material suggest that the role of anisotropy in ordered square lattice transitions is to set the preferred direction of distortion of the peaks. However, our simulations reveal that the combination of varying exchange and anisotropy is required for the new disordered square transition pathway, which invokes a change in topology. As mentioned previously, anisotropy may contribute to elongation and reorientations, while disorder-related defects may lower the energy required for topological transitions, overcoming the topological protection of skyrmions.

The memory of the previous skyrmion lattice in the (O)M-T-SkX phase persisted in spite of saturation to the ferromagnetic phase—marked by the disappearance of all skyrmionic and spiral scattering signals. The recovery of the same approximate azimuthal peak positions and relative peak intensities, despite the predisposition of the skyrmion phase to disordered and jammed states, further underscores the origin of this phenomena to be memory based. One might expect such a memory effect, owing to the “frozen in” nature of the metastable phase, as shown in the upper plot c.3 of Fig. 4.11. One possible explanation for this apparent memory may lie in low-temperature pinning phenomena and enhanced magnetic anisotropy, highlighting the fundamental stabilization energetics of skyrmions in the metastable phase. This result is consistent with skyrmion memory observations made in Cu_2OSeO_3, in which the memory of skyrmion lattice states persisted after increasing the magnetic field to the field polarized state [118]. This memory effect however, did not persist in zero field and was demonstrated in a well ordered triangular phase that did not require any previous ordering procedures. Our memory effect is made substantially more robust by the fact that it exists in the absence of a magnetic field, and occurs in an inherently disordered material, demonstrating a complex competition of stabilization energetics. The latter may be highlighted by the slightly enlarged peak widths for the memory state. One may deduce the competition between previous pinning, which favors the same peak locations and widths, and underlying disorder which favors smeared ring-like patterns. The intensities of our peaks are, however, significantly reduced indicating underdeveloped skyrmion lattice formation as compared to it's original state. Simulations in which the skyrmion-to-ferromagnetic volume fraction ratio was varied suggest a decrease in the skyrmion volume fraction from an assumed value of 95% to 68%. The remaining skyrmion volume fraction in the (M)M-T-SkX phase should be correlated with the disorder in the material, which determines the number of defect pinning sites, and therefore possible locations for toron survival. This suggests the polycrystallinity of the sample may contribute to the observed memory through grain boundary disorder and domain intersection. Examining the same memory effect for an ordered lattice would help elucidate the interplay of skyrmion memory and disorder (such as pinning defects, polycrystallinity, and complex jammed energy landscapes).

Skyrmion lattice correlations extending beyond the skyrmion envelope have also been shown to exist upon FC in $\mathrm{Fe}_{1-x}\mathrm{Co}_x\mathrm{Si}$, producing a metastable phase, where intensities almost two orders of magnitude smaller than in the A phase are thought to indicate origins rooted in surface or edge pinning [102]. On the other hand, previous studies using Magnetic Force Microscopy (MFM) on a polished surface of $\mathrm{Fe}_{1-x}\mathrm{Co}_x\mathrm{Si}$ have demonstrated the preferential and reproducible decoration of certain positions on the surface with metastable skyrmions during field-cooling runs, owing to enlarged local potential barrier at defect pinning sites [241]. Given the chemical disorder inherent to this material, which stabilizes a high density of defects, it is possible that the skyrmion memory is encoded and survives in the form of isolated skyrmions (or torons as suggested in [118, 109]) confined to preferential positions, attributed to defect-related pinning. One fashion in which the skyrmion lattice may then propagate between these isolated skyrmions, which set the lattice orientation, is by a monomer-by-monomer addition type mechanism previously observed in [242]. Theoretical evidence of isolated skyrmions have been shown to exist as metastable objects within the saturated phase for a broad range of uniaxial anisotropy in the phase diagram of [86]. It would therefore follow that the underlying disorder in the material, both compositional and crystalline, plays a considerable role in the observed memory. Thus, the pinning of the skyrmions may be enhanced at lower temperatures and with increased anisotropy.

Studying composition effects via chemical substitution enables a pathway in which one can manipulate the delicate balance of stabilization energy terms, while introducing additional disorder and pinning effects. In particular, exploring the memory effect as a function of x,y concentration in $Co_xZn_yMn_{20-x-y}$ would illuminate the role of defects and anisotropy in the skyrmion memory phenomena. Additionally, one could examine the influence of disorder induced by grain boundaries in polycrystalline samples by performing the memory procedure for varying levels of sample crystallinity, with powdered samples used in the extreme case. Studying the persistence of the memory effect as a function of the strength of the saturating field could provide an estimate on the lower bound of the energy barrier of defect-related pinning. Moreover, exploring the memory effect as a function of the temperature and field of the metastable lattice, before saturation, would highlight the fundamental stabilization energetics of skyrmions in the metastable phase. Future experiments may also vary the time over which the magnetic field is reduced back to its skyrmion envelope value, and in so doing probe a characteristic time scale over which the skyrmion memory persists, similar to metastable skyrmion lifetime estimates in [101]. Noting that the (O)E-T-SkX phase does not exhibit the same memory effect upon saturation into the ferromagnetic phase—the disordered ring SANS pattern is regained—reinforces the disparate nature of the stabilization and formation mechanisms of the thermal equilibrium versus metastable phases; that is, thermal agitation, disorder, and topological stability. Performing simulations which examine lattice transition pathways and memory effects as a function of disorder levels would help establish a boundary between regimes of disorder which facilitate and inhibit skyrmion lattice transitions and stability. This could be used to establish ideal defect densities for enabling skyrmion reorientations and enhancing stability, guiding the tailoring of future material parameters for spintronic applications. We intend to further explore skyrmion formation and stabilization mechanisms across multiple phases in the bulk using a newly developed reconstruction algorithm [229], as well as incorporate spin dynamics [160, 197, 195].

The presence of secondary and tertiary scattering rings may provide additional information as to the long range magnetic order of the skyrmion lattice through reconstructions with higher-order diffraction peaks. Unfortunately, multiple scattering tends to overwhelm higher-order harmonics in the underlying structure. From an experimental point of view, Renninger scans may be employed to quantitatively distinguish the two mechanisms by "rocking out" the condition for multiple scattering. Renninger scans were performed in a bulk sample of MnSi, revealing higher-order diffraction to arise from an interference effect [228]. These scans may be performed in the future on this sample as a function of field and temperature to map out higher-order versus multiple scattering contributions in phase-space. Alternatively, in theory, given an ideal skyrmion sample with instrument

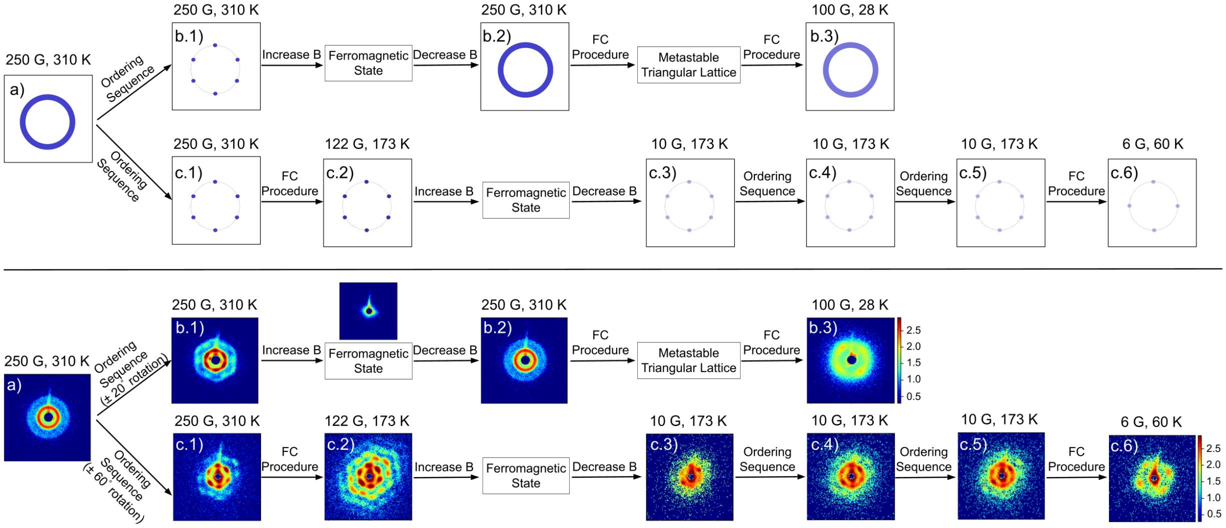

Figure 4.11: Schematic of expected SANS results for outlined experimental procedure (upper panel), and corresponding real SANS results (lower panel). Note: the central peak for the ferromagnetic phase is masked by the beam block, while prominent flares are able to leak out in the SANS image. All SANS images are normalized to a fixed number of standard monitor counts to enable direct comparison between images, with the same scale for the color plots. Note the colorbar is a log-scale of intensity. Reprinted from [113].

resolution limited peak widths, second-order diffraction is indistinguishable from multiple scattering which takes the form of a self-convolution of the first-order peaks with themselves. However, in the case of a disordered sample, the two effects become distinguishable as the first-order diffraction pattern is convolved with some kernel which has cylindrical symmetry. As a result, the radial and angular peak profiles of the primary and secondary rings will be equivalent for the case of higher-order diffraction. For the case of multiple scattering, the 12 secondary peaks will have alternating larger radial widths and smaller angular widths relative to the 6 primary peaks. To determine the approximate ratio of the two effects one can, in theory, unwrap the images in polar coordinates and determine a linear combination of the simulated higher-order diffraction and multiple scattering images that would produce the experimentally measured intensities in frequency space. Unfortunately, given the low signal-to-noise ratio for the secondary peaks in these datasets, this type of analysis is not trivial.

4.7 Conclusions

In conclusion, we have shown skyrmion order, and ordering ability, to vary as a function of phase. Discrepancies in skyrmion lattice transition and metastable phenomena for ordered versus disordered samples were revealed through a newly established disordered-to-ordered square lattice transition pathway and metastable triangular lattice memory effect. These results greatly enhance our understanding of skyrmion stabilization and formation mechanisms for thermal versus metastable phases, demonstrating the interplay of topological stability with a tunable energy landscape of exchange, anisotropy, disorder (i.e. defects and pinning), field, and temperature. Ultimately, our work has provided a valuable account of skyrmion stabilization/formation and lattice restructuring dynamics as a function of disorder, establishing new pathways for skyrmion manipulation and enhanced stability for future devices.

Chapter 5

Three-Dimensional Neutron Far-Field Tomography of a Bulk Skyrmion Lattice

The study presented in this chapter is reproduced and adapted from [243].

Skyrmions are thought to nucleate and annihilate along their depth on points of vanishing magnetization, called Bloch points, as described in section 1.3. However, owing to a lack of bulk techniques, experimental visualizations of skyrmion lattices and their stabilization through defects in three-dimensions remain elusive. In this chapter, we present three-dimensional visualizations of a bulk $Co_8Zn_8Mn_4$ skyrmion lattice through a tomographic algorithm which processes multi-projection small angle neutron scattering measurements to generate mean scattering feature reconstructions (MSFR) of the bulk spin textures. Digital phantoms validated the algorithm; reconstructions of the sample show a disordered skyrmion lattice with a topological saturation of 63 %, exhibiting three-dimensional topological transitions through two different emergent (anti)monopole defect pathways with densities of 147 μm^{-3} and 21 μm^{-3} for branching and segmentation events, respectively. These results serve as the first experimentally-informed visualizations of bulk skyrmion lattice structures and defects in three-dimensions, providing novel insights into skyrmion stabilization and topological transition pathways. This technique opens the door to future studies of bulk skyrmion behavior on unprecedented lengthscales, guiding the development and manipulation of skyrmion materials for spintronic applications.

5.1 Skyrmions in Two Dimensions and Confined Systems

In three-dimensions, the uniform stacking of the two-dimensional skyrmion spin structure produces skyrmion tubes elongated along the external magnetic field direction, thought to penetrate surface-to-surface [244, 97]. In physical bulk crystal systems at non-zero temperature, a finite density of defects exist, interrupting the skyrmion string propagation [121]. Because the emergent flux that defines skyrmions is quantized, their nucleation and termination is mediated by emergent magnetic charges that must also be quantized [59]. Skrymion tube segmentation and branching via emergent magnetic monopoles and anti-monopoles (denoted S^+, S^-, B^+, and B^-, respectively) are believed to mediate skyrmion topological transitions [60]. Motion of such defects in response to changes in external parameters, such as field or temperature conditions, have been proposed to drive a change in skyrmion topology through the unwinding of individual skyrmions [121, 60] and the zipping/unzipping of neighboring skyrmion tubes [59, 122, 60]. Since total emergent charge is conserved, skyrmionic transitions can only take place in three-dimensions when emergent (anti)monopoles are either pinned to a material defect or jammed in place and unable to overcome the activation energy required to travel to the material surface or reach an oppositely-charged monopole to annihilate [123, 122, 69].

As discussed in section 1.2, examinations of skyrmions using two-dimensional imaging have revealed a myriad of in-plane skyrmion string deformations including elongated structures [59] and bent skyrmion strings which terminate on the surface [92] or form at edges [69], while three-dimensional imaging in confined systems has revealed axial modulation of skyrmion tubes [70]. In all of these instances, the physical systems being probed are subject to constricted geometries by virtue of the thin-plate or needle-shaped samples required by the techniques. This introduces confinement effects, causing the system to exhibit drastically different energetics to those of bulk samples, favoring surface-pinning [91] and edge-interactions [73, 94, 69] which affect skyrmion formation, shape, interactions, dynamics, and stabilization. Recent advances in the imaging and reconstruction of three-dimensional magnetization vector fields have been made using X-ray magnetic microscopy [245, 246] and nanotomography [247, 248] techniques, exploiting dichroism in magnetic scattering and element-specific absorption contrast. However, such methods maintain low penetration depths, bounded material thicknesses and compositions, and require vacuum-compatible setups which typically limit angular sampling [248]. A recent study [126] confirmed the presence of interrupted and merging-type skyrmion strings in a sparsely populated micrometer sized thin plate needle-shaped sample of $Mn_{1.4}Pt_{0.9}Pd_{0.4}Sn$ using scalar magnetic X-ray tomography. The observations, however, are limited to individual skyrmion strings in a sample thickness only a few times the skyrmion tube diameters, whose confined geometry and thickness gradient fundamentally alters the skyrmions shape and behaviour; bulk lattice skyrmion behavior has yet to be experimentally observed.

5.2 Reconstruction Technique

Small angle neutron scattering (SANS) is sensitive to bulk scattering features, enabling studies of truly bulk skyrmionic systems along different paths through the sample's phase diagram. In particular, spatially averaged depth information may be obtained by forming rocking curves, integrating over one or more diffraction peaks as a function of sample angle, to extract the longitudinal correlation length of a skyrmion lattice [228]. The effects of recent external magnetic field and temperature history on jammed states has been shown using SANS, where skyrmion lattice defect densities were reduced using an ordering sequence where the external magnetic field is rocked relative to the sample [112]. Rocking the sample in the field [112, 224] produces skyrmion lattice reorientations which disentangle the jammed state, promoting additional skyrmion formation [112, 224], unless the segmentation defect creation barrier is too high or the pinning potential is too strong to liberate existing defects [124, 224, 113].

Whereas previous studies are confined to surface-level techniques, confined systems, or integral far-field SANS measurements which cannot produce real space representations of the sample, here we perform tomography of the thermal equilibrium triangular skyrmion lattice phase to generate a three-dimensional mean scattering feature reconstruction of a bulk skyrmion lattice. While, existing neutron scattering tomography techniques have applied contrast imaging methods and phase-retrieval algorithms to multi-projection ultra small angle neutron-scattering datasets to reconstruct two-dimensional sample cross sections [249] and scattering length density maps of periodic structures [229], respectively, the technique presented here takes somewhat of a divergent approach, coupling the angular projection datasets with a free energy regularization. In particular, our reconstruction algorithm consists of first forming an estimator of a multi-projection set of SANS measurements by operating on the incoming neutron state with a forward operator, which takes the MSFR volume as its main input. Next, the sum of weighted residuals between the estimated and measured SANS patterns for multiple projections is minimized with respect to the MSFR. Without integrating over peak areas before forming the rocking curve, the χ^2 is sensitive to shifting peak locations, shapes, intensities, and correlations. The number of free parameters depends on the chosen MSFR volume, but will usually be larger than the number of data points in the set of SANS images. The large degeneracy of possible solutions and danger of overfitting the data is overcome by adding a free energy regularizing functional to the objective function $f = \chi^2 + \beta F$, where the χ^2 is the weighted sum of measurement residuals, F is the free energy of the MSFR, and β is a Lagrange multiplier reminiscent of a Boltzmann factor. The free energy includes the Heisenberg exchange, Dzyaloshinskii-Moriya (DM) exchange, and external field Zeeman terms and could be made to include additional interactions which are functionals of the spin density, though such terms are beyond the scope of the present work. Knowledge of the functional form of the free energy and average magnetization of the phase is therefore required for the application of this technique to a magnetic system. Similar techniques are often used in traditional computed tomography (CT) algorithms, in which case the total variation can be used as a regularizing functional [250]. The resulting MSFRs may be interpreted as containing the types of structures, and their densities, which are common within the sample. However, there is no portion of the sample which looks exactly like a MSFR, and there are a large number of possible MSFRs which would converge on a minimum of the objective function. Moreover, since the reconstructed magnetization volumes are representative of the bulk, they won't produce surface specific features (such as surface twisting [251, 97]) unless it is frequent throughout the sample, comprising a sizable volume fraction of the magnetic features. One can also view minimizing the objective function as performing a micromagnetic simulation with the χ^2 providing the local interaction and pinning potential terms in the free energy that cause lattice defects, thereby enforcing the lattice correlation lengths and structure encoded in the SANS patterns.

To compute the reconstructions, the cost function was minimized using a conjugate gradient method. The $\boldsymbol{m}^2 = 1$ constraint was enforced by defining search directions in terms of the angular fields $\Theta = \arcsin(m_z)$ and $\Phi = \arctan(m_y, m_x)$. Ten iterations were run with equal weights for all residuals, which can aid in convergence when measurement uncertainties are dominated by counting statistics and there are regions of low count rates. Following the ten iterations, 100 iterations were run with the weights given the measurement uncertainties provided by the SANS reduction software [227]. A maximum weight was introduced for the low-count rate regions to aid in convergence. The resulting average magnetization was found to depend on the weight given to the Zeeman term h, so reconstructions over a range of h and starting average magnetization $\langle m_z \rangle$ were performed (Table 1), with the preferred MSFR being the one that most closely matches the phantom or experimental average magnetization.

Details on the forward propagator, gradient, and defect density calculations are provided in Appendix A.

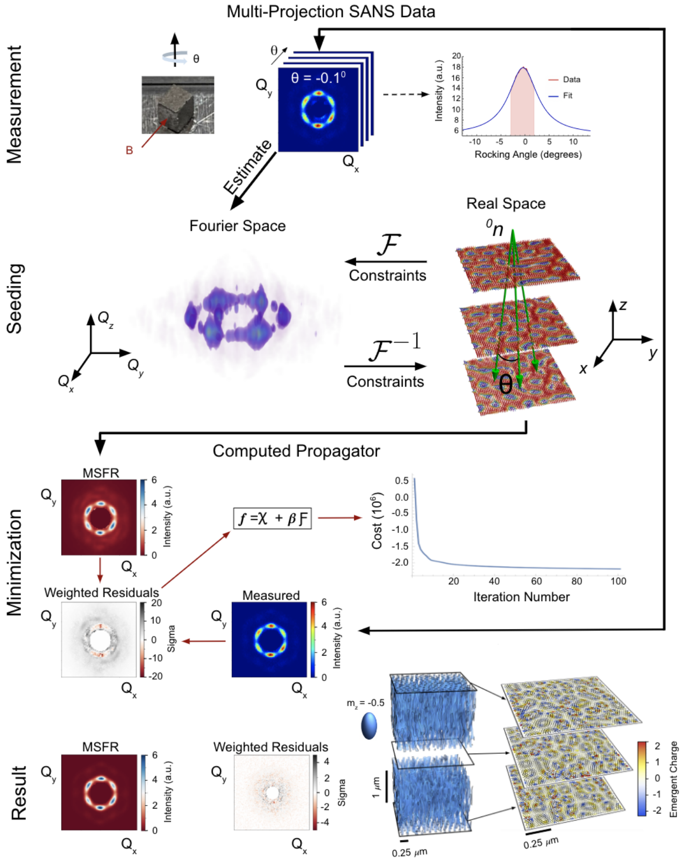

Figure 5.1: Schematic outlining the reconstruction technique, beginning with the collection of experimental SANS angular projections (top) and ending with the output MSFR (bottom). The experimental sample-field geometry used during tomographic rotations is shown, where the sample and magnetic field were rotated coincident about an angle θ ensuring a fixed magnetic orientation parallel to the surface normal of the sample. The rocking curve is plotted for one of the horizontal peaks, showing the measured and extrapolated regions of the Lorentzian curve. Estimated and measured SANS patterns are shown for the initial and final MSFR, including their weighted residuals and minimization of the cost function. The reconstruction is shown for the entire 12.3 μm^3 (1.8 μm×1.8 μm×3.7 μm) MSFR volume, with blue contours outlining the skyrmion tubes for an out of plane magnetization, $m_z = -0.5$. Zoomed in two-dimensional skyrmion spin textures are shown for 3 depths along the reconstruction with highlighted emergent magnetic charges. Reprinted from [243].

5.3 Small Angle Neutron Scattering Tomography

Multi-projection SANS measurements were made (Fig. 5.1) using an above-room-temperature skyrmion host, $Co_8Zn_8Mn_4$, whose characterization was described in chapter 3 ([224]). These measurements were performed at the NG7-30m beamline at the National Institute for Standards and Technology (NIST) for a 15 m beam configuration at a wavelength of 6 Å. The sample was field cooled from 420 K in a field of 250 G to 310 K. Upon entering the thermal equilibrium triangular lattice skyrmion phase a uniform ring manifested in SANS, indicative of a jammed chiral state composed of misoriented skyrmion, labyrinth, and helical domains [113]. The skyrmion sample was rotated symmetrically in the magnetic field 10 times over +/- 60 degree angular range to achieve the ordered six-fold pattern shown in (Fig. 5.1). From here, multi-projection SANS data was collected for a static skyrmion configuration, rotating the sample and field together on the same rotation stage about the vertical axis specified in (Fig. 5.1) to ensure the magnetic field orientation remained fixed—with the field direction parallel to the surface normal of the sample. These tomographic rotations were performed for 30 angles from -2.9 degrees to 2.9 degrees. Incorporating additional tomography axes may enhance the data, particularly in the case of sample tilting for skyrmion states with very short longitudinal correlation lengths, however, this is left for our future studies. The determination of the range and number of projections that should be collected for a given magnetization volume, or sample, is set by the correlation lengths of the phase. In the ideal case, the angular range should be sufficiently large so as to capture the entire decay of the rocking curve. Rotations past this point do not enhance the data unless there exist large off-axis domain structures or spin geometries in which the propagation wavevector lies parallel to the incident neutron direction. For example, conical domains may be probed by collecting angular projections about the perpendicular sample-field geometry, however, these are left as the subject of our future experimental explorations. For the case of highly disordered states characterized by long rocking curves with persistent non-zero angular intensities, this can lead to large angular ranges for the tomographic datasets, and can also present challenges for the rotation of cumbersome cryomagnets in the limited sample space available on typical SANS beamlines. In the experiment presented here, the ordered skyrmion sample and magnetic field were rotated through 30 projections over a 5.8 degree angular range, limited by the geometry of the guide field coils (Fig. 5.2a). Application of the ordering sequence seeks to both enhance the longitudinal and transverse correlation lengths of the phase while precipitating an oriented monodomain skyrmion lattice. Therefore, the ordering sequence should refocus intensity to the central peak of the rocking curve, while minimizing its FWHM and any potential persistent non-zero angular intensity offsets arising from misoriented chiral domains. As a result, the initial application of the ordering sequence enforces our measured angular range, while some of the rocking curve extrapolation performed at lower Q gets filled in by the $\langle m_z \rangle$ parameter and free energy term. To determine the implications for how a limited-projection dataset would effect our results, we reconstructed digital phantoms under both ideal conditions, where SANS data was simulated for 31 projections between ±15 deg about both axes (no compound rotations) and the actual experimental projections (see methods and ideal vs limited projection datasets in supplementary materials).

5.4 Phantom Generation

Digital phantoms were made by seeding an LLG relaxation using Ubermag [236] with a high-energy lattice made to have a fixed correlation volume. The LLG relaxation was stopped after ten iterations to retain a reasonable density of defects. The system used the free energy functional

$$E[\boldsymbol{m}] = -A\boldsymbol{m} \cdot \nabla^2 \boldsymbol{m} + D\boldsymbol{m} \cdot (\nabla \times \boldsymbol{m}) - \mu_0 M_s \boldsymbol{H} \cdot \boldsymbol{m}. \tag{5.1}$$

with exchange stiffness $A = 10$ pJ/m, Dzyaloshinskii–Moriya constant $D = 3.93 \times 10^{-3}$ J/m, saturation magnetization $M_s = 1 \times 10^6$ A/m, and external field values of $H = 0.2080$ T, 0.2780 T, and 0.3475 T for Phantoms A, B, and C, respectively.

The seed was generated by alternating between Fourier-space and real-space constraints. The magnitude of the sample magnetization in Fourier-space is set by the desired correlation volume; the real space magnitude of the sample magnetization was constrained to unity everywhere; and the transverse magnetization was set to be in the direction of the curl of the longitudinal magnetization.

SANS patterns were simulated by applying a forward operator to a randomly-selected and randomly-translated one of twenty phantoms made with differing random initialization. The resulting SANS images from repeating this process at least 100 times were averaged to simulate an incoherent neutron source and create the resulting simulated multi-projection SANS data.

5.5 Three-dimensional Visualizations of Skyrmions in the Bulk

The voxel size of the MSFR is determined by the Fourier-space span of the SANS images $dx = 2\pi/Q_{\text{tot}} = 2\pi/(dQ\ N)$. In this experiment $dx = 14.3$ nm, as determined by the resolution $dQ = 3.4\ \mu\text{m}^{-1}$ and size $N \times N = 128 \times 128$ of the SANS images. The height of the MSFR was set to 256 voxels, for a total volume of 1.8 μm×1.8 μm×3.7 μm= 12.3 μm^3. Two-dimensional slices of the measured and reconstructed SANS images, weighted residuals, and MSFRs are shown for the bulk sample and phantom set B with average magnetizations of 0.42 and 0.41, respectively (Fig. 5.2). Videos showing magnetization and topological defects as a function of depth for the phantoms and MSFRs are available with the supplementary materials [252]. Since the reconstruction technique does not provide a one-to-one spatial mapping to any volume within the sample, deviations between Fig. 5.2g and Fig. 5.2k are expected. However, comparison between the two in-plane slices shows the presence of similar topological structures, transitions, and skyrmion packing densities. A more accurate and comprehensive comparison entails looking at the entire input and MSFR volumes for average features and their densities. Average magnetization, topological saturation, and defect densities are compared in Table 1. Phantoms were generated with the external field near the helical-skyrmion boundary (Phantom A), the ideal value (Phantom B), and the ferromagnetic-skyrmion boundary (Phantom C). The choice of Zeeman term h, was set such that average magnetization of the reconstructions matched those estimated through magnetic susceptibility measurements. The required weighting of the Zeeman term h, to achieve the average magnetization that was estimated from DC-susceptibility, was affected by the χ^2. The favored MSFR are thus those with values of h which produce the estimated average magnetization and are highlighted in Table 1. The agreement between phantom and MSFR is reasonable for Phantoms B and C , with deviations between ideal and limited-projection datasets likely arising due to the truncated rocking curve of the limited datasets. However, the MSFR for Phantom A overestimates the branching defect density. This is likely attributable to the seeding, where Phantom A transitioned from an average magnetization of $\langle m_z \rangle = 0.4$ to $\langle m_z \rangle = 0.33$ during the free energy relaxation (see Materials and Methods), while the MSFR had a net magnetization change of $\langle m_z \rangle = 0.35$ to $\langle m_z \rangle = 0.32$, suggesting hysteresis-like effects can impact the fidelity of the reconstructions. Such effects are reminiscent of real samples, wherein sample histories and trajectories through phase-space may alter the stability, chiral and topological volume fractions, and defect densities of the phase [231, 131, 253]. Future studies may incorporate variations of the estimated $\langle m_z \rangle$ parameter to simulate and incorporate these hysteresis effects.

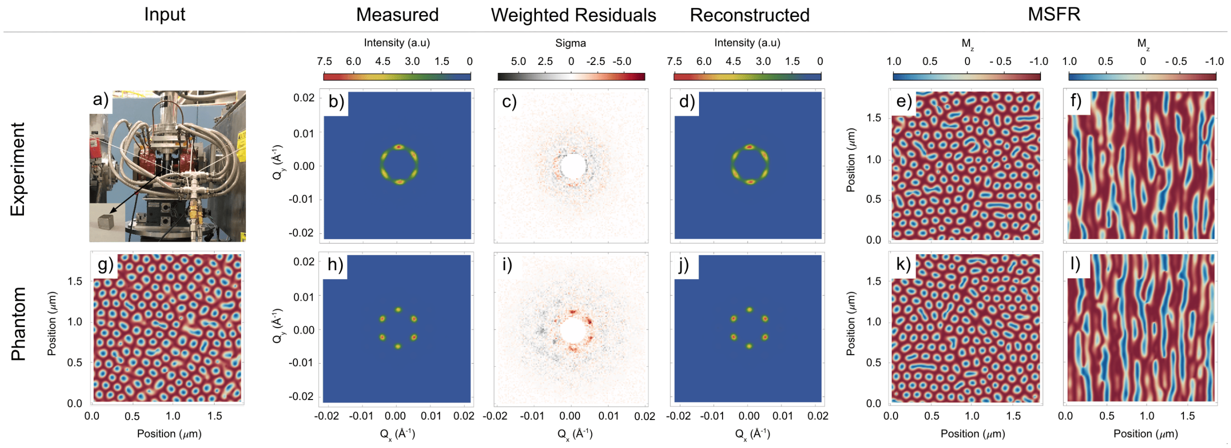

Figure 5.2: Experimental setup (a), measured SANS image (b) reproduced from [224], minimized weighted residuals (c), reconstructed SANS image (d), and xy (e) and xz (f) slices of the MSFR are shown in the upper panel. The lower panel shows the corresponding plots for the phantom B limited-projection dataset (see highlighted row in Table 1) where (g) is the simulated input magnetization, (h) is the simulation SANS pattern, and (i)-(l) follow the same as the upper experimental row. All SANS images are shown for the zeroth projection, with the guide field and sample aligned parallel to the neutron beam. XY and XZ magnetization slices are shown for a 1.8 μm×1.8 μm area of the MSFR, showing the full in-plane magnetization slice and half of the longitudinal magnetization slice. Reprinted from [243].

The sample MSFR topological saturation $N_{\mathrm{sk}}/N_{\mathrm{max}}$ is found to be 63 % of that of a perfect, skyrmion triangular lattice with the same Q_0. This is reflected by the presence of transverse and longitudinal lattice distortions. In particular, skyrmion voids, bimerons, and elongated spin structures present in the two-dimensional MSFR magnetization slices reduce the number of skyrmions from that of an ideal hexagonally packed lattice. Similarly, interruption of the skyrmion strings along their length may be visualized by taking an $x-z$ slice of the MSFR as shown in Fig. 5.2f.

Three-dimensional visualizations of portions of the sample MSFR show skyrmion nucleation and annihilation along their depth, where segmentation $\mathrm{S}^{\pm}$ and branching $\mathrm{B}^{\pm}$ (anti)monopoles mediate the change in topology at skyrmion transition points (Fig. 5.3e). These features are similar to those observed for simulations of skyrmion annihilation in three-dimensions through helical and conical pathways [60, 59, 122]. Notably, some branching events are observed to occur along wave vectors Q which are offset by 60 de-

	h	$\langle m_z \rangle_{\text{seed}}$	$\langle m_z \rangle$	$N_{\text{sk}}/N_{\text{max}}$	ρ_{branch}, μm^{-3}	ρ_{seg}, μm^{-3}	ρ_{tot}, μm^{-3}
Phantom A	0.56	0.40	0.33	65 %	101	37	138
MSFR A, ideal	0.50	0.30	0.28	52 %	322	7	329
	0.60	0.35	0.32	59 %	238	13	251
	0.75	0.40	0.37	65 %	150	26	176
MSFR A, lim. proj.	0.50	0.30	0.30	56 %	299	9	308
	0.60	0.35	0.34	60 %	233	13	246
	0.75	0.40	0.40	64 %	164	24	189
Phantom B	0.75	0.40	0.41	68 %	47	40	87
MSFR B, ideal	0.60	0.35	0.35	62 %	138	10	148
	0.75	0.40	0.38	64 %	115	12	127
	0.87	0.45	0.42	72 %	53	31	84
MSFR B, lim. proj.	0.60	0.35	0.35	60 %	166	6	172
	0.75	0.40	0.41	67 %	88	16	104
	0.87	0.45	0.45	69 %	53	31	84
Phantom C	0.94	0.40	0.47	73 %	13	103	115
MSFR C, ideal	0.80	0.42	0.41	69 %	133	27	161
	0.94	0.47	0.46	72 %	54	56	110
	1.08	0.52	0.49	72 %	21	91	112
MSFR C, lim. proj.	0.80	0.42	0.43	69 %	126	26	152
	0.94	0.47	0.49	72 %	46	63	109
	1.08	0.52	0.54	71 %	23	95	119
MSFR, sample	0.50	0.30	0.25	53 %	214	6	220
	0.60	0.35	0.35	59 %	163	13	176
	0.75	0.40	0.42	63 %	118	21	139
	0.87	0.45	0.48	66 %	69	37	106

Table 5.1: Zeeman term weight in reduced field units h, seeded average magnetization $\langle m_z \rangle_{\text{seed}}$, final average magnetization $\langle m_z \rangle$, topological saturation $N_{\text{sk}}/N_{\text{max}}$, and defect densities, ρ, of the phantoms and associated MSFRs and sample MSFR. The green highlighted rows correspond to the reconstructions that most-closely match the known $\langle m_z \rangle$ parameters—calculated from input phantoms or extracted through susceptibility measurements. The reduced field is fixed; all other parameters are computed from the spin density.

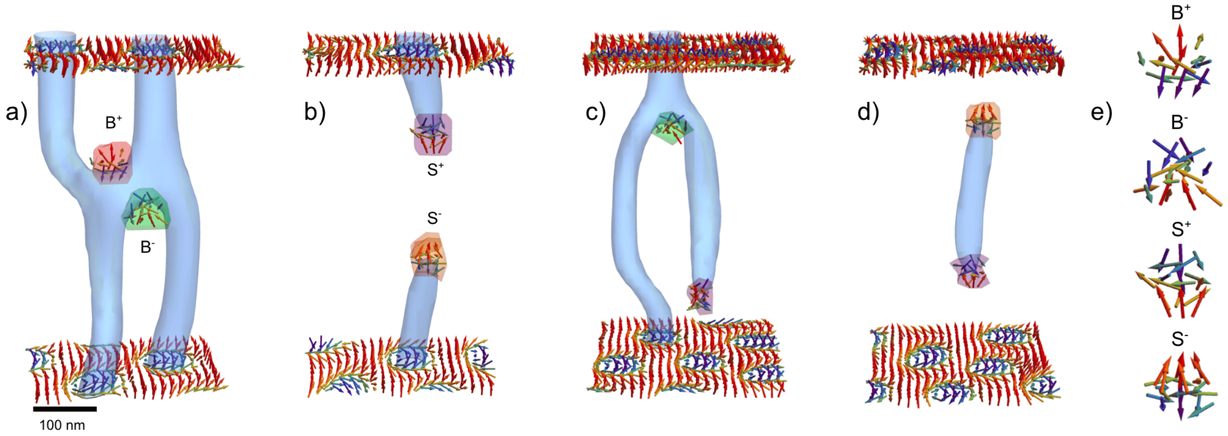

Figure 5.3: Characteristic topological transitions present in the MSFR showing branching and segmentation (anti)monopole pathways. The blue contours outline the skyrmion tubes where the out of plane magnetization, $m_z = -0.5$. Some of the skyrmion tubes are masked to highlight the regions undergoing changes in topology. Emergent magnetic charge density contours are shown for the two types of skyrmion topological transition processes with S^+, S^-, B^+, and B^- corresponding to purple, orange, red, and green, respectively. Branching (B) and segmentation (S) emergent (anti)monopoles are observed to occur at transition points along the tubes, displaying distinct spin textures determined by the sign of $\partial_z m_z$. Zoomed in spin textures are shown for the labeled branching and segmentation (anti)monopoles with each spin corresponding to one voxel (e). All skyrmion features are shown for a depth of 37 voxels, equating to 531 nm. Reprinted from [243].

grees from the horizontal nearest-neighboring skyrmion, producing a skyrmion twisting effect (Fig. 5.3a). Conversely, some instances of segmentation events exhibit pairs of $\mathrm{S}^{\pm}$ (anti)monopoles which cup skyrmions, producing spatially localized skyrmion filaments which extend longitudinally over a few lattice periods (Fig. 5.3d) and are reminiscent of magnetic torons [125]. Given the field history of the sample, wherein saturation to the ferromagnetic phase was performed prior to collection of the tomography data, these structures may represent a skyrmion survival mechanism in the field-polarized state via magnetic torons on defect pinning sites [113]. Future studies will be performed to examine the prevalence of these structures as a function of field history and average magnetization, shedding insight into skyrmion elongation and stabilization mechanisms.

The energy source required for emergent (anti)monopole creation may derive from internal chemical disorder present in the material (such as in material imperfections or site-disorder [60, 92, 124]), thermal activation [141, 38, 254], and the external magnetic field setting relative to the helical and ferromagnetic phase boundaries [38, 92, 59]. For the case of the magnetic field setting, segmentation and branching (anti)monopoles are thought to control skyrmion annihilation upon increasing and decreasing fields, respectively [59, 122, 80]. This is reinforced by reconstructions performed on equivalent datasets under different average magnetization and reduced field h conditions; a shifting prevalence from branching defects in the low-field case, to segmenting defects in the high-field case is observed.

The preferred sample MSFR shows segmentation and branching (anti)monopoles seemingly jammed in place and unable to travel to the sample surfaces or annihilate. The observed defect densities could be due to pinning potentials in the material which would trap the (anti)monopoles and inhibit their motion [124]. In this case, the prevalence of these structures may indicate the degree of internal chemical disorder, providing snapshots of magnetic defect pinning centers. Alternatively, these features may be evidence of an incomplete ordering sequence, wherein the limited magnetic field directions during rotation did not allow the monopoles to propagate along enough angular paths in the sample to completely breakup the jammed labyrinth domains [112]. Future SANS tomography measurements taken as a function of skyrmion ordering could decouple these two possibilities. Implementation with structured neutron beams, which possess an analogous non-trivial winding character in spin [197] or phase [194, 255], may provide estimates of the magnetic defect densities based on the vertical widening of the skyrmion peaks in the transverse geometry. Alternatively, the defects themselves may be viewed as the magnetic equivalent of phase singularities, capable of generating topological neutron states for probing nanometric sample topologies.

5.6 Conclusions

We have shown experimental visualizations of the three-dimensional character of a bulk skyrmion lattice through Mean Scattering Feature Reconstructions, generated via a SANS tomography technique. The present results uncover the stabilization and evolution of a triangular skyrmion lattice in the bulk through three-dimensional topological transitions which exhibit a mixture of distinctive segmenting and branching (anti)monopole defects. Exotic features for these two event types are observed in the MSFR, characterized by skyrmion twisting during branching events and localized skyrmion filament structures cupped by $S^{\pm}$ (anti)monopoles. Our SANS tomography techniques provide unique insights into skyrmion formation/annihilation and transition processes through (anti)monopole defects, opening the door to future studies of bulk micromagnetic materials on unprecedented lengthscales, including skyrmion and emergent (anti)monopole structure, behaviour, and dynamic processes under a wide range of external parameters under complex environments. Furthermore, this techniques may be extended to incorporate new micromagnetic systems, such as frustrated magnets and superconducting vortex lattices, in addition to exotic topological structures such as magnetic chiral bobbers [80], torons [118, 109, 125], bimerons [256], and hopfions [82].

Chapter 6

Experimental Realization of Neutron Helical Waves

The study presented in this chapter is reproduced and adapted from [255].

Whereas conventional neutron probes exploit the nuclear and magnetic moments of the neutron to study the structural and magnetic properties of materials, the OAM degree of freedom of the neutron promises direct access to topological phases, structures, and interactions over a wide range of systems. Endowing the wavefront of the neutron with OAM embeds the sample-to-system interaction in a topological subspace, enabling novel investigations of topological scattering interactions and interferences across various phases of matter and system potentials. Through topological interaction mechanisms such as targeted scattering, conservation of topological charge, and dynamic OAM transfer mechanisms, we would gain unprecedented insights into topological features and excitations spanning condensed matter systems to fundamental physics and quantum sensing applications, ushering in a new phase of neutron probing techniques.

Section 2.1.2 introduced the concept of neutron OAM, its future applications, and the various means by which it has been generated and detected. One of the foremost challenges facing the utilization of neutron OAM degrees of freedom across modern neutron scattering and imaging techniques is the inability to create helical wavefronts dominated by a single OAM value. Future applications involving the determination of sample defect densities, magnetic topological charges, and exotic topological interactions/phases are predicated on the input of a known single-valued neutron OAM. Moreover, implementation with quantum materials necessitates the generation of topological neutron states on the length-scale of the periodicity of the topological structures in the sample. However, existing methods as outlined in section 2.1.2 are limited to either incoherent averaged values or lattice structures with large periodicities unable to match those found in quantum materials. As a result, neutron OAM prospects for quantum materials and sensing applications remain unrealized.

In this chapter, we demonstrate a holographic approach to the selective tuning of neutron OAM. We use microfabricated arrays of millions of diffraction gratings with critical dimensions comparable to neutron coherence lengths. The arrays can be laid out on the cm-square areas typical of usual neutron scattering targets, inspiring the direct integration of other structured wave techniques, such as the generation of Airy and Bessel beams [257, 258, 259], into neutron sciences. Furthermore, we discuss the applications towards characterization of materials, helical neutron interactions, and spin-orbit correlations.

6.1 Generation of Neutron Helical Beams Through Phase-Gratings

Phase-gratings with q-fold fork dislocations are a standard tool in optics that produce photons with OAM value of $\ell = m\hbar q$ at the mth order of diffraction [260]. This requires that the transverse coherence length of the light beam be at least comparable to the dimensions of the fork dislocation.

Neutron beams have transverse coherence lengths of microns and fluence rates of $10^5 - 10^7$ neutrons/(cm^2×s). Observing the neutron signal from a single micron sized target is impractical. However, we can multiply the signal by using an $N \times N$ array of micron-sized fork dislocation gratings. When considering an array it is important that the overall array size is much smaller than the diffraction signal of interest, and that the separation distance between the individual gratings is large enough so that it does not induce an observable diffraction order.

We have fabricated such arrays with $N = 2500$ on silicon substrates using electron beam lithography. Fig. 6.1a shows scanning electron microscope (SEM) images of the fork dislocation phase-gratings with $q = 3$. By construction, the spatial dimensions of the individual gratings are comparable to the transverse coherence length of our neutron beam. The use of such an array increases the neutron intensity by N^2 in a given $m > 0$ diffraction order in the far-field (see Fig. 6.1b). The individual diffraction orders in the presented intensity profiles (see Fig. 6.1c) span an area of $\approx$ 10 cm by 10 cm, were taken over a

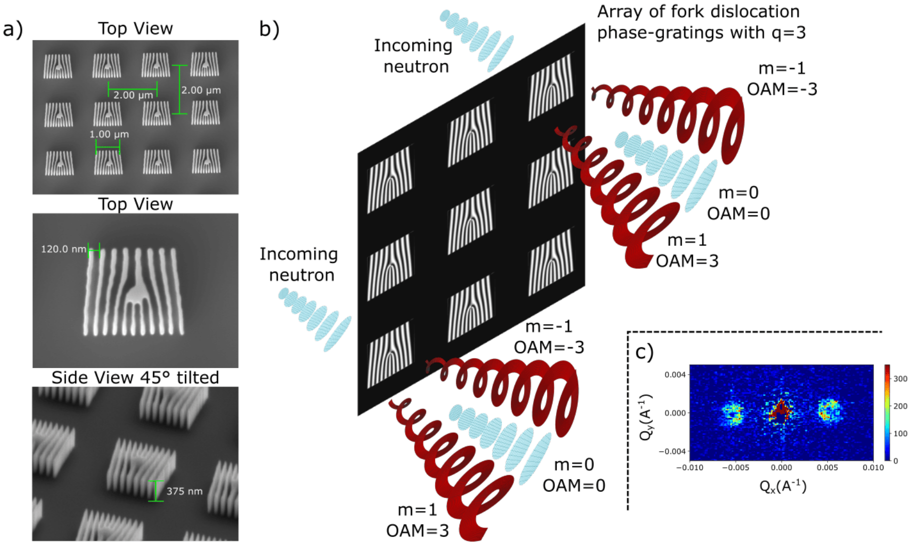

Figure 6.1: Holographic approach to generating neutron helical wavefronts that carry well-defined orbital angular momentum (OAM). a) SEM images characterizing the array of fork dislocation phase-gratings used to generate the neutron helical wavefronts. The arrays covered a 0.5 cm by 0.5 cm area and consisted of 6,250,000 individual 1 μm by 1 μm fork dislocation phase-gratings that possesses a period of 120 nm, height 500 nm, and were separated by 1 μm on each sides. Three arrays with topological charges of q=0 (standard grating profile), 3 (shown here), and 7 were used in the experiment. b) Each phase-grating generates a diffraction spectra consisting of diffraction orders (m) that carry a well-defined OAM value of $\ell = m\hbar q$. c) The intensity in the far-field is the sum over the signal from all of the individual fork dislocation phase-gratings. Shown is an example of the collected SANS data. Reprinted from [255].

period of ≈ 40 min, and consist of the signal from $6,250,000$ individual fork dislocation phase-gratings.

To characterize the generated OAM states we can map out the momentum distribution. SANS beamlines provide several advantages as they map the spatial profiles in the far-field, where the observed intensity distribution is directly determined by the Fourier transform of the outgoing neutron wavefunction. Having access to the far-field enables the use of holographic techniques that have been developed for optical structured waves [260]. Another advantage is the relatively large flux and the accessibility to a wide range of wavelengths. And lastly, it is the typical setup used in material characterization techniques including the contemporary techniques analyzing skyrmion and topological geometries [224, 113].

Straight-forward extensions follow for incorporating the characterization of materials and performing experiments with helical neutron interactions.

Small angle neutron scattering measurements were performed on the GP-SANS beamline at the High Flux Isotope Reactor at Oak Ridge National Laboratory [261]. The arrays of fork dislocation phase-gratings were placed inside a rotation mount which was then affixed to the end of the sample aperture holder. The phase-gratings were placed 17.8 m away from a 20 mm diameter source aperture. A 4 mm diameter sample aperture was placed right in front of the sample. The distance from the phase-grating to the camera was 19 m, and the camera size spanned an area of ≈ 1 m^2 with each pixel being $\approx$ 5.5 mm by 4.1 mm in size. The wavelength distribution was triangular with $\Delta\lambda/\lambda$ $\approx$0.13 and a central wavelength of 12 Å. The resulting beam divergence is $\approx$ 0.67 mrad, the transverse coherence of the neutron wavepacket $\sigma_\perp \approx \lambda L_1/s \approx 1$ μm, and the standard deviation of the resolution distribution was estimated to be σ_Q=0.00016 Å^{-1}.

The neutron wavelength is selected by a turbine-like velocity selector that has helical blades which allow specified neutrons with correct velocity (and thus wavelength) through it. The $\Delta\lambda/\lambda$ is determined by the angle at which the velocity selector is positioned with respect to the beam. Note that because the wavelengths were selected with a velocity selector we do not get $\lambda/2$ and $\lambda/4$ contributions that are present when a monochromator is used.

Scattering images were collected for the three arrays of fork dislocation phase-gratings in the beam, where the instrument configuration remained fixed. An empty beam scan without a sample and a background scan for a plain Si wafer of equivalent size and thickness were collected. These measurements were used to take into account the beam size, total neutron monitor counts, background and plain wafer scattering, and sample/plain wafer transmission which would otherwise contribute to losses in intensity and increased background scattering noise levels in the images.

A simple map for modelling the action of a binary phase-grating with a fork dislocation can be expressed as:

$$\psi_{\text{in}} \rightarrow \psi_{\text{in}} \left[\cos\left(\frac{\alpha}{2}\right) + \sin\left(\frac{\alpha}{2}\right) \sum_m \frac{2}{m\pi} e^{i\frac{2\pi m x}{p}} e^{imq\phi} \right] \tag{6.1}$$

where x (ϕ) is the Cartesian (azimuthal) coordinate, p is the grating period, $m = ... - 3, -1, 1, 3...$ are the non-zero diffraction orders, α is the induced phase by the height of the grating grooves, and the incoming wavefunction ψ_{in} is typically taken to be a Gaussian profile for convenience. The far-field is typically defined to be the distance at which Fraunhofer diffraction is valid. In this regime the diffraction orders are spatially separated, so here we can consider the m terms independently along their respective propagation directions. We thus obtain well-defined OAM states in the form of $\psi_{\text{in}}e^{imq\phi}$. Note that the OAM is therefore only well defined in the paraxial approximation. The full analysis of the evolution of such states is presented in Ref. [262, 263].

With equal transverse coherence lengths $\sigma_x = \sigma_y = \sigma_\perp$ we can make use of the cylindrical symmetry to describe the transverse wave function in terms of solutions to the 2-D harmonic oscillator [160]:

$$\psi_{\ell,n_r}(r,\phi) = \mathcal{N}\left(\frac{r}{\sigma_\perp}\right)^{|\ell|} e^{-\frac{r^2}{2\sigma_\perp^2}} \mathcal{L}_{n_r}^{|\ell|}\left(\frac{r^2}{\sigma_\perp^2}\right) e^{i\ell\phi}, \tag{6.2}$$

where $\mathcal{N} = \frac{1}{\sigma_\perp}\sqrt{\frac{n_r!}{\pi(n_r+|\ell|)!}}$ is the normalization constant, $n_r \in (0,1,2...)$, $\ell \in (0,\pm1,\pm2...)$, and $\mathcal{L}_{n_r}^{|\ell|}(r^2/\sigma_\perp^2)$ are the associated Laguerre polynomials. The corresponding neutron energy is

$$E = \hbar\omega_\perp(2n_r + |\ell| + 1), \tag{6.3}$$

where $\omega_\perp^2 = \hbar/(2M\sigma_\perp^2)$, and M is the mass of the neutron. Each diffraction order m of the fork dislocation phase-grating is in a definite state of OAM:

$$\psi = \sum_{n_r} \psi_{\ell=mq,n_r}. \tag{6.4}$$

Considering $n_r = 0$ dominant term [160] of the first diffraction order, we can determine that the azimuthally integrated intensity:

$$\int_0^{2\pi} |\psi_{q,0}(r_0,\phi_0)|^2 d\phi \tag{6.5}$$

peaks at:

$$r_0 = \sigma_\perp\sqrt{q}. \tag{6.6}$$

6.2 Results

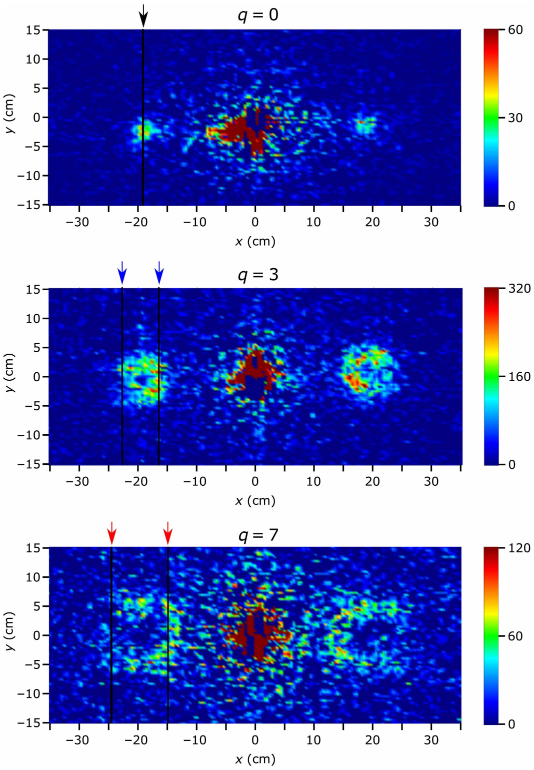

Figure 6.2: SANS data collected for the three arrays of fork dislocation phase-gratings with q=0 (top), q=3 (middle), and q=7 (bottom). The m= $-1, 0, 1$ diffraction orders are visible, and the corresponding doughnut profiles induced by the helical wavefronts (see Fig. 6.1b) can be observed in the bottom two profiles. Due to the relatively high intensity of the direct beam the range of the colorbar is limited to emphasize the diffraction order features. The vertical gridlines and the arrows above the plots indicate the location of the theoretical intensity peaks of the m= -1 orders. The azimuthally integrated intensity profiles across the diffraction orders, as well as the corresponding simulated profiles, are shown in Fig. 6.3. Reprinted from [255].

We fabricated three arrays of fork dislocation phase-gratings on Si wafers, with topological charge of q=0, 3, and 7. Each array covered a 0.5 cm by 0.5 cm area and consisted of $6,250,000$ individual 1 μm by 1 μm fork dislocation phase-gratings, where each one possessed a period of 120 nm, height 500 nm, and was separated by 1 μm on each side from the other fork dislocation phase-gratings.

The observed SANS data for the arrays of fork dislocation phase-gratings is shown in Fig. 6.2. The measurement time was 60 min for q=0, 40 min for q=3, and 60 min for q=7. With the phase-grating period of $p = 120$ nm, the angle of divergence of the first diffraction order is $\theta \approx \lambda/p \approx 0.01$ rad which corresponds to $Q_x = 2\pi/p = 0.00525$ $\mathring{A}^{-1}$ on the SANS images (see Fig 6.1c). In our particular setup this corresponds to a spatial distance of $x \approx 19$ cm on the camera as shown in Fig. 6.2. Good agreement is found with the observed location of the peaks.

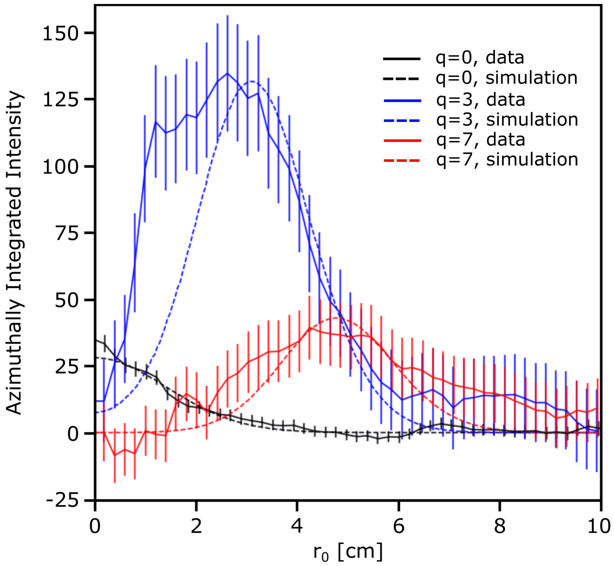

Figure 6.3: The azimuthally integrated intensity profiles centered on the $m = -1$ diffraction orders of the data presented in Fig. 6.2. The simulated profiles take into account the wavelength distribution, beam divergence, propagation distance, and array size which are common to all three cases. The amplitude in each case was scaled to match the observed data. Note that for the q=0 data, a large magnet apparatus was present in the beamline which greatly reduced the observed intensity. Good agreement is found between the simulated and observed profiles. Reprinted from [255].

To quantify the doughnut profiles we can analyze the azimuthally integrated intensity (Eq. 6.5) centered on the first diffraction orders. Fig. 6.3 shows the comparison between observed and simulated intensity. For the simulated profiles only the amplitude was varied in each case to match the observed amplitude. Wavelength distribution, beam divergence, propagation distance, and array size are common to all three profiles. Note that because each wavelength has a distinct diffraction angle, the observed signal at the first diffraction orders is the incoherent sum of the translated signals from each wavelength. For the q=0 data, a large magnet apparatus was present in the beamline which greatly reduced the observed intensity and therefore the peak appears relatively smaller than expected. Good agreement is observed between the simulated and observed profiles.

6.3 Conclusions

Through microfabrication and SANS techniques, we have successfully produced and characterized topological diffraction gratings which generate neutron helical waves that are dominated by a well-defined OAM value. Using microfabricated 2D arrays of fork dislocation phase-gratings, we have revealed the doughnut shaped intensity SANS signature of various topological neutron states, thus providing the first experimental realization of single-valued coherent neutron OAM states. This method enables novel investigations of the coherent interaction between neutron OAM and topological phases of matter through targeted and enhanced scattering/interferences, conservation of OAM/topological charge, and a dynamic OAM-magnon transfer. For example, through the implementation of a topological grating upstream of a magnetic skyrmion sample, we could couple the topological spatial phase structure of the neutron beam with the topological spin phase structure of the skyrmion lattice, exploring the coherent diffraction of neutron OAM states from a triangular skyrmion lattice phase. A successful demonstration of the passage and/or transfer of neutron OAM to skyrmions would serve as a novel and direct means of probing sample topologies, conservation of OAM, and provide estimates on topological defect densities and structural correlation lengths, having extensive implications for neutron scattering techniques for bulk topological phases. These results would have far-reaching implications for neutron scattering techniques as a whole, providing insight into topological interactions between neutrons and materials, ushering in a new phase of neutron materials scattering techniques.

A myriad of applications which extend beyond quantum materials, involve fundamental tests of topological based interactions and novel neutron beam manipulation techniques. In particular, topological absorption/decay mechanisms and interaction potentials may be explored using the presented neutron helical wave generation technique, with studies ranging from spin-dependent neutron OAM selection rules in nuclear spin-polarized ^{3}He, to OAM-dependent neutron lifetimes. Moreover, the microfabrication methods presented here may be extended to various shapes of phase-gratings such as cubic phase and radial phase gradients, enabling the production of "self-accelerating" Airy beams [258, 264], as well as the "non-diffractive" Bessel beams [259, 265]. This would offer new routes to manipulating neutron beam shapes and trajectories, opening the door to a new suite of structured neutron beam techniques.

Finally, these structured techniques may be extended to other quantum materials characterization methods by incorporating OAM degrees of freedom across a variety of probe particles, spanning electrons to X-rays. In particular, developing OAM-based analyzers and structuring input probing beams with helical wavefronts, and spin-orbit modes of various symmetries and topologies, would enable the direct investigation of novel topological features and excitations. Implementation of these methods across Angle-Resolved Photoemission Spectroscopy(ARPES) and neutron spectroscopic instruments for example, would enable the direct examination of topological interactions and excitations in quantum materials which span a diverse range of lengthscales, dimensions, and degrees of freedom, encompassing energy to spin. These experiments promise a new generation of quantum measurement techniques which provide unprecedented access to exotic topological phases and interactions in quamtum materials.

Chapter 7

Conclusions and Future Prospects

In this thesis, we (1) demonstrated novel techniques for probing three-dimensional topological magnetic states in bulk quantum materials, and (2) applied these methods to characterize the topological dynamics and stabilization defect pathways of the disordered multi-phase bulk skyrmion material, $Co_8Zn_8Mn_4$. Neutron scattering is an invaluable tool in the study of quantum materials, however, current techniques and their instrumentation fail to exploit all the available degrees of freedom of the neutron that we have at our disposal. In particular, tomographic approaches have yet to be adopted to modern SANS techniques; as a result, valuable information regarding the sensitivity of the neutron to three-dimensional sample states is completely discarded. Additionally, spin-phase coupled neutron interactions and topological degrees of freedom have yet to be explored, leaving a blatant gap in the repertoire for neutron scattering methods for quantum material investigations. Our work resolves these outstanding challenges, providing both the first demonstration of a three-dimensional reconstruction technique for the visualization of bulk micromagnetic materials and the first method for generating tunable single-valued topological neutron states.

The synthesis and characterization procedure for a disordered multi-phase bulk skyrmion sample, $Co_8Zn_8Mn_4$, was outlined in chapter 3. Powder and backscatter Laue X-ray diffraction techniques were used to characterize the phase purity and crystallinity of the sample, respectively. Magnetometry and SANS measurements were performed to identify the thermal equilibrium temperature-magnetic field skyrmion envelope. SANS measurements of the thermal equilibrium triangular lattice phase revealed a uniform scattering ring characteristic of a rotationally disordered magnetic configuration composed of chiral and skyrmion domains. Application of a skyrmion ordering sequence precipitated oriented and ordered triangular lattices which manifest a hexagonal pattern in SANS.

Ordering methods demonstrated in chapter 3 were used to examine the disorder-dependent nature of skyrmion transitions and dynamics across thermal and metastable phases in chapter 4. Application of skyrmion ordering procedures in the thermal equilibrium phase revealed an indirect conversion between the disordered ring intensity and the ordered skyrmion peak intensity, indicative of the presence of an initial jammed state of chiral domains. Cooling from the disordered thermal equilibrium skyrmion triangular lattice phase to the metastable skyrmion square lattice phase revealed a new disordered-to-ordered skyrmion square lattice transition pathway characterized by the novel promotion of four-fold order in SANS and accompanied by a change in topology of the system, reinforced through micromagnetic simulations. Here, anisotropy is thought to facilitate the disentangling of a jammed labyrinth state through pathways which alter the topological charge of the system, allowing reorientations to a square lattice. In the ordered metastable triangular lattice phase, field-induced saturation protocols to and from the ferromagnetic phase reveal a skyrmion memory effect which is enhanced upon application of a skyrmion ordering sequence. The dynamical response of the memory state to the ordering sequence suggests that skyrmion survival during saturation is encoded into topological charge conserving magnetic torons which are pinned to defect sites. The subsequent interplay of the anisotropy and field direction during the ordering sequence may facilitate the elongation of torons into skyrmions. Together, these results highlight the role of skyrmion disorder and topological charge in skyrmion stabilization and lattice restructuring pathways, offering new routes for skyrmion manipulation and enhanced stability for spintronic applications.

Application of the SANS tomography technique to a bulk skyrmion material (chapter 5) yielded the first three-dimensional visualizations of a bulk skyrmion lattice and its stabilization through branching and segmentation topological transition emergent (anti)monopoles defect pathways. These visualizations have provided key insights into skyrmion formation and annihilation mechanisms through the identification of defect-mediated transition points and possible field-saturated skyrmion fragments, in addition to their dynamical twisting behaviors. In this manner, we have overcome the previous sample thickness and shape requirements associated with x-ray and electron probes, which limit studies to thin and confined sample geometries only capable of reconstructing a handful of skyrmions over a few periods of depth. Moreover, our method enables bulk studies across a broad range of material compositions and states under extreme and diverse external parameters, thanks to the generous sample spaces afforded by SANS beamlines which may accommodate both complex and large-scale sample environments. Future studies involve the tomographic exploration of various skyrmion formation and annihilation phenomena as a function of field, temperature, and skyrmion order, mapping out the entire magnetic phase space of the material. Alternatively, three-dimensional oscillatory skyrmion dynamics on the millisecond and sub-millisecond scale can be explored via the incorporation of Time-Resolved SANS measurements to the multi-projection SANS datasets. Application of the tomography technique to skyrmion systems during various dynamical processes such as current-induced creation, nonlinear phenomena, and short-term memory effects, may guide the future development of skyrmion-based neuromorphic computing [266, 267]. The tomography algorithm may be expanded to handle a broader class of micromagnetic systems, such as frustrated magnets and vortex lattice superconductors, whilst also extending the search for exotic topological structures to new magnetic systems [268, 81]. Furthermore, the tomography algorithm could also be adapted to neutron grating interferometry setups, enabling phase tomography studies up to micrometer lengthscales. Finally, computational advancements may be made by implementing machine-learning methods using phantom training datasets or by incorporating quantum annealing approaches to the minimization portion of the algorithm.

The experimental generation and characterization of neutron helical waves dominated by tunable single-valued topological charges, as outlined in chapter 6, serves as a critical first step as to the incorporation of structured neutron beams techniques in SANS methods and the further advancement of neutron scattering techniques for quantum material applications. The successful microfabrication of neutron diffraction phase-gratings with periodicities accessible by SANS heralds a generation of a variety of structured neutron beams spanning Airy beams, using cubic phase gratings, to spin-orbit beams, through magnetic analogues of the fork-dislocation phase-gratings, and combinations thereof. The nontrivial propagation properties of these beams offer new routes to manipulating neutron beam shapes and trajectories which can be applied to prepare exotic and robust neutron states for tests of exotic interactions, fundamental physics, and quantum materials.

Neutron helical waves hold special promise for the direct characterization of topological magnetic states in bulk materials [269]. In particular, the fork-dislocation phase-gratings may be fabricated with periodicities and topological charges matching those found in bulk skyrmion materials. Preparation of these states upstream of a skyrmion sample in a SANS experiment would then enable the coherent diffraction of topological neutron states phase-matched to the topological sample states. This setup would effectively embed the scattering in a topological subspace, producing topological interferences from which we could derive structural topological information on the sample, such as the topological charge, defect densities, and correlation lengths of the topological features, based on enhanced scattering intensities, addition of OAM, and OAM dephasing. Angular characteristics of the coherent scattering interaction between neutron OAM and bulk magnetic topological structures may also be explored by performing SANS measurements as the topological diffraction gratings are rotated upstream of a sample. These beam preparation methods may additionally be extended to dynamic neutron scattering techniques to explore exotic interactions between topological neutron state and topological magnetic sample states, coupling to excitations in condensed matter, potentially through OAM-magnon modes. Moreover, neutron OAM states may be incorporated to interferometric [170, 270, 271, 272, 273, 274, 194, 275], polarized [197, 276, 277, 278], and entangled neutron methods [279, 280, 281, 282], enabling the search for exotic topological phases, magnetic correlations, and interactions. For instance, similar fork dislocation gratings could be used to generate a topological neutron interferometer which measures topological phase shifts through azimuthal rotations of fringe patterns or changes in their topological orders; magnetic analogues of the gratings and transverse neutron polarimetry approaches could serve as a novel route to examining spin-dependant OAM correlations and interactions in quantum materials, such as OAM induced rotations of skyrmion lattices; OAM entangled neutron beams could uncover unique scattering signatures and properties of topological and frustrated systems. Finally, neutron OAM states may be used in a SANS tomography approach, examining the topological interference of neutron and sample states as a function of sample rotation. This procedure would enable the determination of the volume fraction, orientation, and topological charges of topological features in samples, effectively mapping the three-dimensional topology of a sample for the first time. These structured beam methods may be incorporated into the input probe beams and analyzers of additional sample characterization techniques which transcend those of neutrons, such as Angle-Resolved Photoemission Spectroscopy (ARPES), bridging real space and momentum space topologies. Together, these experiments promise a new generation of neutron scattering techniques with unrivalled control over neutron beams, providing access to exotic interactions over a range of lengthscales and topologies.

The quantum measurement techniques presented here reveal an unaddressed regime of physics which reimagines current skyrmion spintronic architectures. Novel access to the third dimension and topological features of bulk quantum materials enables the unprecedented study of skyrmion formation, interactions, defect pathways, and drive dynamics across a range of systems and parameters. This collection of phenomena offers new routes for skyrmion stabilization, control, and manipulation which may fundamentally reshape our approaches to the engineering of spintronic devices and quantum computation frameworks. In particular, three-dimensional investigations may establish innovative methods for the controlled directional transport of skyrmions and may lead to devices which employ hybridized skyrmion systems, consisting of both smooth and singular magnetic textures, using disorder as a tunable control parameter; nonaxisymmetric skyrmions, with tubes perpendicular to the external field [283, 284, 84]; or entirely new topological quasiparticles as logical bits and qubits [285, 82, 286, 80, 287, 52, 288]. Moreover, the topological stability and additional degrees of freedom of three-dimensional skyrmion systems may be exploited in quantum computation schemes. Here, skyrmions are intrinsically quantum-error corrected logical qubits, acting as their own decoherent free subspace for logic operations, similar to those demonstrated with neutron interferometry [289]. Three-dimensional skyrmion twisting [94, 97] and braiding phenomena [81] may also be exploited, enabling three-dimensional quantum computation schemes [290, 291, 292]. Topological probes may lead to exotic conceptualizations involving higher-order topology skyrmion structures [293, 294, 295, 296] and superstructures [81, 87, 37]. These new device architectures may operate on new dynamical modes such as skyrmion string rotation, dilation, and propagation in confined channels [297, 298, 299], while employing novel readout methods such as OAM-magnon coupled excitations. Ultimately, these experiments open the door to the unique functionalities of three-dimensional skyrmions, offering new symmetries, degrees of freedom, and dynamical control methods which inspire a new era in quantum materials characterization and engineering, reshaping modern skyrmion spintronics and quantum information technologies.

References

[1] B Keimer and JE Moore. The physics of quantum materials. *Nature Physics*, 13(11):1045–1055, 2017.

[2] Yoshinori Tokura, Masashi Kawasaki, and Naoto Nagaosa. Emergent functions of quantum materials. *Nature Physics*, 13(11):1056–1068, 2017.

[3] Bahadur Singh, Hsin Lin, and Arun Bansil. Topology and symmetry in quantum materials. *Advanced Materials*, page 2201058, 2022.

[4] Yoshinori Tokura. Quantum materials at the crossroads of strong correlation and topology. *Nature Materials*, 21(9):971–973, 2022.

[5] Jing Wang and Shou-Cheng Zhang. Topological states of condensed matter. *Nature Materials*, 16(11):1062–1067, 2017.

[6] Mucio A Continentino. Topological phase transitions. *Physica B: Condensed Matter*, 505:A1–A2, 2017.

[7] Ching-Kai Chiu, Jeffrey CY Teo, Andreas P Schnyder, and Shinsei Ryu. Classification of topological quantum matter with symmetries. *Reviews of Modern Physics*, 88(3):035005, 2016.

[8] K v Klitzing, Gerhard Dorda, and Michael Pepper. New method for high-accuracy determination of the fine-structure constant based on quantized hall resistance. *Physical Review Letters*, 45(6):494, 1980.

[9] Klaus von Klitzing, Tapash Chakraborty, Philip Kim, Vidya Madhavan, Xi Dai, James McIver, Yoshinori Tokura, Lucile Savary, Daria Smirnova, Ana Maria Rey, et al. 40 years of the quantum hall effect. *Nature Reviews Physics*, 2(8):397–401, 2020.

[10] R. E. Prange, S. M. Girvin, and K. V. Klitzing. *The quantum Hall effect*. Springer, 1989.

[11] AH MacDonald and P Středa. Quantized hall effect and edge currents. *Physical review B*, 29(4):1616, 1984.

[12] David J Thouless, Mahito Kohmoto, M Peter Nightingale, and Marcel den Nijs. Quantized hall conductance in a two-dimensional periodic potential. *Physical Review Letters*, 49(6):405, 1982.

[13] Yasuhiro Hatsugai. Chern number and edge states in the integer quantum hall effect. *Physical Review Letters*, 71(22):3697, 1993.

[14] Qian Niu, Ds J Thouless, and Yong-Shi Wu. Quantized hall conductance as a topological invariant. *Physical review B*, 31(6):3372, 1985.

[15] Joseph E Avron, Daniel Osadchy, and Ruedi Seiler. A topological look at the quantum hall effect. *Physics today*, 56(8):38–42, 2003.

[16] Mahito Kohmoto. Topological invariant and the quantization of the hall conductance. *Annals of Physics*, 160(2):343–354, 1985.

[17] Xiao-Gang Wen. Colloquium: Zoo of quantum-topological phases of matter. *Reviews of Modern Physics*, 89(4):041004, 2017.

[18] F Duncan M Haldane. Nobel lecture: Topological quantum matter. *Reviews of Modern Physics*, 89(4):040502, 2017.

[19] Jeffrey CY Teo and Taylor L Hughes. Topological defects in symmetry-protected topological phases. *Annual Review of Condensed Matter Physics*, 8:211–237, 2017.

[20] Urs Gasser, Christoph Eisenmann, Georg Maret, and Peter Keim. Melting of crystals in two dimensions. *ChemPhysChem*, 11(5):963–970, 2010.

[21] Tony Hilton Royle Skyrme. A non-linear field theory. *Proceedings of the Royal Society of London. Series A. Mathematical and Physical Sciences*, 260(1300):127–138, 1961.

[22] M Zahid Hasan and Charles L Kane. Colloquium: topological insulators. *Reviews of Modern Physics*, 82(4):3045, 2010.

[23] Xiao-Liang Qi and Shou-Cheng Zhang. Topological insulators and superconductors. *Reviews of Modern Physics*, 83(4):1057, 2011.

[24] Yoshinori Tokura, Kenji Yasuda, and Atsushi Tsukazaki. Magnetic topological insulators. *Nature Reviews Physics*, 1(2):126–143, 2019.

[25] Tiantian Zhang, Yi Jiang, Zhida Song, He Huang, Yuqing He, Zhong Fang, Hongming Weng, and Chen Fang. Catalogue of topological electronic materials. *Nature*, 566(7745):475–479, 2019.

[26] AA Burkov. Topological semimetals. *Nature Materials*, 15(11):1145–1148, 2016.

[27] Masatoshi Sato and Yoichi Ando. Topological superconductors: a review. *Reports on Progress in Physics*, 80(7):076501, 2017.

[28] Sergey S Pershoguba, Sho Nakosai, and Alexander V Balatsky. Skyrmion-induced bound states in a superconductor. *Physical review B*, 94(6):064513, 2016.

[29] Shubhayu Chatterjee, Matteo Ippoliti, and Michael P Zaletel. Skyrmion superconductivity: Dmrg evidence for a topological route to superconductivity. *Physical review B*, 106(3):035421, 2022.

[30] Tarun Grover and T Senthil. Topological spin hall states, charged skyrmions, and superconductivity in two dimensions. *Physical Review Letters*, 100(15):156804, 2008.

[31] Stefano Donati, Lorenzo Dominici, Galbadrakh Dagvadorj, Dario Ballarini, Milena De Giorgi, Alberto Bramati, Giuseppe Gigli, Yuri G Rubo, Marzena Hanna Szymańska, and Daniele Sanvitto. Twist of generalized skyrmions and spin vortices in a polariton superfluid. *Proceedings of the National Academy of Sciences*, 113(52):14926–14931, 2016.

[32] Yusuke Ishihara, Takeshi Mizushima, Atsushi Tsuruta, and Satoshi Fujimoto. Torsional chiral magnetic effect due to skyrmion textures in a weyl superfluid He 3- A. *Physical review B*, 99(2):024513, 2019.

[33] LS Leslie, A Hansen, KC Wright, BM Deutsch, and NP Bigelow. Creation and detection of skyrmions in a Bose-Einstein condensate. *Physical Review Letters*, 103(25):250401, 2009.

[34] Usama Al Khawaja and Henk Stoof. Skyrmions in a ferromagnetic Bose–Einstein condensate. *Nature*, 411(6840):918–920, 2001.

[35] Jun-ichi Fukuda and Slobodan Žumer. Quasi-two-dimensional skyrmion lattices in a chiral nematic liquid crystal. *Nature Communications*, 2(1):246, 2011.

[36] Andriy Nych, Jun-ichi Fukuda, Uliana Ognysta, Slobodan Žumer, and Igor Muševič. Spontaneous formation and dynamics of half-skyrmions in a chiral liquid-crystal film. *Nature Physics*, 13(12):1215–1220, 2017.

[37] David Foster, Charles Kind, Paul J Ackerman, Jung-Shen B Tai, Mark R Dennis, and Ivan I Smalyukh. Two-dimensional skyrmion bags in liquid crystals and ferromagnets. *Nature Physics*, 15(7):655–659, 2019.

[38] Yoshinori Tokura and Naoya Kanazawa. Magnetic skyrmion materials. *Chemical Reviews*, 121(5):2857–2897, 2020.

[39] Roland Wiesendanger. Nanoscale magnetic skyrmions in metallic films and multilayers: a new twist for spintronics. *Nat. Rev. Mater.*, 1(7):16044, 2016.

[40] Naoto Nagaosa and Yoshinori Tokura. Topological properties and dynamics of magnetic skyrmions. *Nature Nanotechnology*, 8(12):899–911, 2013.

[41] SL Zhang, G Van Der Laan, and T Hesjedal. Direct experimental determination of the topological winding number of skyrmions in Cu_2OSeO_3. *Nature Communications*, 8(1):14619, 2017.

[42] A. Neubauer, C. Pfleiderer, B. Binz, A. Rosch, R. Ritz, P. G. Niklowitz, and P. Böni. Topological hall effect in the A phase of MnSi. *Physical Review Letters*, 102(18):186602, 2009.

[43] S. Seki, X. Z. Yu, S. Ishiwata, and Y. Tokura. Observation of skyrmions in a multiferroic material. *Science*, 336(6078):198, 2012.

[44] T. Schulz, R. Ritz, A. Bauer, M. Halder, M. Wagner, C. Franz, C. Pfleiderer, K. Everschor, M. Garst, and A. Rosch. Emergent electrodynamics of skyrmions in a chiral magnet. *Nature Physics*, 8(4):301–304, 2012.

[45] JS White, I Živković, AJ Kruchkov, M Bartkowiak, A Magrez, and HM Rønnow. Electric-field-driven topological phase switching and skyrmion-lattice metastability in magnetoelectric Cu_2OSeO_3. *Physical Review Applied*, 10(1):014021, 2018.

[46] JS White, K Prša, P Huang, AA Omrani, I Živković, M Bartkowiak, H Berger, A Magrez, JL Gavilano, G Nagy, et al. Electric-field-induced skyrmion distortion and giant lattice rotation in the magnetoelectric insulator Cu_2OSeO_3. *Physical Review Letters*, 113(10):107203, 2014.

[47] Nan Tang, WLNC Liyanage, Sergio A Montoya, Sheena Patel, Lizabeth J Quigley, Alexander J Grutter, Michael R Fitzsimmons, Sunil Sinha, Julie A Borchers, Eric E Fullerton, et al. Skyrmion-excited spin wave fractal network. *Advanced Materials*, page 2300416, 2023.

[48] Wang Kang, Yangqi Huang, Xichao Zhang, Yan Zhou, and Weisheng Zhao. Skyrmion-electronics: An overview and outlook. *Proceedings of the IEEE*, 104(10):2040–2061, 2016.

[49] Huixia Luo, Peifeng Yu, Guowei Li, and Kai Yan. Topological quantum materials for energy conversion and storage. *Nature Reviews Physics*, 4(9):611–624, 2022.

[50] Albert Fert, Nicolas Reyren, and Vincent Cros. Magnetic skyrmions: advances in physics and potential applications. *Nature Review Materials*, 2(7):17031, 2017.

[51] Xichao Zhang, Yan Zhou, Kyung Mee Song, Tae-Eon Park, Jing Xia, Motohiko Ezawa, Xiaoxi Liu, Weisheng Zhao, Guoping Zhao, and Seonghoon Woo. Skyrmion-electronics: writing, deleting, reading and processing magnetic skyrmions toward spintronic applications. *Journal of Physics: Condensed Matter*, 32(14):143001, 2020.

[52] Christina Psaroudaki and Christos Panagopoulos. Skyrmion qubits: A new class of quantum logic elements based on nanoscale magnetization. *Physical Review Letters*, 127(6):067201, 2021.

[53] Xichao Zhang, Motohiko Ezawa, and Yan Zhou. Magnetic skyrmion logic gates: conversion, duplication and merging of skyrmions. *Sci. Rep.*, 5(1):9400, 2015.

[54] Alexey A Kovalev and Shane Sandhoefner. Skyrmions and antiskyrmions in quasi-two-dimensional magnets. *Frontiers in Physics*, 6:98, 2018.

[55] Xiuzhen Yu. Magnetic imaging of various topological spin textures and their dynamics. *Journal of Magnetism and Magnetic Materials*, 539:168332, 2021.

[56] XZ Yu, W Koshibae, Y Tokunaga, K Shibata, Y Taguchi, N Nagaosa, and Y Tokura. Transformation between meron and skyrmion topological spin textures in a chiral magnet. *Nature*, 564(7734):95–98, 2018.

[57] XZ Yu, Y Tokunaga, Y Kaneko, WZ Zhang, K Kimoto, Y Matsui, Y Taguchi, and Y Tokura. Biskyrmion states and their current-driven motion in a layered manganite. *Nature Communications*, 5(1):3198, 2014.

[58] Shi-Zeng Lin, Avadh Saxena, and Cristian D Batista. Skyrmion fractionalization and merons in chiral magnets with easy-plane anisotropy. *Physical review B*, 91(22):224407, 2015.

[59] Peter Milde, Denny Köhler, Joachim Seidel, LM Eng, Andreas Bauer, Alfonso Chacon, Jonas Kindervater, Sebastian Mühlbauer, Christian Pfleiderer, Stefan Buhrandt, et al. Unwinding of a skyrmion lattice by magnetic monopoles. *Science*, 340(6136):1076–1080, 2013.

[60] Max T Birch, David Cortés-Ortuño, Nguyen D Khanh, Shinichiro Seki, Aleš Štefančič, Geetha Balakrishnan, Yoshinori Tokura, and Peter D Hatton. Topological defect-mediated skyrmion annihilation in three dimensions. *Communications Physics*, 4(1):175, 2021.

[61] Ulrich K Roessler, AN Bogdanov, and C Pfleiderer. Spontaneous skyrmion ground states in magnetic metals. *Nature*, 442(7104):797–801, 2006.

[62] Sebastian Mühlbauer, Benedikt Binz, F Jonietz, Christian Pfleiderer, Achim Rosch, Anja Neubauer, Robert Georgii, and Peter Böni. Skyrmion lattice in a chiral magnet. *Science*, 323(5916):915–919, 2009.

[63] C Pappas, E Lelievre-Berna, P Falus, PM Bentley, E Moskvin, S Grigoriev, P Fouquet, and B Farago. Chiral paramagnetic skyrmion-like phase in MnSi. *Physical Review Letters*, 102(19):197202, 2009.

[64] Dustin A Gilbert, Brian B Maranville, Andrew L Balk, Brian J Kirby, Peter Fischer, Daniel T Pierce, John Unguris, Julie A Borchers, and Kai Liu. Realization of ground-state artificial skyrmion lattices at room temperature. *Nature Communications*, 6(1):8462, 2015.

[65] Ryan D Desautels, Lisa DeBeer-Schmitt, Sergio A Montoya, Julie A Borchers, Soong-Geun Je, Nan Tang, Mi-Young Im, Michael R Fitzsimmons, Eric E Fullerton, and Dustin A Gilbert. Realization of ordered magnetic skyrmions in thin films at ambient conditions. *Physical Review Materials*, 3(10):104406, 2019.

[66] Rina Takagi, Naofumi Matsuyama, Victor Ukleev, Le Yu, Jonathan S White, Sonia Francoual, José RL Mardegan, Satoru Hayami, Hiraku Saito, Koji Kaneko, et al. Square and rhombic lattices of magnetic skyrmions in a centrosymmetric binary compound. *Nature Communications*, 13(1):1472, 2022.

[67] Satoru Hayami and Yukitoshi Motome. Square skyrmion crystal in centrosymmetric itinerant magnets. *Phys. Rev. B*, 103:024439, Jan 2021.

[68] Nguyen Duy Khanh, Taro Nakajima, Xiuzhen Yu, Shang Gao, Kiyou Shibata, Max Hirschberger, Yuichi Yamasaki, Hajime Sagayama, Hironori Nakao, Licong Peng, et al. Nanometric square skyrmion lattice in a centrosymmetric tetragonal magnet. *Nature Nanotechnology*, 15(6):444–449, 2020.

[69] MT Birch, D Cortés-Ortuño, LA Turnbull, MN Wilson, F Groß, N Träger, A Laurenson, N Bukin, SH Moody, M Weigand, et al. Real-space imaging of confined magnetic skyrmion tubes. *Nature Communications*, 11(1):1–8, 2020.

[70] Daniel Wolf, Sebastian Schneider, Ulrich K Rößler, András Kovács, Marcus Schmidt, Rafal E Dunin-Borkowski, Bernd Büchner, Bernd Rellinghaus, and Axel Lubk. Unveiling the three-dimensional magnetic texture of skyrmion tubes. *Nature Nanotechnology*, 17(3):250–255, 2022.

[71] M. Crisanti, M. T. Birch, M. N. Wilson, S. H. Moody, A. Štefančič, B. M. Huddart, S. Cabeza, G. Balakrishnan, P. D. Hatton, and R. Cubitt. Position-dependent stability and lifetime of the skyrmion state in nickel-substituted Cu_2OSeO_3. *Phys. Rev. B*, 102:224407, Dec 2020.

[72] T Reimann, A Bauer, C Pfleiderer, P Böni, P Trtik, A Tremsin, M Schulz, and S Mühlbauer. Neutron diffractive imaging of the skyrmion lattice nucleation in MnSi. *Physical review B*, 97(2):020406, 2018.

[73] Haifeng Du, Renchao Che, Lingyao Kong, Xuebing Zhao, Chiming Jin, Chao Wang, Jiyong Yang, Wei Ning, Runwei Li, Changqing Jin, et al. Edge-mediated skyrmion chain and its collective dynamics in a confined geometry. *Nature Communications*, 6(1):8504, 2015.

[74] Naoya Kanazawa, Shinichiro Seki, and Yoshinori Tokura. Noncentrosymmetric magnets hosting magnetic skyrmions. *Advanced Materials*, 29(25):1603227, 2017.

[75] Y Tokunaga, XZ Yu, JS White, Henrik M Rønnow, D Morikawa, Y Taguchi, and Y Tokura. A new class of chiral materials hosting magnetic skyrmions beyond room temperature. *Nature Communications*, 6(1):7638, 2015.

[76] XZ Yu, Yoshinori Onose, Naoya Kanazawa, Joung Hwan Park, JH Han, Yoshio Matsui, Naoto Nagaosa, and Yoshinori Tokura. Real-space observation of a two-dimensional skyrmion crystal. *Nature*, 465(7300):901–904, 2010.

[77] XZ Yu, Naoya Kanazawa, Yoshinori Onose, K Kimoto, WZ Zhang, Shintaro Ishiwata, Yoshio Matsui, and Yoshinori Tokura. Near room-temperature formation of a skyrmion crystal in thin-films of the helimagnet FeGe. *Nature Materials*, 10(2):106–109, 2011.

[78] Shanquan Chen, Shuai Yuan, Zhipeng Hou, Yunlong Tang, Jinping Zhang, Tao Wang, Kang Li, Weiwei Zhao, Xingjun Liu, Lang Chen, et al. Recent progress on topological structures in ferroic thin films and heterostructures. *Advanced Materials*, 33(6):2000857, 2021.

[79] Yuuki Yasui, Christopher J Butler, Nguyen Duy Khanh, Satoru Hayami, Takuya Nomoto, Tetsuo Hanaguri, Yukitoshi Motome, Ryotaro Arita, Taka-hisa Arima, Yoshinori Tokura, et al. Imaging the coupling between itinerant electrons and localised moments in the centrosymmetric skyrmion magnet $GdRu_2Si_2$. *Nature Communications*, 11(1):5925, 2020.

[80] Fengshan Zheng, Filipp N Rybakov, Aleksandr B Borisov, Dongsheng Song, Shasha Wang, Zi-An Li, Haifeng Du, Nikolai S Kiselev, Jan Caron, András Kovács, et al. Experimental observation of chiral magnetic bobbers in B20-type FeGe. *Nature Nanotechnology*, 13(6):451–455, 2018.

[81] Fengshan Zheng, Filipp N Rybakov, Nikolai S Kiselev, Dongsheng Song, András Kovács, Haifeng Du, Stefan Blügel, and Rafal E Dunin-Borkowski. Magnetic skyrmion braids. *Nature Communications*, 12(1):5316, 2021.

[82] Noah Kent, Neal Reynolds, David Raftrey, Ian TG Campbell, Selven Virasawmy, Scott Dhuey, Rajesh V Chopdekar, Aurelio Hierro-Rodriguez, Andrea Sorrentino, Eva Pereiro, et al. Creation and observation of hopfions in magnetic multilayer systems. *Nature Communications*, 12(1):1562, 2021.

[83] Shuang Li, Jing Xia, Laichuan Shen, Xichao Zhang, Motohiko Ezawa, and Yan Zhou. Mutual conversion between a magnetic Néel hopfion and a Néel toron. *Physical review B*, 105(17):174407, 2022.

[84] Hayley RO Sohn, Sergei M Vlasov, Valeriy M Uzdin, Andrey O Leonov, and Ivan I Smalyukh. Real-space observation of skyrmion clusters with mutually orthogonal skyrmion tubes. *Physical review B*, 100(10):104401, 2019.

[85] Shilei Zhang, Florian Kronast, Gerrit van der Laan, and Thorsten Hesjedal. Real-space observation of skyrmionium in a ferromagnet-magnetic topological insulator heterostructure. *Nano Letters*, 18(2):1057–1063, 2018.

[86] Murray Neff Wilson, AB Butenko, AN Bogdanov, and TL Monchesky. Chiral skyrmions in cubic helimagnet films: The role of uniaxial anisotropy. *Physical review B*, 89(9):094411, 2014.

[87] Andrey O Leonov. Skyrmion clusters and chains in bulk and thin-layered cubic helimagnets. *Physical review B*, 105(9):094404, 2022.

[88] Akira Tonomura, Xiuzhen Yu, Keiichi Yanagisawa, Tsuyoshi Matsuda, Yoshinori Onose, Naoya Kanazawa, Hyun Soon Park, and Yoshinori Tokura. Real-space observation of skyrmion lattice in helimagnet MnSi thin samples. *NanoLetters*, 12(3):1673–1677, 2012.

[89] EA Karhu, UK Rößler, AN Bogdanov, S Kahwaji, BJ Kirby, H Fritzsche, MD Robertson, CF Majkrzak, and TL Monchesky. Chiral modulations and reorientation effects in MnSi thin films. *Physical review B*, 85(9):094429, 2012.

[90] AB Butenko, AA Leonov, UK Rößler, and AN Bogdanov. Stabilization of skyrmion textures by uniaxial distortions in noncentrosymmetric cubic helimagnets. *Physical review B*, 82(5):052403, 2010.

[91] Wataru Koshibae and Naoto Nagaosa. Dynamics of skyrmion in disordered chiral magnet of thin film form. *Scientific Reports*, 9(1):5111, 2019.

[92] Xiuzhen Yu, Jan Masell, Fehmi S Yasin, Kosuke Karube, Naoya Kanazawa, Kiyomi Nakajima, Takuro Nagai, Koji Kimoto, Wataru Koshibae, Yasujiro Taguchi, et al. Real-space observation of topological defects in extended skyrmion-strings. *Nano Letters*, 20(10):7313–7320, 2020.

[93] AO Leonov, Yoshihiko Togawa, TL Monchesky, AN Bogdanov, J Kishine, Y Kousaka, M Miyagawa, T Koyama, J Akimitsu, Ts Koyama, et al. Chiral surface twists and skyrmion stability in nanolayers of cubic helimagnets. *Physical Review Letters*, 117(8):087202, 2016.

[94] SA Meynell, MN Wilson, H Fritzsche, AN Bogdanov, and TL Monchesky. Surface twist instabilities and skyrmion states in chiral ferromagnets. *Physical review B*, 90(1):014406, 2014.

[95] FN Rybakov, AB Borisov, and AN Bogdanov. Three-dimensional skyrmion states in thin films of cubic helimagnets. *Physical review B*, 87(9):094424, 2013.

[96] AO Leonov and M Mostovoy. Edge states and skyrmion dynamics in nanostripes of frustrated magnets. *Nature Communications*, 8(1):14394, 2017.

[97] Shilei Zhang, Gerrit van der Laan, Jan Müller, Lukas Heinen, Markus Garst, Andreas Bauer, Helmuth Berger, Christian Pfleiderer, and Thorsten Hesjedal. Reciprocal space tomography of 3D skyrmion lattice order in a chiral magnet. *Proceedings of the National Academy of Sciences*, 115(25):6386–6391, 2018.

[98] W Münzer, A Neubauer, T Adams, S Mühlbauer, C Franz, F Jonietz, R Georgii, P Böni, B Pedersen, M Schmidt, et al. Skyrmion lattice in the doped semiconductor $\mathrm{Fe}_{1-x}\mathrm{Co}_x\mathrm{Si}$. *Physical review B*, 81(4):041203, 2010.

[99] K Karube, JS White, N Reynolds, JL Gavilano, H Oike, A Kikkawa, F Kagawa, Y Tokunaga, Henrik M Rønnow, Y Tokura, et al. Robust metastable skyrmions and their triangular–square lattice structural transition in a high-temperature chiral magnet. *Nature Materials*, 15(12):1237–1242, 2016.

[100] Taro Nakajima, Hiroshi Oike, Akiko Kikkawa, Elliot P Gilbert, Norman Booth, Kazuhisa Kakurai, Yasujiro Taguchi, Yoshinori Tokura, Fumitaka Kagawa, and Taka-hisa Arima. Skyrmion lattice structural transition in MnSi. *Science advances*, 3(6):e1602562, 2017.

[101] MT Birch, R Takagi, S Seki, MN Wilson, F Kagawa, A Štefančič, G Balakrishnan, R Fan, P Steadman, CJ Ottley, et al. Increased lifetime of metastable skyrmions by controlled doping. *Physical review B*, 100(1):014425, 2019.

[102] L. J. Bannenberg, K. Kakurai, F. Qian, E. Lelièvre-Berna, C. D. Dewhurst, Y. Onose, Y. Endoh, Y. Tokura, and C. Pappas. Extended skyrmion lattice scattering and long-time memory in the chiral magnet $\mathrm{Fe}_{1-x}\mathrm{Co}_x\mathrm{Si}$. *Phys. Rev. B*, 94:104406, Sep 2016.

[103] James Rowland, Sumilan Banerjee, and Mohit Randeria. Skyrmions in chiral magnets with Rashba and Dresselhaus spin-orbit coupling. *Physical review B*, 93(2):020404, 2016.

[104] Sandip Bera and Sudhansu S Mandal. Theory of the skyrmion, meron, antiskyrmion, and antimeron in chiral magnets. *Physical Review Research*, 1(3):033109, 2019.

[105] ea Y Ishikawa, K Tajima, D Bloch, and M Roth. Helical spin structure in manganese silicide MnSi. *Solid State Communications*, 19(6):525–528, 1976.

[106] Fengjiao Qian, Lars J Bannenberg, Heribert Wilhelm, Grégory Chaboussant, Lisa M Debeer-Schmitt, Marcus P Schmidt, Aisha Aqeel, Thomas TM Palstra, Ekkes Brück, Anton JE Lefering, et al. New magnetic phase of the chiral skyrmion material Cu_2OSeO_3. *Science Advances*, 4(9):eaat7323, 2018.

[107] S-A Siegfried, AS Sukhanov, EV Altynbaev, Dirk Honecker, A Heinemann, AV Tsvyashchenko, and SV Grigoriev. Spin-wave dynamics in the helimagnet FeGe studied by small-angle neutron scattering. *Physical review B*, 95(13):134415, 2017.

[108] B Lebech, J Bernhard, and T Freltoft. Magnetic structures of cubic FeGe studied by small-angle neutron scattering. *Journal of Physics: Condensed Matter*, 1(35):6105, 1989.

[109] A. O. Leonov, C. Pappas, and I. Kézsmárki. Field and anisotropy driven transformations of spin spirals in cubic skyrmion hosts. *Phys. Rev. Research*, 2:043386, Dec 2020.

[110] A Chacon, L Heinen, M Halder, A Bauer, W Simeth, S Mühlbauer, H Berger, Markus Garst, Achim Rosch, and Christian Pfleiderer. Observation of two independent skyrmion phases in a chiral magnetic material. *Nature Physics*, 14(9):936–941, 2018.

[111] M Halder, A Chacon, A Bauer, W Simeth, S Mühlbauer, H Berger, L Heinen, M Garst, A Rosch, and C Pfleiderer. Thermodynamic evidence of a second skyrmion lattice phase and tilted conical phase in Cu_2OSeO_3. *Physical review B*, 98(14):144429, 2018.

[112] Dustin A Gilbert, Alexander J Grutter, Paul M Neves, Guo-Jiun Shu, Gergely Zimanyi, Brian B Maranville, Fang-Cheng Chou, Kathryn Krycka, Nicholas P Butch, Sunxiang Huang, et al. Precipitating ordered skyrmion lattices from helical spaghetti and granular powders. *Physical Review Materials*, 3(1):014408, 2019.

[113] ME Henderson, M Bleuel, J Beare, DG Cory, B Heacock, MG Huber, GM Luke, M Pula, D Sarenac, S Sharma, et al. Skyrmion alignment and pinning effects in the disordered multiphase skyrmion material $Co_8Zn_8Mn_4$. *Physical review B*, 106(9):094435, 2022.

[114] SL Zhang, A Bauer, DM Burn, P Milde, E Neuber, LM Eng, H Berger, C Pfleiderer, G Van Der Laan, and T Hesjedal. Multidomain skyrmion lattice state in Cu_2OSeO_3. *Nano letters*, 16(5):3285–3291, 2016.

[115] Markus Preißinger, K Karube, D Ehlers, B Szigeti, H-A Krug von Nidda, JS White, V Ukleev, HM Rønnow, Y Tokunaga, A Kikkawa, et al. Vital role of magnetocrystalline anisotropy in cubic chiral skyrmion hosts. *npj Quantum Materials*, 6(1):65, 2021.

[116] K Karube, JS White, V Ukleev, CD Dewhurst, R Cubitt, A Kikkawa, Y Tokunaga, HM Rønnow, Y Tokura, and Y Taguchi. Metastable skyrmion lattices governed by magnetic disorder and anisotropy in β-Mn-type chiral magnets. *Physical review B*, 102(6):064408, 2020.

[117] Daisuke Morikawa, Xiuzhen Yu, Kosuke Karube, Yusuke Tokunaga, Yasujiro Taguchi, Taka-hisa Arima, and Yoshinori Tokura. Deformation of topologically-protected supercooled skyrmions in a thin plate of chiral magnet $Co_8Zn_8Mn_4$. *Nano letters*, 17(3):1637–1641, 2017.

[118] Lars J Bannenberg, Heribert Wilhelm, Robert Cubitt, Ankit Labh, Marcus P Schmidt, Eddy Lelièvre-Berna, Catherine Pappas, Maxim Mostovoy, and Andrey O Leonov. Multiple low-temperature skyrmionic states in a bulk chiral magnet. *npj Quantum Materials*, 4(1):11, 2019.

[119] Chetan Dhital, Lisa DeBeer-Schmitt, David P Young, and John F DiTusa. Unpinning the skyrmion lattice in MnSi: Effect of substitutional disorder. *Physical review B*, 99(2):024428, 2019.

[120] Karin Everschor-Sitte and Matthias Sitte. Real-space Berry phases: Skyrmion soccer. *Journal of Applied Physics*, 115(17):172602, 2014.

[121] Junichi Iwasaki, Masahito Mochizuki, and Naoto Nagaosa. Current-induced skyrmion dynamics in constricted geometries. *Nature Nanotechnology*, 8(10):742–747, 2013.

[122] Fumitaka Kagawa, Hiroshi Oike, Wataru Koshibae, Akiko Kikkawa, Yoshihiro Okamura, Yasujiro Taguchi, Naoto Nagaosa, and Yoshinori Tokura. Current-induced viscoelastic topological unwinding of metastable skyrmion strings. *Nature Communications*, 8(1):1332, 2017.

[123] Seonghoon Woo, Kai Litzius, Benjamin Krüger, Mi-Young Im, Lucas Caretta, Kornel Richter, Maxwell Mann, Andrea Krone, Robert M Reeve, Markus Weigand, et al. Observation of room-temperature magnetic skyrmions and their current-driven dynamics in ultrathin metallic ferromagnets. *Nat. Mater.*, 15(5):501, 2016.

[124] Christoph Schütte and Achim Rosch. Dynamics and energetics of emergent magnetic monopoles in chiral magnets. *Physical review B*, 90(17):174432, 2014.

[125] A. O. Leonov and K. Inoue. Homogeneous and heterogeneous nucleation of skyrmions in thin layers of cubic helimagnets. *Phys. Rev. B*, 98:054404, 2018.

[126] S Seki, M Suzuki, M Ishibashi, R Takagi, ND Khanh, Y Shiota, K Shibata, W Koshibae, Y Tokura, and T Ono. Direct visualization of the three-dimensional shape of skyrmion strings in a noncentrosymmetric magnet. *Nature Materials*, 21(2):181–187, 2022.

[127] Jayaraman Rajeswari, Ping Huang, Giulia Fulvia Mancini, Yoshie Murooka, Tatiana Latychevskaia, Damien McGrouther, Marco Cantoni, Edoardo Baldini, Jonathan Stuart White, Arnaud Magrez, et al. Filming the formation and fluctuation of skyrmion domains by cryo-lorentz transmission electron microscopy. *Proceedings of the National Academy of Sciences*, 112(46):14212–14217, 2015.

[128] Wanjun Jiang, Xichao Zhang, Guoqiang Yu, Wei Zhang, Xiao Wang, M Benjamin Jungfleisch, John E Pearson, Xuemei Cheng, Olle Heinonen, Kang L Wang, et al. Direct observation of the skyrmion hall effect. *Nature Physics*, 13(2):162–169, 2017.

[129] C Reichhardt, D Ray, and CJ Olson Reichhardt. Collective transport properties of driven skyrmions with random disorder. *Physical Review Letters*, 114(21):217202, 2015.

[130] Charles Reichhardt, Cynthia Jane O Reichhardt, and MV Milošević. Statics and dynamics of skyrmions interacting with disorder and nanostructures. *Reviews of Modern Physics*, 94(3):035005, 2022.

[131] K Karube, Jonathan S White, D Morikawa, Marek Bartkowiak, A Kikkawa, Y Tokunaga, T-h Arima, Henrik M Rønnow, Y Tokura, and Y Taguchi. Skyrmion formation in a bulk chiral magnet at zero magnetic field and above room temperature. *Physical Review Materials*, 1(7):074405, 2017.

[132] Jonathan S White, Kosuke Karube, Victor Ukleev, PM Derlet, R Cubitt, CD Dewhurst, AR Wildes, XZ Yu, HM Rønnow, Yoshinori Tokura, et al. Small-angle neutron scattering study of mesoscale magnetic disordering and skyrmion phase suppression in the frustrated chiral magnet $Co_{6.75}Zn_{6.75}Mn_{6.5}$. *Journal of Applied Crystallography*, 55(5), 2022.

[133] Weiwei Xie, Srinivasa Thimmaiah, Jagat Lamsal, Jing Liu, Thomas W Heitmann, Dante Quirinale, Alan I Goldman, Vitalij Pecharsky, and Gordon J Miller. β-Mn-type $Co_{8+x}Zn_{12-x}$ as a defect cubic laves phase: Site preferences, magnetism, and electronic structure. *Inorganic Chemistry*, 52(16):9399–9408, 2013.

[134] T Hori, H Shiraish, and Y Ishii. Magnetic properties of β-MnCoZn alloys. *Journal of magnetism and magnetic materials*, 310(2):1820–1822, 2007.

[135] JR Stewart, BD Rainford, RS Eccleston, and R Cywinski. Non-fermi-liquid behavior of electron-spin fluctuations in an elemental paramagnet. *Physical Review Letters*, 89(18):186403, 2002.

[136] H Nakamura, K Yoshimoto, M Shiga, M Nishi, and K Kakurai. Strong antiferromagnetic spin fluctuations and the quantum spin-liquid state in geometrically frustrated-mn, and the transition to a spin-glass state caused by non-magnetic impurity. *Journal of Physics: Condensed Matter*, 9(22):4701, 1997.

[137] T Nakajima, K Karube, Y Ishikawa, M Yonemura, N Reynolds, JS White, HM Rønnow, A Kikkawa, Y Tokunaga, Y Taguchi, et al. Correlation between site occupancies and spin-glass transition in skyrmion host $Co_{10-\frac{x}{2}}Zn_{10-\frac{x}{2}}Mn_x$. *Physical review B*, 100(6):064407, 2019.

[138] Joshua D Bocarsly, Colin Heikes, Craig M Brown, Stephen D Wilson, and Ram Seshadri. Deciphering structural and magnetic disorder in the chiral skyrmion host materials $Co_xZn_yMn_z$ (x+ y+ z= 20). *Physical Review Materials*, 3(1):014402, 2019.

[139] V Ukleev, K Karube, PM Derlet, CN Wang, H Luetkens, D Morikawa, A Kikkawa, L Mangin-Thro, AR Wildes, Y Yamasaki, et al. Frustration-driven magnetic fluctuations as the origin of the low-temperature skyrmion phase in $Co_7Zn_7Mn_6$. *npj Quantum Materials*, 6(1):40, 2021.

[140] Kosuke Karube, Jonathan S White, Daisuke Morikawa, Charles D Dewhurst, Robert Cubitt, Akiko Kikkawa, Xiuzhen Yu, Yusuke Tokunaga, Taka-hisa Arima, Henrik M Rønnow, et al. Disordered skyrmion phase stabilized by magnetic frustration in a chiral magnet. *Science advances*, 4(9):eaar7043, 2018.

[141] Hiroshi Oike, Akiko Kikkawa, Naoya Kanazawa, Yasujiro Taguchi, Masashi Kawasaki, Yoshinori Tokura, and Fumitaka Kagawa. Interplay between topological and thermodynamic stability in a metastable magnetic skyrmion lattice. *Nature Physics*, 12(1):62–66, 2016.

[142] Y Okamura, F Kagawa, S Seki, and Y Tokura. Transition to and from the skyrmion lattice phase by electric fields in a magnetoelectric compound. *Nature Communications*, 7(1):12669, 2016.

[143] MN Wilson, MT Birch, A Štefančič, AC Twitchett-Harrison, G Balakrishnan, TJ Hicken, R Fan, P Steadman, and PD Hatton. Stability and metastability of skyrmions in thin lamellae of Cu_2OSeO_3. *Physical Review Research*, 2(1):013096, 2020.

[144] T Nagase, M Komatsu, YG So, T Ishida, H Yoshida, Y Kawaguchi, Y Tanaka, K Saitoh, N Ikarashi, M Kuwahara, et al. Smectic liquid-crystalline structure of skyrmions in chiral magnet $Co_{8.5}Zn_{7.5}Mn_4$ (110) thin film. *Physical Review Letters*, 123(13):137203, 2019.

[145] H Atac, M Constantinou, Z-E Meziani, M Paolone, and N Sparveris. Measurement of the neutron charge radius and the role of its constituents. *Nature Communications*, 12(1):1759, 2021.

[146] Grant J Mathews, T Kajino, and T Shima. Big bang nucleosynthesis with a new neutron lifetime. *Physical Review D*, 71(2):021302, 2005.

[147] Hartmut Abele. The neutron. its properties and basic interactions. *Progress in Particle and Nuclear Physics*, 60(1):1–81, 2008.

[148] RJ Campbell and VF Sears. Neutron optics: An introduction to the theory of neutron optical phenomena and their applications, 1989.

[149] Benjamin Heacock, Takuhiro Fujiie, Robert W Haun, Albert Henins, Katsuya Hirota, Takuya Hosobata, Michael G Huber, Masaaki Kitaguchi, Dmitry A Pushin, Hirohiko Shimizu, et al. Pendellösung interferometry probes the neutron charge radius, lattice dynamics, and fifth forces. *Science*, 373(6560):1239–1243, 2021.

[150] Hannes Bartosik, Jürgen Klepp, Claus Schmitzer, Stephan Sponar, Adán Cabello, Helmut Rauch, and Yuji Hasegawa. Experimental test of quantum contextuality in neutron interferometry. *Physical Review Letters*, 103(4):040403, 2009.

[151] Yuji Hasegawa, Rudolf Loidl, Gerald Badurek, Matthias Baron, and Helmut Rauch. Violation of a bell-like inequality in single-neutron interferometry. *Nature*, 425(6953):45–48, 2003.

[152] Samuel A Werner, Roberto Colella, Albert W Overhauser, and CF Eagen. Observation of the phase shift of a neutron due to precession in a magnetic field. *Physical Review Letters*, 35(16):1053, 1975.

[153] Helmut Rauch, Anton Zeilinger, Gerald Badurek, A Wilfing, W Bauspiess, and U Bonse. Verification of coherent spinor rotation of fermions. *Physics Letters A*, 54(6):425–427, 1975.

[154] Stephan Sponar, René IP Sedmik, Mario Pitschmann, Hartmut Abele, and Yuji Hasegawa. Tests of fundamental quantum mechanics and dark interactions with low-energy neutrons. *Nature Reviews Physics*, 3(5):309–327, 2021.

[155] William Michael Snow, Chris Haddock, and Ben Heacock. Searches for exotic interactions using neutrons. *Symmetry*, 14(1):10, 2021.

[156] Ke Li, Muhammad Arif, David G Cory, Robert Haun, Benjamin Heacock, Michael G Huber, Joachim Nsofini, Dimitry A Pushin, Parminder Saggu, Dusan Sarenac, et al. Neutron limit on the strongly-coupled chameleon field. *Physical Review D*, 93(6):062001, 2016.

[157] Arnab Banerjee, Jiaqiang Yan, Johannes Knolle, Craig A Bridges, Matthew B Stone, Mark D Lumsden, David G Mandrus, David A Tennant, Roderich Moessner, and Stephen E Nagler. Neutron scattering in the proximate quantum spin liquid α-RuCl$_3$. *Science*, 356(6342):1055–1059, 2017.

[158] AD Christianson, EA Goremychkin, R Osborn, S Rosenkranz, MD Lumsden, CD Malliakas, IS Todorov, H Claus, DY Chung, MG Kanatzidis, et al. Unconventional superconductivity in $Ba_{0.6}K_{0.4}Fe_2As_2$ from inelastic neutron scattering. *Nature*, 456(7224):930–932, 2008.

[159] O Nahman-Lévesque, D Sarenac, DG Cory, B Heacock, MG Huber, and DA Pushin. Generalizing the quantum information model for dynamic diffraction. *Physical review A*, 105(2):022403, 2022.

[160] Joachim Nsofini, Dusan Sarenac, Christopher J Wood, David G Cory, Muhammad Arif, Charles W Clark, Michael G Huber, and Dmitry A Pushin. Spin-orbit states of neutron wave packets. *Phys. Rev. A*, 94(1):013605, 2016.

[161] Joachim Nsofini, Dusan Sarenac, Kamyar Ghofrani, Michael G Huber, Muhammad Arif, David G Cory, and Dmitry A Pushin. Noise refocusing in a five-blade neutron interferometer. *Journal of applied physics*, 122(5), 2017.

[162] J Nsofini, D Sarenac, DG Cory, and DA Pushin. Coherence optimization in neutron interferometry through defocusing. *Physical review A*, 99(4):043614, 2019.

[163] Joachim Nsofini, Kamyar Ghofrani, Dusan Sarenac, David G Cory, and Dimitry A Pushin. Quantum-information approach to dynamical diffraction theory. *Physical review A*, 94(6):062311, 2016.

[164] Helmut Rauch and Samuel A Werner. *Neutron Interferometry: Lessons in Experimental Quantum Mechanics, Wave-Particle Duality, and Entanglement*, volume 12. Oxford University Press, USA, 2015.

[165] DA Pushin, M Arif, MG Huber, and DG Cory. Measurements of the vertical coherence length in neutron interferometry. *Physical Review Letters*, 100(25):250404, 2008.

[166] Benjamin Heacock, Robert Haun, Katsuya Hirota, Takuya Hosobata, Michael G Huber, Michelle E Jamer, Masaaki Kitaguchi, Dmitry A Pushin, Hirohiko Shimizu, Ivar Taminiau, et al. Measurement and alleviation of subsurface damage in a thick-crystal neutron interferometer. *Acta Crystallographica Section A: Foundations and Advances*, 75(6):833–841, 2019.

[167] Olivier Nahman-Lévesque, Dusan Sarenac, Owen Lailey, David G Cory, Michael G Huber, and Dmitry Pushin. Quantum information approach to the implementation of a neutron cavity. *New Journal of Physics*, 2023.

[168] AP Serebrov, VE Varlamov, AG Kharitonov, AK Fomin, Yu N Pokotilovski, P Geltenbort, IA Krasnoschekova, MS Lasakov, RR Taldaev, AV Vassiljev, et al. Neutron lifetime measurements using gravitationally trapped ultracold neutrons. *Physical review C*, 78(3):035505, 2008.

[169] Vladimir K Ignatovich. Ultracold neutrons—discovery and research. *Physics-Uspekhi*, 39(3):283, 1996.

[170] Dmitry A Pushin, Dusan Sarenac, Daniel S Hussey, Haixing Miao, Muhammad Arif, David G Cory, Michael G Huber, David L Jacobson, Jacob M LaManna, Joseph D Parker, et al. Far-field interference of a neutron white beam and the applications to noninvasive phase-contrast imaging. *Physical review A*, 95(4):043637, 2017.

[171] D Sarenac, DG Cory, J Nsofini, I Hincks, P Miguel, M Arif, Charles W Clark, MG Huber, and DA Pushin. Generation of a lattice of spin-orbit beams via coherent averaging. *Physical Review Letters*, 121(18):183602, 2018.

[172] Dimitry A Pushin, Michael G Huber, Muhammad Arif, Chandra B Shahi, Joachim Nsofini, Christopher J Wood, Dusan Sarenac, David G Cory, et al. Neutron interferometry at the National Institute of Standards and Technology. *Advances in High Energy Physics*, 2015, 2015.

[173] D Sarenac, G Gorbet, C Kapahi, Charles W Clark, DG Cory, H Ekinci, S Fangzhou, ME Henderson, MG Huber, D Hussey, et al. Cone beam neutron interferometry: from modeling to applications. *arXiv preprint arXiv:2309.01787*, 2023.

[174] Benjamin Heacock, Muhammad Arif, David G Cory, Thomas Gnaeupel-Herold, Robert Haun, Michael G Huber, Michelle Elizabeth Jamer, Joachim Nsofini, Dmitry A Pushin, Dusan Sarenac, et al. Increased interference fringe visibility from the post-fabrication heat treatment of a perfect crystal silicon neutron interferometer. *Review of Scientific Instruments*, 89(2), 2018.

[175] B Heacock, D Sarenac, DG Cory, MG Huber, DS Hussey, C Kapahi, H Miao, H Wen, and DA Pushin. Angular alignment and fidelity of neutron phase-gratings for improved interferometer fringe visibility. *AIP Advances*, 9(8), 2019.

[176] Daniel S Hussey, Houxun Miao, Guangcui Yuan, Dmitry Pushin, Dusan Sarenac, Michael G Huber, David L Jacobson, Jacob M LaManna, and Han Wen. Demonstration of a white beam far-field neutron interferometer for spatially resolved small angle neutron scattering. *arXiv preprint arXiv:1606.03054*, 2016.

[177] Parminder Saggu, Taisiya Mineeva, Muhammad Arif, David G Cory, Robert Haun, Ben Heacock, Michael G Huber, Ke Li, Joachim Nsofini, Dusan Sarenac, et al. Decoupling of a neutron interferometer from temperature gradients. *Review of Scientific Instruments*, 87(12), 2016.

[178] Ralf-Hendrik Menk, Archana Sharma, Andrea Vacchi, Hans Juergen Besch, and Albert Walenta. Nuclear instruments and methods in physics research, section a: Accelerators, spectrometers, detectors and associated. 2003.

[179] Les Allen, Marco W Beijersbergen, RJC Spreeuw, and JP Woerdman. Orbital angular momentum of light and the transformation of Laguerre-Gaussian laser modes. *Physical review A*, 45(11):8185, 1992.

[180] Jonathan Leach, Miles J Padgett, Stephen M Barnett, Sonja Franke-Arnold, and Johannes Courtial. Measuring the orbital angular momentum of a single photon. *Physical Review Letters*, 88(25):257901, 2002.

[181] Andrew R Cameron, Sandra WL Cheng, Sacha Schwarz, Connor Kapahi, Dusan Sarenac, Michael Grabowecky, David G Cory, Thomas Jennewein, Dmitry A Pushin, and Kevin J Resch. Remote state preparation of single-photon orbital-angular-momentum lattices. *Physical review A*, 104(5):L051701, 2021.

[182] Konstantin Y Bliokh, Ebrahim Karimi, Miles J Padgett, Miguel A Alonso, Mark R Dennis, Angela Dudley, Andrew Forbes, Sina Zahedpour, Scott W Hancock, Howard M Milchberg, et al. Roadmap on structured waves. *Journal of Optics*, 25(10):103001, 2023.

[183] Sacha Schwarz, Connor Kapahi, Ruoxuan Xu, Andrew R Cameron, Dusan Sarenac, Jean-Philippe W MacLean, Katanya B Kuntz, David G Cory, Thomas Jennewein, Kevin J Resch, et al. Talbot effect of orbital angular momentum lattices with single photons. *Physical review A*, 101(4):043815, 2020.

[184] Masaya Uchida and Akira Tonomura. Generation of electron beams carrying orbital angular momentum. *nature*, 464(7289):737–739, 2010.

[185] Benjamin J McMorran, Amit Agrawal, Ian M Anderson, Andrew A Herzing, Henri J Lezec, Jabez J McClelland, and John Unguris. Electron vortex beams with high quanta of orbital angular momentum. *Science*, 331(6014):192–195, 2011.

[186] Robert W Boyd. Neutrons with a twist. *Nature*, 525(7570):462–463, 2015.

[187] Yijie Shen, Xuejiao Wang, Zhenwei Xie, Changjun Min, Xing Fu, Qiang Liu, Mali Gong, and Xiaocong Yuan. Optical vortices 30 years on: OAM manipulation from topological charge to multiple singularities. *Light: Science & Applications*, 8(1):90, 2019.

[188] Ebrahim Karimi. Spiral phase plate, 2011. Last accessed 19 October 2023.

[189] Dusan Sarenac, Andrew E Silva, Connor Kapahi, DG Cory, B Thompson, and Dmitry A Pushin. Human psychophysical discrimination of spatially dependant Pancharatnam–Berry phases in optical spin-orbit states. *Scientific reports*, 12(1):3245, 2022.

[190] Connor Kapahi, Andrew E Silva, David G Cory, Mukhit Kulmaganbetov, Melanie Mungalsingh, Dmitry A Pushin, Taranjit Singh, Ben Thompson, and Dusan Sarenac. Measuring the visual angle of polarization-related entoptic phenomena using structured light. *arXiv preprint arXiv:2304.12941*, 2023.

[191] DA Pushin, C Kapahi, AE Silva, DG Cory, M Kulmaganbetov, M Mungalsingh, T Singh, B Thompson, and D Sarenac. Psychophysical discrimination of radially varying polarization entoptic phenomena. *arXiv preprint arXiv:2305.12637*, 2023.

[192] Dmitry A Pushin, David G Cory, Connor Kapahi, Mukhit Kulmaganbetov, Melanie Mungalsingh, Andrew E Silva, Taranjit Singh, Benjamin Thompson, and Dusan Sarenac. Structured light enhanced entoptic stimuli for vision science applications. *Frontiers in Neuroscience*, 17, 2023.

[193] Dusan Sarenac, Connor Kapahi, Andrew E Silva, David G Cory, Ivar Taminiau, Benjamin Thompson, and Dmitry A Pushin. Direct discrimination of structured light by humans. *Proceedings of the National Academy of Sciences*, 117(26):14682–14687, 2020.

[194] Charles W Clark, Roman Barankov, Michael G Huber, Muhammad Arif, David G Cory, and Dmitry A Pushin. Controlling neutron orbital angular momentum. *Nature*, 525(7570):504–506, 2015.

[195] D Sarenac, J Nsofini, I Hincks, M Arif, Charles W Clark, DG Cory, MG Huber, and DA Pushin. Methods for preparation and detection of neutron spin-orbit states. *New journal of physics*, 20(10):103012, 2018.

[196] Dusan Sarenac, Michael G Huber, Benjamin Heacock, Muhammad Arif, Charles W Clark, David G Cory, Chandra B Shahi, and Dmitry A Pushin. Holography with a neutron interferometer. *Optics express*, 24(20):22528–22535, 2016.

[197] Dusan Sarenac, Connor Kapahi, Wangchun Chen, Charles W Clark, David G Cory, Michael G Huber, Ivar Taminiau, Kirill Zhernenkov, and Dmitry A Pushin. Generation and detection of spin-orbit coupled neutron beams. *Proceedings of the National Academy of Sciences*, 116(41):20328–20332, 2019.

[198] Quan Le Thien, Sam McKay, Roger Pynn, and Gerardo Ortiz. Spin-textured neutron beams with orbital angular momentum. *Physical review B*, 107(13):134403, 2023.

[199] Tapan Chatterji. *Neutron scattering from magnetic materials.* Elsevier, 2005.

[200] Boualem Hammouda. Probing nanoscale structures-the SANS toolbox. *National Institute of Standards and Technology*, pages 1–717, 2008.

[201] Amparo Lopez-Rubio and Elliot Paul Gilbert. Neutron scattering: a natural tool for food science and technology research. *Trends in Food Science & Technology*, 20(11-12):576–586, 2009.

[202] Toyoko Imae, Toshiji Kanaya, Michihiro Furusaka, and Naoya Torikai. *Neutrons in soft matter*. John Wiley & Sons, 2011.

[203] Roger Pynn. Neutron scattering—a non-destructive microscope for seeing inside matter. *Neutron applications in earth, energy and environmental sciences*, pages 15–36, 2009.

[204] Roger Pynn. Neutron scattering: a primer. *Los Alamos Science*, 19:1–31, 1990.

[205] Theyencheri Narayanan, Hanna Wacklin, Oleg Konovalov, and Reidar Lund. Recent applications of synchrotron radiation and neutrons in the study of soft matter. *Crystallography Reviews*, 23(3):160–226, 2017.

[206] Volker S Urban, William T Heller, John Katsaras, and Wim Bras. Soft matter sample environments for time-resolved small angle neutron scattering experiments: A review. *Applied Sciences*, 11(12):5566, 2021.

[207] Igor A Zaliznyak and John M Tranquada. Neutron scattering and its application to strongly correlated systems. In *Strongly Correlated Systems: Experimental Techniques*, pages 205–235. Springer, 2014.

[208] Connor Kapahi, Dusan Sarenac, Markus Bleuel, David G Cory, Benjamin Heacock, Melissa E Henderson, Michael G Huber, Ivar Taminiau, and Dmitry Pushin. High-transmission neutron optical devices utilizing micro-machined structures. *Quantum Beam Science*, 7(1):10, 2023.

[209] Sam Mugiraneza and Alannah M Hallas. Tutorial: a beginner's guide to interpreting magnetic susceptibility data with the curie-weiss law. *Communications Physics*, 5(1):95, 2022.

[210] Reinhold Kleiner, Dieter Koelle, Frank Ludwig, and John Clarke. Superconducting quantum interference devices: State of the art and applications. *Proceedings of the IEEE*, 92(10):1534–1548, 2004.

[211] John Clarke. Principles and applications of squids. *Proceedings of the IEEE*, 77(8):1208–1223, 1989.

[212] Dietmar Drung. Dc squid systems overview. *Superconductor Science and Technology*, 4(9):377, 1991.

[213] John Clarke and Alex I Braginski. The squid handbook. vol. 2. applications of squids and squid systems. 2006.

[214] M Buchner, K Höfler, B Henne, V Ney, and A Ney. Tutorial: Basic principles, limits of detection, and pitfalls of highly sensitive squid magnetometry for nanomagnetism and spintronics. *Journal of Applied Physics*, 124(16):161101, 2018.

[215] James Walter Beare. *μSR and AC Susceptibility as a probe of Frustrated Pyrochlore Magnets and Type-1 Superconductivity*. PhD thesis, 2021.

[216] A Bauer and Ch Pfleiderer. Magnetic phase diagram of MnSi inferred from magnetization and ac susceptibility. *Physical review B*, 85(21):214418, 2012.

[217] Fedor Gömöry. Characterization of high-temperature superconductors by ac susceptibility measurements. *Superconductor Science and Technology*, 10(8):523, 1997.

[218] M Bałanda. Ac susceptibility studies of phase transitions and magnetic relaxation: Conventional, molecular and low-dimensional magnets. *Acta physica polonica A*, 124(6):964–976, 2013.

[219] AF Khoder. The superconducting transition and the behavior of the ac susceptibility. *Physics Letters A*, 94(8):378–380, 1983.

[220] Neil W Ashcroft and N David Mermin. *Solid state physics*. Cengage Learning, 2022.

[221] Tomce Runcevski and Craig M Brown. The Rietveld refinement method: Half of a century anniversary, 2021.

[222] RA Young. The reitveld method. international union of crystallography monographs on crystallography. *Oxford University Press*, 5:1–38, 1995.

[223] Juan Rodriguez-Carvajal. Fullprof: a program for Rietveld refinement and pattern matching analysis. In *satellite meeting on powder diffraction of the XV congress of the IUCr*, volume 127. Toulouse, France:[sn], 1990.

[224] Melissa E Henderson, James Beare, Sudarshan Sharma, Markus Bleuel, Pat Clancy, David G Cory, Michael G Huber, Casey A Marjerrison, Mathew Pula, Dusan Sarenac, et al. Characterization of a disordered above room temperature skyrmion material $Co_8Zn_8Mn_4$. *Materials*, 14(16):4689, 2021.

[225] Shoichi Nagata, PH Keesom, and HR Harrison. Low-dc-field susceptibility of cu mn spin glass. *Physical review B*, 19(3):1633, 1979.

[226] C J Glinka, J G Barker, B Hammouda, S Krueger, J J Moyer, and W J Orts. The 30 m small-angle neutron scattering instruments at the National Institute of Standards and Technology. *J. Appl. Cryst.*, 31:430–445, 1998.

[227] Steven R Kline. Reduction and analysis of SANS and USANS data using igor pro. *J. Appl. Cryst.*, 39(6):895–900, 2006.

[228] T Adams, S Mühlbauer, C Pfleiderer, F Jonietz, A Bauer, A Neubauer, R Georgii, P Böni, U Keiderling, K Everschor, et al. Long-range crystalline nature of the skyrmion lattice in MnSi. *Physical Review Letters*, 107(21):217206, 2011.

[229] B Heacock, D Sarenac, DG Cory, MG Huber, JPW MacLean, H Miao, H Wen, and DA Pushin. Neutron sub-micrometre tomography from scattering data. *IUCrJ*, 5(6011):893–900, 2020.

[230] C Back, V Cros, H Ebert, K Everschor-Sitte, A Fert, M Garst, Tianping Ma, S Mankovsky, T L Monchesky, M Mostovoy, N Nagaosa, S S P Parkin, C Pfleiderer, N Reyren, A Rosch, Y Taguchi, Y Tokura, K von Bergmann, and Jiadong Zang. The 2020 skyrmionics roadmap. *J. Phys. D Appl. Phys.*, 53:363001, 2020.

[231] M. T. Birch, S. H. Moody, M. N. Wilson, M. Crisanti, O. Bewley, A. Štefančič, G. Balakrishnan, R. Fan, P. Steadman, D. Alba Venero, R. Cubitt, and P. D. Hatton. Anisotropy-induced depinning in the Zn-substituted skyrmion host Cu_2OSeO_3. *Phys. Rev. B*, 102:104424, Sep 2020.

[232] V. Ukleev, Y. Yamasaki, D. Morikawa, K. Karube, K. Shibata, Y. Tokunaga, Y. Okamura, K. Amemiya, M. Valvidares, H. Nakao, Y. Taguchi, Y. Tokura, and T. Arima. Element-specific soft x-ray spectroscopy, scattering, and imaging studies of the skyrmion-hosting compound $Co_8Zn_8Mn_4$. *Phys. Rev. B*, 99:144408, Apr 2019.

[233] Specific commercial equipment, instruments, or materials are identified in this paper to foster understanding. such identification does not imply recommendation or endorsement by the National Institute of Standards and Technology, nor does it imply that the materials or equipment identified are necessarily the best available for the purpose.

[234] Gavin S. Abo, Yang-Ki Hong, Jihoon Park, Jaejin Lee, Woncheol Lee, and Byoung-Chul Choi. Definition of magnetic exchange length. *IEEE Transactions on Magnetics*, 49(8):4937–4939, 2013.

[235] P. Lu, H. Du, L. Wang, H. Li, W. Wang, Y. Shi, X. Wu, Y. Chai, and Y Sun. Skyrmion-glass-like phase in polycrystalline MnSi. *arXiv preprint arXiv:2201.12959*, 2022.

[236] Marijan Beg, Martin Lang, and Hans Fangohr. Ubermag: Towards more effective micromagnetic workflows. *IEEE Transactions on Magnetics*, 58(2):1–5, 2022.

[237] R. Takagi, D. Morikawa, K. Karube, N. Kanazawa, K. Shibata, G. Tatara, Y. Tokunaga, T. Arima, Y. Taguchi, Y. Tokura, and S. Seki. Spin-wave spectroscopy of the Dzyaloshinskii-Moriya interaction in room-temperature chiral magnets hosting skyrmions. *Phys. Rev. B*, 95:220406, 2017.

[238] V. Ukleev, K. A. Pschenichnyi, O. Utesov, K. Karube, S. Mühlbauer, R. Cubitt, Y. Tokura, Y. Taguchi, J. S. White, and S. V. Grigoriev. Spin wave stiffness and damping in a frustrated chiral helimagnet $Co_8Zn_8Mn_4$ as measured by small-angle neutron scattering. *Phys. Rev. Research*, 4:023239, Jun 2022.

[239] Thomas T. J. Mutter, Andrey O. Leonov, and Katsuya Inoue. Skyrmion instabilities and distorted spiral states in a frustrated chiral magnet. *Phys. Rev. B*, 100:060407, Aug 2019.

[240] Y. Fujishiro, N. Kanazawa, T. Nakajima, X. Z. Yu, K. Ohishi, Y. Kawamura, K. Kakurai, T. Arima, H. Mitamura, A. Miyake, K. Akiba, M. Tokunaga, A. Matsuo, K. Kindo, T. Koretsune, R. Arita, and Y. Tokura. Topological transitions among skyrmion- and hedgehog-lattice states in cubic chiral magnets. *Nature Communications*, 10(1):1059, Mar 2019.

[241] Peter Milde, Erik Neuber, Andreas Bauer, Christian Pfleiderer, and Lukas M. Eng. Surface pinning and triggered unwinding of skyrmions in a cubic chiral magnet. *Phys. Rev. B*, 100:024408, 2019.

[242] Tae-Hoon Kim, Haijun Zhao, Ben Xu, Brandt A. Jensen, Alexander H. King, Matthew J. Kramer, Cewen Nan, Liqin Ke, and Lin Zhou. Mechanisms of skyrmion and skyrmion crystal formation from the conical phase. *Nano Lett.*, 20:4731–4738, 2020.

[243] ME Henderson, B Heacock, M Bleuel, DG Cory, C Heikes, MG Huber, J Krzywon, O Nahman-Levesqué, GM Luke, M Pula, et al. Three-dimensional neutron far-field tomography of a bulk skyrmion lattice. *Nature Physics*, pages 1–7, 2023.

[244] G. van der Laan, S. L. Zhang, and T. Hesjedal. Depth profiling of 3d skyrmion lattices in a chiral magnet—a story with a twist. *AIP Advances*, 11(1):015108, 2021.

[245] Robert Streubel, Florian Kronast, Peter Fischer, Dula Parkinson, Oliver G. Schmidt, and Denys Makarov. Retrieving spin textures on curved magnetic thin films with full-field soft x-ray microscopies. *Nature Communications*, 6(1):7612, Jul 2015.

[246] C. Blanco-Roldán, C. Quirós, A. Sorrentino, A. Hierro-Rodríguez, L. M. Álvarez-Prado, R. Valcárcel, M. Duch, N. Torras, J. Esteve, J. I. Martín, M. Vélez, J. M. Alameda, E. Pereiro, and S. Ferrer. Nanoscale imaging of buried topological defects with quantitative x-ray magnetic microscopy. *Nature Communications*, 6(1):8196, Sep 2015.

[247] Claire Donnelly, Sebastian Gliga, Valerio Scagnoli, Mirko Holler, Jörg Raabe, Laura J Heyderman, and Manuel Guizar-Sicairos. Tomographic reconstruction of a three-dimensional magnetization vector field. *New Journal of Physics*, 20(8):083009, aug 2018.

[248] C Donnelly and V Scagnoli. Imaging three-dimensional magnetic systems with x-rays. *Journal of Physics: Condensed Matter*, 32(21):213001, feb 2020.

[249] M Strobl, W Treimer, and A Hilger. Small angle scattering signals for (neutron) computerized tomography. *Applied Physics Letters*, 85(3):488–490, 2004.

[250] Emil Y Sidky and Xiaochuan Pan. Image reconstruction in circular cone-beam computed tomography by constrained, total-variation minimization. *Physics in Medicine & Biology*, 53(17):4777, 2008.

[251] S. L. Zhang, G. van der Laan, W. W. Wang, A. A. Haghighirad, and T. Hesjedal. Direct observation of twisted surface skyrmions in bulk crystals. *Phys. Rev. Lett.*, 120:227202, May 2018.

[252] Melissa E Henderson, Benjamin Heacock, Markus Bleuel, David G Cory, Colin Heikes, Mike G Huber, Jeff Krzywon, Olivier Nahman-Levesque, Graeme M Luke, Mathew Pula, Dusan Sarenac, Kirill Zhernenkov, and Dmitry A Pushin. Supplemental videos for: Three-dimensional neutron far-field tomography of a bulk skyrmion lattice. *https://doi.org/10.5281/zenodo.7115410*, 2022.

[253] Arthur R. C. McCray, Yue Li, Rabindra Basnet, Krishna Pandey, Jin Hu, Daniel P. Phelan, Xuedan Ma, Amanda K. Petford-Long, and Charudatta Phatak. Thermal hysteresis and ordering behavior of magnetic skyrmion lattices. *Nano Letters*, 22(19):7804–7810, Oct 2022.

[254] Nitish Mathur, Fehmi S. Yasin, Matthew J. Stolt, Takuro Nagai, Koji Kimoto, Haifeng Du, Mingliang Tian, Yoshinori Tokura, Xiuzhen Yu, and Song Jin. In-plane magnetic field-driven creation and annihilation of magnetic skyrmion strings in nanostructures. *Advanced Functional Materials*, 31(13):2008521, 2021.

[255] Dusan Sarenac, Melissa E Henderson, Huseyin Ekinci, Charles W Clark, David G Cory, Lisa DeBeer-Schmitt, Michael G Huber, Connor Kapahi, and Dmitry A Pushin. Experimental realization of neutron helical waves. *Science Advances*, 8(46):eadd2002, 2022.

[256] Börge Göbel, Alexander Mook, Jürgen Henk, Ingrid Mertig, and Oleg A Tretiakov. Magnetic bimerons as skyrmion analogues in in-plane magnets. *Physical review B*, 99(6):060407, 2019.

[257] Jérémie Harris, Vincenzo Grillo, Erfan Mafakheri, Gian Carlo Gazzadi, Stefano Frabboni, Robert W Boyd, and Ebrahim Karimi. Structured quantum waves. *Nature Physics*, 11(8):629–634, 2015.

[258] Michael V Berry and Nandor L Balazs. Nonspreading wave packets. *American Journal of Physics*, 47(3):264–267, 1979.

[259] JJJM Durnin, JJ Miceli Jr, and Joseph H Eberly. Diffraction-free beams. *Physical Review Letters*, 58(15):1499, 1987.

[260] NR Heckenberg, R McDuff, CP Smith, H Rubinsztein-Dunlop, and MJ Wegener. Laser beams with phase singularities. *Optical and quantum electronics*, 24(9):S951–S962, 1992.

[261] George D Wignall, Kenneth C Littrell, William T Heller, Yuri B Melnichenko, Kathy M Bailey, Gary W Lynn, Dean A Myles, Volker S Urban, Michelle V Buchanan, Douglas L Selby, et al. The 40 m general purpose small-angle neutron scattering instrument at Oak Ridge National Laboratory. *Journal of Applied Crystallography*, 45(5):990–998, 2012.

[262] MV Berry. Optical vortices evolving from helicoidal integer and fractional phase steps. *Journal of Optics A: Pure and Applied Optics*, 6(2):259, 2004.

[263] Michael V Berry. Paraxial beams of spinning light. In *International conference on singular optics*, volume 3487, pages 6–12. International Society for Optics and Photonics, 1998.

[264] GA Siviloglou, J Broky, Aristide Dogariu, and DN Christodoulides. Observation of accelerating airy beams. *Physical Review Letters*, 99(21):213901, 2007.

[265] V Garces-Chavez, David McGloin, H Melville, Wilson Sibbett, and Kishan Dholakia. Simultaneous micromanipulation in multiple planes using a self-reconstructing light beam. *Nature*, 419(6903):145–147, 2002.

[266] Kyung Mee Song, Jae-Seung Jeong, Biao Pan, Xichao Zhang, Jing Xia, Sunkyung Cha, Tae-Eon Park, Kwangsu Kim, Simone Finizio, Jörg Raabe, et al. Skyrmion-based artificial synapses for neuromorphic computing. *Nature Electronics*, 3(3):148–155, 2020.

[267] Tomoyuki Yokouchi, Satoshi Sugimoto, Bivas Rana, Shinichiro Seki, Naoki Ogawa, Yuki Shiomi, Shinya Kasai, and Yoshichika Otani. Pattern recognition with neuromorphic computing using magnetic field–induced dynamics of skyrmions. *Science Advances*, 8(39):eabq5652, 2022.

[268] Paul Sutcliffe. Skyrmion knots in frustrated magnets. *Physical Review Letters*, 118(24):247203, 2017.

[269] Dusan Sarenac, Wangchun Chen, Charles W Clark, David G Cory, Connor Kapahi, Benjamin Heacock, Melissa Henderson, Michael Huber, Lisa DeBeer-Schmitt, Kirill Zhernenkov, et al. Novel methods of characterizing topological spin textures with neutron probes. In *Spintronics XVI*, volume 12656, page 1265602. SPIE, 2023.

[270] M Strobl, I Manke, N Kardjilov, A Hilger, M Dawson, and J Banhart. Advances in neutron radiography and tomography. *Journal of Physics D: Applied Physics*, 42(24):243001, 2009.

[271] M Strobl, C Grünzweig, A Hilger, I Manke, N Kardjilov, C David, and F Pfeiffer. Neutron dark-field tomography. *Physical Review Letters*, 101(12):123902, 2008.

[272] Markus Strobl, Ralph P Harti, Christian Grünzweig, Robin Woracek, and Jeroen Plomp. Small angle scattering in neutron imaging—a review. *Journal of Imaging*, 3(4):64, 2017.

[273] M Strobl, J Valsecchi, RP Harti, P Trtik, A Kaestner, C Gruenzweig, E Polatidis, and J Capek. Achromatic non-interferometric single grating neutron dark-field imaging. *Scientific Reports*, 9(1):19649, 2019.

[274] Jacopo Valsecchi, Ralph P Harti, Marc Raventós, Muriel D Siegwart, Manuel Morgano, Pierre Boillat, Markus Strobl, Patrick Hautle, Lothar Holitzner, Uwe Filges, et al. Visualization and quantification of inhomogeneous and anisotropic magnetic fields by polarized neutron grating interferometry. *Nature Communications*, 10(1):3788, 2019.

[275] Matteo Busi, Jiazhou Shen, Michael Bacak, Marie Christine Zdora, Jan Čapek, Jacopo Valsecchi, and Markus Strobl. Multi-directional neutron dark-field imaging with single absorption grating. *Scientific Reports*, 13(1):15274, 2023.

[276] WC Chen, TR Gentile, CB Fu, S Watson, GL Jones, JW McIver, and DR Rich. Polarized 3He cell development and application at NIST. In *Journal of Physics: Conference Series*, volume 294, page 012003. IOP Publishing, 2011.

[277] Wangchun Chen, Thomas R Gentile, R Erwin, Shannon Watson, Q Ye, Kathryn L Krycka, and Brian B Maranville. 3he spin filter based polarized neutron capability at the nist center for neutron research. In *Journal of Physics: Conference Series*, volume 528, page 012014. IOP Publishing, 2014.

[278] Thomas R Gentile, E Babcock, JA Borchers, WC Chen, D Hussey, GL Jones, WT Lee, CF Majkzrak, KV O'Donovan, WM Snow, et al. Polarized 3He spin filters in neutron scattering. *Physica B: Condensed Matter*, 356(1-4):96–102, 2005.

[279] Jiazhou Shen, Steven J Kuhn, Robert M Dalgliesh, VO de Haan, N Geerits, Abdul AM Irfan, Fankang Li, Shufan Lu, Stephen R Parnell, Jerome Plomp, et al. Unveiling contextual realities by microscopically entangling a neutron. *Nature Communications*, 11(1):1–6, 2020.

[280] Abu Ashik Md Irfan, Patrick Blackstone, Roger Pynn, and Gerardo Ortiz. Quantum entangled-probe scattering theory. *New Journal of Physics*, 23(8):083022, 2021.

[281] SJ Kuhn, S McKay, J Shen, N Geerits, RM Dalgliesh, E Dees, AAM Irfan, F Li, S Lu, V Vangelista, et al. Neutron-state entanglement with overlapping paths. *Physical Review Research*, 3(2):023227, 2021.

[282] S McKay, AAM Irfan, Q Le Thien, N Geerits, SR Parnell, RM Dalgliesh, NV Lavrik, II Kravchenko, G Ortiz, and R Pynn. Neutron spin echo is a" quantum tale of two paths". *arXiv preprint arXiv:2309.03987*, 2023.

[283] Jan Müller, Jayaraman Rajeswari, Ping Huang, Yoshie Murooka, Henrik M Rønnow, Fabrizio Carbone, and Achim Rosch. Magnetic skyrmions and skyrmion clusters in the helical phase of Cu_2OSeO_3. *Physical Review Letters*, 119(13):137201, 2017.

[284] Andrey O Leonov, Alex N Bogdanov, and Katsuya Inoue. Toggle-switch-like crossover between two types of isolated skyrmions within the conical phase of cubic helimagnets. *Physical review B*, 98(6):060411, 2018.

[285] Wanjun Jiang, Pramey Upadhyaya, Wei Zhang, Guoqiang Yu, M Benjamin Jungfleisch, Frank Y Fradin, John E Pearson, Yaroslav Tserkovnyak, Kang L Wang, Olle Heinonen, et al. Blowing magnetic skyrmion bubbles. *Science*, 349(6245):283–286, 2015.

[286] Jin-Sheng Wu and Ivan I Smalyukh. Hopfions, heliknotons, skyrmions, torons and both abelian and nonabelian vortices in chiral liquid crystals. *Liquid Crystals Reviews*, pages 1–35, 2022.

[287] Börge Göbel, Ingrid Mertig, and Oleg A Tretiakov. Beyond skyrmions: Review and perspectives of alternative magnetic quasiparticles. *Physics Reports*, 895:1–28, 2021.

[288] Maverick Chauwin, Xuan Hu, Felipe Garcia-Sanchez, Neilesh Betrabet, Alexandru Paler, Christoforos Moutafis, and Joseph S Friedman. Skyrmion logic system for large-scale reversible computation. *Physical Review Applied*, 12(6):064053, 2019.

[289] DA Pushin, MG Huber, M Arif, and DG Cory. Experimental realization of decoherence-free subspace in neutron interferometry. *Physical Review Letters*, 107(15):150401, 2011.

[290] Reinoud Lavrijsen, Ji-Hyun Lee, Amalio Fernández-Pacheco, Dorothée CMC Petit, Rhodri Mansell, and Russell P Cowburn. Magnetic ratchet for three-dimensional spintronic memory and logic. *Nature*, 493(7434):647–650, 2013.

[291] Jonas Nothhelfer, Sebastián A Díaz, Stephan Kessler, Tobias Meng, Matteo Rizzi, Kjetil MD Hals, and Karin Everschor-Sitte. Steering majorana braiding via skyrmion-vortex pairs: A scalable platform. *Physical Review B*, 105(22):224509, 2022.

[292] R Knapman, T Tausendpfund, SA Díaz, and K Everschor-Sitte. Spacetime magnetic hopfions: from internal excitations and braiding of skyrmions. *arXiv preprint arXiv:2305.07589*, 2023.

[293] Jin Tang, Yaodong Wu, Weiwei Wang, Lingyao Kong, Boyao Lv, Wensen Wei, Jiadong Zang, Mingliang Tian, and Haifeng Du. Magnetic skyrmion bundles and their current-driven dynamics. *Nature Nanotechnology*, 16(10):1086–1091, 2021.

[294] Xichao Zhang, Yan Zhou, and Motohiko Ezawa. High-topological-number magnetic skyrmions and topologically protected dissipative structure. *Physical review B*, 93(2):024415, 2016.

[295] Alexander G Kolesnikov, Maksim E Stebliy, Alexander S Samardak, and Alexey V Ognev. Skyrmionium–high velocity without the skyrmion hall effect. *Scientific reports*, 8(1):16966, 2018.

[296] Filipp N Rybakov and Nikolai S Kiselev. Chiral magnetic skyrmions with arbitrary topological charge. *Physical review B*, 99(6):064437, 2019.

[297] Y Okamura, F Kagawa, M Mochizuki, M Kubota, S Seki, S Ishiwata, M Kawasaki, Y Onose, and Y Tokura. Microwave magnetoelectric effect via skyrmion resonance modes in a helimagnetic multiferroic. *Nature Communications*, 4(1):2391, 2013.

[298] Y Onose, Y Okamura, S Seki, S Ishiwata, and Y Tokura. Observation of magnetic excitations of skyrmion crystal in a helimagnetic insulator Cu_2OSeO_3. *Physical Review Letters*, 109(3):037603, 2012.

[299] Tomoyuki Yokouchi, Shintaro Hoshino, Naoya Kanazawa, Akiko Kikkawa, Daisuke Morikawa, Kiyou Shibata, Taka-hisa Arima, Yasujiro Taguchi, Fumitaka Kagawa, Naoto Nagaosa, et al. Current-induced dynamics of skyrmion strings. *Science Advances*, 4(8):eaat1115, 2018.

[300] Varley F Sears. *Neutron optics: an introduction to the theory of neutron optical phenomena and their applications*, volume 3. Oxford University Press, USA, 1989.

[301] Eugene Balkind, Aldo Isidori, and Matthias Eschrig. Magnetic skyrmion lattice by the Fourier transform method. *Physical review B*, 99(13):134446, 2019.

[302] M. J. Donahue and D. G. Porter. OOMMF user's guide, version 1.0, 1999.

APPENDICES

Appendix A

Supplementary Discussion for Section 5

This section contains the details and discussions of the mathematical formalism of the seed generation, forward propagator, minimization, and defect density calculations used in the tomography algorithm and post-processing analysis of chapter 5.

A.1 Forward Propagator

The scattering pattern from passing through a single MSFR volume $S_{Q,\theta}$ for some projection θ is computed by propagating a neutron wave function through the sample via the time-evolution operator $\mathcal{U}$

$$S_{Q,\theta} = \left|\left\langle Q\middle|\mathcal{U}\middle|K_\theta\right\rangle\right|^2. \tag{A.1}$$

Which is estimated using a translation operator along the z-direction

$$\mathcal{J}_{\theta,dz} = e^{iK_z(\theta,Q)dz} \tag{A.2}$$

assuming elastic scattering

$$K_z(\theta, Q) = \sqrt{K^2 - (K\sin\theta - Q_x)^2 - Q_y^2}, \tag{A.3}$$

where K is the incoming neutron wave number, along with potential the potential V_z at layer z

$$\mathcal{U}_{\theta,z+dz} = \mathcal{J}_{\theta,dz}\left[1 - iV_z dz\, m_n/K_z\right], \tag{A.4}$$

where m_n is the neutron mass, and dz is the voxel height. The potential from the sample is computed from its resulting magnetic field by applying the characteristic $-\hat{Q}\times\hat{Q}\times$ operator in Fourier-space [300]

$$\boldsymbol{B}_s = -4\pi M_s \mathcal{F}^{-1}\left\{\hat{Q}\times\hat{Q}\times\mathcal{F}\left[\boldsymbol{m}\right]\right\} \tag{A.5}$$

where M_s is the saturated magnetization, with $4\pi M_s = 1900$ G estimated from DC susceptibility measurements taken at 310 K. The potential also includes the external field and operates on a neutron spinor via Pauli matrices

$$V = -\mu_n\boldsymbol{\sigma}\cdot(\boldsymbol{B}_s + \boldsymbol{H}_{\text{ext}}). \tag{A.6}$$

The unpolarized cross section

$$S_{Q,\theta} = \sum_{s,s'} \left|\langle Q, s'|\mathcal{U}|K_\theta, s\rangle\right|^2 \tag{A.7}$$

is then computed by summing over input s and selected s' spin states.

Assuming the longitudinal correlation length of the sample is smaller than the reconstruction height, the observed scattering pattern can be estimated by self-convolving the scattering pattern of a single MSFR N times

$$I_{Q\theta} = \sum_{Q'',Q'} Y_{QQ'}W^{\theta}_{Q'Q''}\left[(S*)^N I_0\right]_{Q''\theta}, \tag{A.8}$$

where N is the ratio of the sample dimension along the propagation direction and the corresponding size of the MSFR. For this sample $N = 860$. Because the forward propagator is a function of the projection of the momentum transfer in the $x-y$ plane Q_{xy}, the sparse matrix W shifts the scale of Q to be horizontal to the propagation axis. The sparse matrix Y smears out $Q = K\Omega_Q \simeq K_{\text{avg}}\Omega_Q(1-\delta\lambda/\lambda)$, where Ω_Q is the scattering angle, over the neutron's incoming wavelength distribution.

A.2 Seeding

The initial guess is formed by first estimating the three-dimensional vector amplitude of the MSFR in Fourier-space $|\widetilde{m}_0|^2$. This is accomplished by first performing a N^{th}-order deconvolution of the scattering signal with itself and the incoming beam profile, which solves for I_θ

$$I_{\text{meas}} = (I_\theta *)^N I_0 \tag{A.9}$$

with the I_θ slices of $|\widetilde{m}|$ for each measured projection unknown. This is accomplished with modified Richardson-Lucy algorithm, which is iterative

$$I_{\theta,i+1} = I_i \left[\left(\frac{I_{\text{meas}}}{\epsilon + (I_{\theta,i} *)^N I_0} \right) * (I_{\theta,i} *)^{N-1} I_0 \right] \tag{A.10}$$

where ϵ is a small regulator. When N is large, this can be unstable, and we found it is often helpful to enact this algorithm in stages, with I_{meas} deconvolved from I_0, then performing the deconvolution in n stages with $N' = N^{1/n}$. It can also be helpful to track the error of the deconvolution and stop iterating, or change the regulator size when the error stops decreasing with iteration number.

After deconvolution is complete, the Bragg peaks were fit to a Lorentzian profile with respect to Q_z. The projection with the incoming beam aligned with the dominant direction of the skyrmion tubes $I_{\theta=0}$ was then taken as the $|\widetilde{m}|$-slice at zero Q_z and expanded along the $Q_0 = D/J$ sphere, but attenuated according to the fitted Lorentzian with respect to Q_z. The result is a smooth function with a Lorentzian envelope along Q_z that preserves the transverse correlation structure of $I_{\theta=0}$. All the $Q > 0$ structure is then scaled and a DC term is introduced to $\widetilde{m}_0$ to generate the expected net sample magnetization $\langle m \rangle = \widetilde{m}(Q = 0)$.

After forming an estimate of $|\widetilde{m}_0|$, a guess for m is generated with an alternating projections algorithm. The vector field of the MSFR m is iteratively amended according to its constraints in Fourier and real-space. The Fourier-space constraint is given by the magnitude estimated from the deconvolved SANS data $|\widetilde{m}_0|$

$$\widetilde{\boldsymbol{m}}_{i+1} = \widetilde{\boldsymbol{m}}_i \frac{|\widetilde{m}_0|}{|\widetilde{m}_i|} \tag{A.11}$$

For the first few iterations, the transverse components of $\widetilde{m}$ are also redefined according to the sign of the DM term and expected curl around m_z

$$\widetilde{m}_{xy} = \pm i Q_{yx} \widetilde{m}_z. \tag{A.12}$$

The real space constraint is $\boldsymbol{m}^2 = 1$. However, it can also be beneficial to let m relax through a few iterations of a free energy minimizer before reapplying Fourier-space constraints. The net result is a guess m that adheres reasonably-well to the measured SANS projections, while also having a low free energy.

A.3 Minimization

The chosen cost function was

$$f = \chi^2 + \beta \mathcal{F}, \tag{A.13}$$

where the χ^2 is the sum of weighted residuals for all the projections

$$\chi^2 = \sum_{Q,\theta} (I_{Q,\theta} - M_{Q,\theta})^2 w_{Q,\theta} \tag{A.14}$$

and the free energy includes symmetric and antisymmetric exchange terms and a Zeeman term

$$\mathcal{F} = -\frac{1}{2} \boldsymbol{m} \cdot \nabla^2 \boldsymbol{m} + Q_0 \, \boldsymbol{m} \cdot (\nabla \times \boldsymbol{m}) - \boldsymbol{h} \cdot \boldsymbol{m} \tag{A.15}$$

where the reduced field $\boldsymbol{h} = \boldsymbol{H} Q_0^2 / J$, and helical shell radius $Q_0 = D/J$ is taken from the SANS patterns. The χ^2 depends on the difference between the measured SANS patterns $M_{Q,\theta}$ and estimated SANS intensity for each projection $I_{Q,\theta}$ computed from the MSFR via Eqn A.8. The residuals are weighted according to $w_{Q,\theta} = 1/\sigma^2_{Q,\theta}$, which is taken from the SANS reduction software [227], with the dominant uncertainty from Poisson counting statistics.

The Lagrange multiplier β acts like a Boltzmann factor. Since the $\chi^2 \sim \mathcal{O}(\sqrt{N_{Q,\theta}})$, where $N_{Q,\theta}$ is the total number of measured SANS pixels over all projections, and the two kinetic terms in $\mathcal{F} \sim \mathcal{O}(Q_0^2)$, a reasonable choice is $\beta = \sqrt{N_{Q,\theta}}/Q_0^2$. Adjusting the weight of the Zeeman term h will change the average magnetization $\langle m_z \rangle$. A reasonable value of h can be selected based on studying the behavior of the free energy term in isolation

[301]. However, we found that larger values of h were needed when the χ^2 was introduced to achieve the same average magnetization, likely because the χ^2 acts like a kinetic term which further reinforces the helical shell size Q_0. We therefore chose to study the behavior of the reconstructions over a range of h, as is shown in Table 1.

The gradient of the free energy term was computed via finite difference methods, similar to OOMMF [302]. The derivative of the χ^2 necessitates taking the derivative of the forward operator, which results in computing the overlap of the forward-propagating wavefunction ψ_θ with a backward-propagating residual wavefunction χ_θ for each projection

$$\frac{\delta}{\delta \boldsymbol{m}}\chi^2 = i\mu_n M_s m_n dz \ \sum_{\theta} \frac{1}{K_z}\ \mathcal{F}^{-1}\left\{\mathcal{F}\left\{\mathrm{Im}\left[\chi_\theta^\dagger \boldsymbol{\sigma}\psi_\theta\right]\right\}\cdot\left(\mathbb{I}-\hat{Q}\hat{Q}\right)\right\}, \tag{A.16}$$

where $\mathcal{F}\{\cdots\}$ and $\mathcal{F}^{-1}\{\cdots\}$ indicate forward and reverse Fourier transforms, respectively. The wavefunctions are computed by a combination of forward and backward propagation operators

$$\begin{aligned} \psi_\theta &= \left\langle x\middle|\mathcal{U}_z\middle|K_\theta\right\rangle \\ \chi_\theta &= \sum_{Q} \langle x|\mathcal{U}_{z,f}^{-1}|Q\rangle\, \widetilde{\psi}_{f,Q} G_Q \\ G_Q &= 2\sum_{Q',Q''} Y_{Q,Q'} W_{Q'',Q'} \left\{I_0 * [(I-M)w]\right\}_{Q'',\theta} \end{aligned} \tag{A.17}$$

where tildes indicate Fourier-space representations; subscript f denotes the final state; and $\mathcal{U}_{z,f}^{-1}$ is the backward in time propagator, starting from the final MSFR layer.

A.4 Defect Densities

The emergent magnetic field is computed from the MSFR and its derivatives

$$b_i = \frac{1}{2}\epsilon_{ijk}\boldsymbol{m}\cdot\left(\partial_j \boldsymbol{m}\times\partial_k \boldsymbol{m}\right), \tag{A.18}$$

where ϵ_{ijk} is the fully antismmetric tensor; $\partial_i \equiv \partial/\partial x_i$; and repeated indices are summed over the three space coordinates. Summing z-component of this field over an area is identified as the skyrmion winding number in the enclosed area, and the emergent magnetic charge density is defined as the source term for the emergent magnetic field

$$4\pi\rho_{\mathrm{em}} = \nabla \cdot \boldsymbol{b}. \tag{A.19}$$

A peak-finding algorithm was used to identify local maxima of ρ_{em}^2 that survive a threshold cut after a Gaussian blurring. The total emergent charge of the defect was then estimated to be the sum of ρ_{em} over the neighboring ±2 voxels in all directions. Further classification of branching (two skyrmion events) versus segmentation (single skyrmion events) was accomplished by summing $\partial_z m_z$ over the same neighborhood. The same or differing signs of the two summations indicate segmentation and branching defects, respectively.